UNIVERSITY OF LATVIA

FACULTY OF SCIENCE AND TECHNOLOGY

KEVON KADIWALA

Exploring Novel Synthesis Methods For Transition Metal Dichalcogenides and Investigating Their Properties

Submitted for the Doctoral degree in Physics

Subfield of Materials Physics

Scientific Advisor:

Dr. phys. Boris Polyakov

RIGA, 2025

The doctoral thesis work was carried out in Institute of Solid State Physics, University of Latvia from 2020 to 2024.

The thesis contains an introduction followed by 5 chapters and a reference list ending with acknowledgments.

Form of the thesis: dissertation in materials physics

Supervisor: *Dr. phys.* **Boris Polyakov**, senior researcher

Reviewers:

1. *Dr.* **Jana Andzane** (University of Latvia)
2. *Dr.* **Vjačeslavs Gerbreders** (Daugavpils University)
3. *Dr.* **Zia Ullah Khan** (Linchoping University, Sweden)

The thesis will be defended at the public session of the Promotional Council of Physics and Astronomy of University of Latvia on March 28th of 2025 in the conference hall of the Institute of Solid State Physics of University of Latvia.

The thesis is available at the Library of the University of Latvia, Raiņa bulv. 19.

Chairman of the Doctoral Committee *Dr. habil. phys.* **Uldis Rogulis**

Secretary of the Doctoral Committee **Sintija Siliņa**

Abstract

The field of Transition Metal Dichalcogenides (TMDs) has gathered significant attention due to its promising applications in electronics, optoelectronics, catalysis, and more. However, the current challenge lies in achieving scalable growth that meets commercial demands. This bottleneck has impeded the widespread commercialization of TMD-based products and necessitates a concerted effort to develop synthesis techniques that are both efficient and reproducible. This work seeks to address this critical issue by exploring a range of unique synthesis approaches designed to overcome these limitations.

The primary objective here, is to establish innovative methodologies for synthesizing TMD thin films on large-area substrates, ensuring consistency in geometry, quality, and reproducibility. Pulsed Laser Deposition (PLD) is one such method, offering precise control over film thickness and composition. Its versatility makes it suitable for scalable growth and the creation of heterostructures, enhancing device performance. Additionally, the combination of magnetron sputtering and chemical vapor transport (CVT) offers another promising approach. Magnetron sputtering allows precise deposition of precursor materials, while CVT enables controlled selenization or sulfurization for high-quality films. Ampoule-assisted conversion adds flexibility by providing a vacuum-sealed environment, reducing defects and improving crystallinity.

Beyond synthesis, this work delves into the detailed characterization of the synthesized TMD materials to evaluate their properties. Techniques like X-ray diffraction, Raman spectroscopy, and electron microscopy are employed to examine the films' chemical and structural properties, while electrical and optical analyses assess their quality for potential applications. By understanding the mechanisms of TMD synthesis and leveraging their unique properties, this research aims to facilitate broader adoption of TMD-based technologies. The findings could lead to breakthroughs in flexible electronics, high-performance transistors, and advanced photodetectors, ultimately driving innovation and enabling new commercial applications which have a lasting impact on technology and society.

Keywords: Transition Metal Dichalcogenides, Thin Films, Pulsed Laser Deposition, Magnetron Sputtering, Chemical Vapor Transport

Table of Contents

Abstract 2
List of abbreviations 5
List of figures 6
1. Introduction **9**
1.1 Current state of this field 10
1.2 Motivation of Research 12
1.2.1 Current Challenges 12
1.3 Objectives of this work 14
1.4 Scientific novelty 15
1.5 Outline of this work 16
2. General topics **18**
2.1 Fundamentals of Transition Metal Dichalcogenides 18
2.2 Common synthesis techniques overview 21
2.3 Material synthesis and investigation details 25
2.4 Unique Concepts explored in this work 27
3. Producing Heterostructures with TMDs **30**
3.1 MoS_2 and WS_2 grown on GaN nanowires 30
3.2 Growth of $TaSe_2$ on ZnS nanowire with Al_2O_3 as intermediary layer 33
3.3 Key results and Implications 37
3.3.1 GaN-MoS_2 and GaN-WS_2 Core–Shell NWs 37
3.3.2 Core/Shell NWs with $TaSe_2$ Shell by Selenizing Ta Film 37
3.3.3 Unique and novel aspects 38
4. Growth of TMDs thin films **39**
4.1 WSe_2 thin films and crystals 39
4.2 $ReSe_2$ thin films 45
4.3 $TiSe_2$ and VSe_2 thin films 50
4.4 Key results of the studies 53
4.4.1 WSe_2 Thin Films from WO_3 and W Metal Precursors 53
4.4.2 $ReSe_2$ Thin Films from Re Metal and ReO_x Precursors 54
4.4.3 Synthesis of $TiSe_2$ and VSe_2 thin films 54
4.4.4 Unique and novel aspects 55
5. Summary: Objectives in retrospect **56**

6. Main theses **57**
Author's publication list **58**
Participation in schools and conferences **60**
References **62**
Acknowledgements 78

List of abbreviations

AFM: Atomic Force Microscopy

ALD: Atomic Layer Deposition

CDW: Charge Density Wave

CVD: Chemical Vapour Deposition

CVT: Chemical Vapour Transport

DC: Direct Current

DFT: Density Functional Theory

DIW: Deionized Water

EDX: Energy Dispersive X-ray Spectroscopy

HER: Hydrogen Evolution Reaction

h-BN: Hexagonal Boron Nitride

ICDD: International Centre for Diffraction Data

MOCVD: Metal Organic Chemical Vapour Deposition

μm: Micrometre

nm: Nanometre

NWs: Nanowires

PDF: Powder Diffraction File

PLD: Pulsed Laser Deposition

Q-switching: Quality-switching (in lasers)

SEM: Scanning Electron Microscopy

TEM: Transmission Electron Microscopy

TMD: Transition Metal Dichalcogenide

XPS: X-ray Photoelectron Spectroscopy

XRD: X-ray Diffraction

1D: One-Dimensional

2D: Two-Dimensional

List of figures

Figure 1.1: Illustration of the current main-stream synthesis techniques for transition metal dichalcogenides divided in two main types **11**
Figure 1.2: Illustration of the current main-stream synthesis techniques for transition metal dichalcogenides divided in two main types **10**
Figure 1.3: Graphical presentation of current few but important challenges in the field of Transition Metal Dichalcogenides which require attention and focused research **13**
Figure 1.4: Directions of the desired results of this study to be obtained as the outcomes of this work illustration **15**
Figure 2.1: Graphical crystal structures of (a) hexagonal structure with a space group of $P6_3/mmc$ (b) triclinic crystal system with a space group of P-1 and (c) hexagonal crystal … **18**
Figure 2.2: Flow chart of the three different methodologies consisting of at times more than one technique for the synthesis of TMDs films (left to right) in this work **21**
Figure 2.3: Simplified graphical illustration of the Pulsed Laser Deposition technique **22**
Figure 2.4: Graphical illustration for working principal of Magnetron Sputtering method **23**
Figure 2.5: Schematics of the general working principal of Chemical vapour Deposition technique **24**
Figure 2.6: Graphical illustration of a quartz ampoule prepared during this study and its inside components before the heating process **25**
Figure 3.1: A schematic of both demonstrated GaN-MeX_2 core–shell NW preparation methods on Si/SiO_2 substrates: (1) two-step method, which includes sulfurization of pre-deposited metal oxide coating; and (2) direct deposition of MoS_2 or WS_2 with pulsed laser deposition **30**
Figure 3.3: (a) X-ray diffraction and (b) micro-Raman spectrum of GaN-MoS_2 NW arrays on a Si/SiO_2 substrate; (c) X-ray diffraction and (d) micro-Raman spectrum of GaN-WS_2 NW arrays on a Si/SiO_2 substrate. **31**
Figure 3.2: Transmission electron microscope images at different magnifications of individual (a-b) GaN-MoS_2 NW prepared via MoO_3 coating sulfurization, (c-d) GaN-MoS_2 NW … **31**
Figure 3.4: High-resolution XPS core-level spectra and peak fits of GaN-MoS_2 core–shell NWs for (a) Mo 3d, (b) S 2p, (c) Ga 3d and (d) N 1 s. High-resolution XPS core-level spectra … **32**
Figure 3.5: Schematic representation of the GaN-WS_2 and GaN-MoS_2 band edges positions with respect to the standard hydrogen electrode (SHE). Blue and red horizontal dashed lines correspond to the redox potentials for $H+/H_2$ and O_2/H_2O dissociation, respectively. **33**
Figure 3.6: A scheme for the four-step method for the fabrication of ZnS/ Al_2O_3/ $TaSe_2$ core/shell NWs. Growth of ZnS NWs via VLS mechanism using Au NPs catalysts (a). Al_2O_3 layer deposition by ALD around ZnS NWs (b). Ta thin film deposition on ZnS/Al_2O_3 NWs (c) **34**
Figure 3.8: High-resolution XPS spectra of the selenized ZnS/Al_2O_3/Ta NWs elements for (a) Ta and (b) Se. Ta 4f peak scan fitting revealed two chemical states (Ta 4+ and 5+) present in the sample. **35**
Figure 3.7: Rietveld refinement (solid line) of the X-ray diffraction pattern (open circles) for selenized ZnS/Al_2O_3/Ta NWs on an oxidized Si/SiO_2 substrate. The corresponding Bragg … **35**
Figure 3.9: TEM images of $ZnS/Al_2O_3/TaSe_2$ NWs at different magnifications. A single $ZnS/Al_2O_3/TaSe_2$ NW with a Au NP at the end on a Lacey carbon-coated TEM grid (a). $ZnS/Al_2O_3/TaSe_2$ NW … **36**
Figure 3.10: SEM images of selenized ZnS/ Al_2O_3/Ta NWs grown on Si/SiO_2 substrate at different magnifications taken at 12 keV (a,b) and 5 keV (c,d), respectively. **36**
Figure 4.1: Schematic of the process of on-chip device fabrication. First the SiO_2/Si substrate is cleaned using acetone and isopropanol (a), then the first mask is made using the … **39**

Figure 4.2: Optical images of the synthesized patterned WSe_2 films made by photolithography (a,b), and devices with various gap widths between the two electrodes were fabricated (c–e) using WSe_2 films..... **39**
Figure 4.3: Scanning electron microscope images at different magnifications of WSe_2 films made from a WO_3 precursor at 700°C (a,b) and 800°C (c,d) and from a W metal precursor at 700°C (e,f)..... **40**
Figure 4.4: Atomic force microscope (AFM) Z-drive images of WSe_2 films made from a WO_3 precursor (a) and from a W metal precursor (c) showing the difference between film surfaces and further complimented by SEM images of the same samples in the respective order of (b) and (d)..... **40**
Figure 4.5: X-ray diffraction patterns of WSe_2 films from both precursors (WO_3 and W) at different temperatures, 700°C and 800°C, show peaks confirming the phase of the synthesized WSe_2 film **41**
Figure 4.6: Raman spectra of WSe_2 thin films synthesized from both precursors (WO_3 and W) using CVT method showing the peaks respective to E^1_{2g} and A^1_g vibrational modes..... **41**
Figure 4.8: WSe_2 two-terminal photoconductor devices, prepared from W(a,b) and WO_3(c,d) metal as the precursor (I_{DS}-drain source current, V_{DS}-drain source bias voltage, V_{GS}- gate source bias voltage). **42**
Figure 4.7: WSe_2 two-terminal photoconductor devices prepared from WO_3 and W metal as the precursor materials, respectively, showing dark state I–V characteristics … **42**
Figure 4.9: WSe_2 crystal synthesis setup (c) used for the synthesis of crystals. Image a,b are important parameters shown by Zhou et al. which this setup was configured **43**
Figure 4.11: (left)Raman and (right) XRD of the synthesized WSe_2 crystals of different samples. For Raman, the signal was obtained by focusing laser on an atomically thin crystal whereas XRD data was obtained through large area scan over the whole substrate. **44**
Figure 4.10: Optical images of the synthesized WSe_2 crystals on different samples. **44**
Figure 4.12: (a-c) Optical images of the devices made and (d-f) photo measurements. 1V bias applied for all measurements..... **44**
Figure 4.13: FET measurements performed on 2D crystals to show its p-type of conductivity of crystals..... **45**
Figure 4.14: Graphical illustration of the methodology followed in this work starting with (a) substrate preparation by cutting them in ~100 mm^2 square size and cleaning … **45**
Figure 4.15: X-ray diffraction patterns for the synthesized $ReSe_2$ films from (a) Re metal precursor films and (b) ReO_x precursor films at 650°C, 750°C, 850°C and 1000°C on SiO_2/Si substrate for 15 mins..... **46**
Figure 4.16: SEM images of the synthesized $ReSe_2$ films from (a-d) Re metal precursor films and (e-h) ReO_x precursor films using 650°C to 1000°C temperatures on silicon as substrate..... **46**
Figure 4.17: AFM images of the synthesized $ReSe_2$ films on sapphire substrate from (a-d) Re metal precursor and (e-h) ReO_x precursor at 650°C and 750°C temperatures are shown here … **47**
Figure 4.18: XPS spectra of $ReSe_2$ films synthesized at 650°C from (a,b) Re precursor films and (c,d) ReO_x precursor films. (e) Raman spectra of the $ReSe_2$ films synthesized at 650°C measured **48**
Figure 4.19: (a) Transmittance, (b) absorption and (c) reflectance of the produced $ReSe_2$ films on sapphire substrate from both precursor materials in the range of 500-2500 nm wavelength. **48**
Figure 4.20: Tauc plot to deduce the direct optical bandgap of the $ReSe_2$ films synthesized from (a) ReO_x and (b) Re metal. (c) Change in Resistivity with temperature was measured..... **49**
Figure 4.21: Open aperture Z-scan curves of the $ReSe_2$ thin films (a) synthesized from Re at 650°C and 750°C measured with the power of 16.4 W and 20.1 W respectively, (b) from ReO_x at 650°C and 750°C with the power of 21.2 W and 24.2 W with 900nm wavelength laser source. **49**
Figure 4.22: Graphical illustration of the methodology used here to synthesize $TiSe_2$ and VSe_2 thin films starting from (a) substrate cleaning in acetone and DIW using ultrasound … **51**
Figure 4.23: Optical images of $TiSe_2$ (a,b) and VSe_2 (c,d) thin films converted at 700°C with different magnifications, used to confirm the presence of surface crystals..... **51**

Figure 4.24: SEM images of $TiSe_2$ thin films (a,d) converted at 650°C, (b,e) at 700°C and (c,f) at 750°C. (g) XRD spectra of $TiSe_2$ thin films synthesized using different temperatures **52**
Figure 4.25: SEM images of VSe_2 thin films (a,d) converted at 650°C, (b,e) at 700°C and (c,f) at 750°C. (g) XRD spectra of synthesized VSe_2 thin films using different temperatures. **52**
Figure 4.26: EDX elemental mapping of (a-c) $TiSe_2$ and (d-f) VSe_2 films synthesized at 650°C, shows presence and distribution of their respective elements across the film **53**

1. Introduction

Transition metal dichalcogenides (TMDs) have emerged as a prominent class of materials within the field of materials science, captivating researchers due to their unique properties and diverse potential applications[1–5]. Characterized by a layered structure wherein transition metal atoms are covalently bonded between chalcogen atom layers arranged in a hexagonal lattice, TMDs exhibit remarkable tunability[2,6–9]. This tunability stems from the ability to manipulate factors such as layer thickness, chemical composition, and the application of external stimuli like strain and doping. By meticulously controlling these parameters, researchers can engineer the electronic, optical, mechanical, and catalytic properties of TMD materials with high precision [10–14]. This exceptional degree of control positions TMDs as highly attractive candidates for a wide range of applications across various scientific disciplines [4,9,14–17].

In the domain of electronics, TMDs have attracted significant attention as promising materials for next-generation electronic devices. Their inherent advantages include high carrier mobility, excellent electrostatic control, and compatibility with flexible and transparent substrates – all crucial characteristics for the development of advanced electronics [18,19]. Field-effect transistors (FETs) fabricated using TMDs have demonstrated impressive performance metrics, signifying their potential utility in logic circuits, memory devices, and beyond [5,18,20–26]. Furthermore, the creation of TMD heterostructures – achieved by stacking different TMD layers or combining TMDs with complementary materials like graphene or boron nitride – offers the exciting possibility of realizing entirely novel electronic functionalities and device architectures [1,2,16].

TMDs also hold immense promise in the realm of optoelectronics due to their intriguing optical properties. These properties encompass strong light-matter interactions, tuneable bandgaps, and efficient light emission. By harnessing these attributes, TMDs are being explored for applications in photodetectors, light-emitting diodes (LEDs), and photovoltaic devices [27–29]. By leveraging the unique quantum confinement effects and excitonic phenomena observed in TMD monolayers, researchers are actively developing ultra-compact photonic and optoelectronic devices boasting unprecedented performance characteristics[30–34]. These advancements pave the way for the realization of integrated photonic circuits and quantum technologies. The potential of TMDs extends beyond electronics and optoelectronics. They are also demonstrating exceptional promise as efficient and Earth-abundant catalysts for various chemical reactions, including hydrogen evolution, oxygen reduction, and nitrogen fixation[6,24,35]. The high surface areas, abundant active sites, and tuneable electronic structures exhibited by TMD materials contribute to their remarkable catalytic activity[14,36,37]. This has opened doors for their utilization in sustainable energy conversion technologies and environmental remediation efforts.

Furthermore, TMDs are making significant inroads in the field of energy storage and conversion, with potential applications in lithium-ion batteries, supercapacitors, and electrochemical water splitting [16,38–40]. Their high surface area, mechanical flexibility, and chemical stability make TMD-based electrodes and catalysts attractive candidates for enhancing the performance and longevity of energy storage and conversion devices. Finally, TMDs are proving to be exceptional sensing materials, exhibiting exceptional sensitivity to external stimuli such as gases, biomolecules, and mechanical strain[5,19,27,41]. By functionalizing TMD surfaces with specific ligands or exploiting their intrinsic electronic and optical responses, researchers are developing ultrasensitive and selective sensors capable of detecting a wide range of analytes. These sensors have the potential to revolutionize various fields, including environmental monitoring, healthcare diagnostics, and industrial process control [36,42–44]. The exploration of TMDs is an ongoing endeavour, and as researchers continue

to unveil their secrets, we can anticipate even more groundbreaking discoveries that will significantly reshape various technological landscapes. This ongoing pursuit underscores the immense potential of TMDs and their transformative role in the future of materials science.

1.1 Current state of this field

Material Properties and Applications

Electrically, TMDs can exhibit both n-type and p-type conductivity, depending on their composition and doping. **MoS_2** and **WS_2** are typically n-type semiconductors, which makes them suitable for applications in field-effect transistors (FETs) and other electronic devices [24,45–47]. On the other hand, **WSe_2** and **$ReSe_2$** can exhibit p-type conductivity, which is beneficial for creating p-n junctions and complementary logic circuits [48–52].

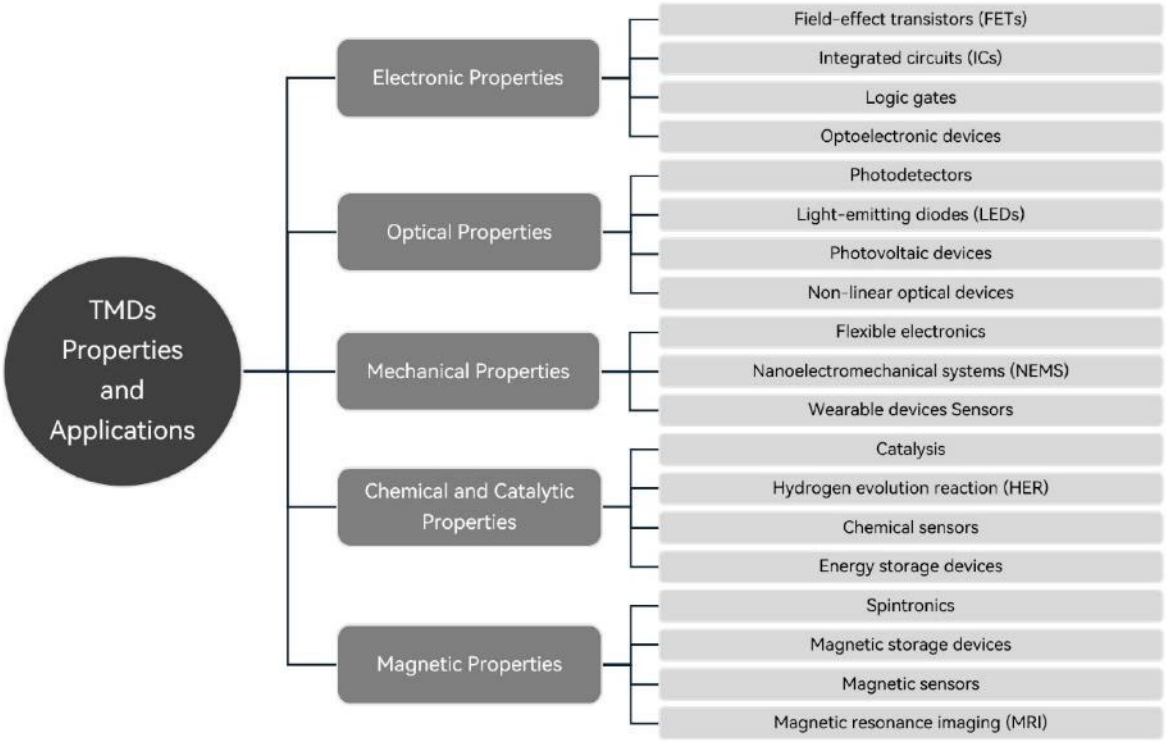

Figure 1.1: Illustration of the current main-stream synthesis techniques for transition metal dichalcogenides divided in two main types.

WSe_2 offers unique advantages, such as its tuneable bandgap and strong spin-orbit coupling. These properties make it a promising material for spintronic devices and optoelectronic applications. Its high carrier mobility and mechanical strength also contribute to its potential for various electronic devices [53–56]. **$ReSe_2$** is another intriguing TMD with anisotropic properties, making it a promising candidate for catalysis and sensing applications. Its layered structure and unique electronic properties offer opportunities for exploring novel device concepts [57–59]. **$TiSe_2$** and **VSe_2** are relatively less explored TMDs, but they have shown promise for various applications. TiSe2, for instance, exhibits metallic behaviour and has been investigated for its potential in energy storage and electronic devices. It has also attracted attention due to its charge density wave phase transitions and potential for superconducting behaviour [60–63].

The ongoing research and development in the field of TMDs continue to uncover new properties and applications, solidifying their role as a key material in the advancement of modern technology and next generation of electronics.

Common Synthesis Methods

The synthesis techniques of 2D TMDs have evolved from mechanical exfoliation to more sophisticated CVD process, currently encompassing both bottom-up and top-down approaches in various studies *(fig. 1.2)*. Mechanical exfoliation, a top-down method and the earliest employed for isolating TMD monolayers, involves manually peeling layers from bulk crystals[64–70]. While effective for producing small quantities of pristine TMD flakes, this method is labour-intensive and limited in scalability, hindering its utility for large-scale production. In contrast, bottom-up synthesis methods such as chemical vapor deposition (CVD), metal-organic chemical vapor deposition (MOCVD), and molecular beam epitaxy (MBE) have gained prominence for their ability to produce high-quality TMD monolayers with precise thickness and composition[66,71,72].

Chemical vapor deposition involves the decomposition of precursor gases on a substrate surface to form TMD monolayers. By carefully controlling the deposition parameters such as temperature,

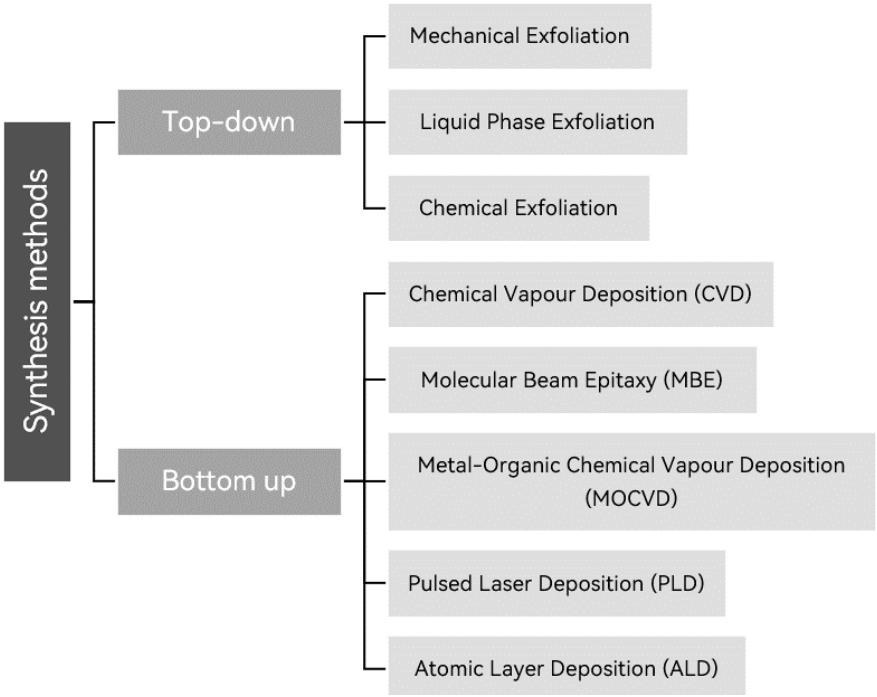

Figure 1.2: Illustration of the current main-stream synthesis techniques for transition metal dichalcogenides divided in two main types.

pressure, and gas flow rates, researchers can achieve uniform growth of TMD films over large areas. This scalability makes CVD particularly attractive for industrial-scale production of TMD-based devices. Metal-organic chemical vapor deposition (MOCVD), another bottom-up technique, introduces metal-organic precursors along with sulphur or selenium sources into a high-temperature reactor. This method allows controlled growth of TMD films with excellent uniformity and reproducibility. MOCVD has demonstrated the capability for wafer-scale growth of TMD monolayers, showcasing its potential for large-scale applications [73–75].

In addition to these methods, pulsed laser deposition (PLD) and physical vapor deposition (PVD) have been explored for the synthesis of TMDs. PLD, a versatile bottom-up technique, uses high-energy laser pulses to ablate a target material, depositing it onto a substrate [76–78]. This method allows for precise control over the film's composition and thickness, making it suitable for synthesizing complex TMD structures. PVD, which encompasses techniques such as sputtering and evaporation, involves the physical transfer of material from a source to a substrate in a vacuum environment. PVD methods are advantageous for their simplicity and ability to produce uniform TMD films over large areas [79,80].

1.2 Motivation of Research

While significant research has been conducted on TMD semiconductors like MoS_2, WS_2, WSe_2, $ReSe_2$, $TaSe_2$, $TiSe_2$ and VSe_2, much of the focus has been on laboratory-scale synthesis techniques such as exfoliation and molecular beam epitaxy (MBE) [20,27,64–72]. These methods, while effective for producing high-quality materials, often suffer from scalability issues and are not suitable for large-scale industrial production. As a result, there is a critical need to develop scalable synthesis techniques for these materials to realize their full potential in a wide range of technological applications. Exfoliation, a top-down approach, involves mechanically exfoliating bulk crystals into thin layers. While this method can produce high-quality, single-layer TMDs, it is inherently limited in terms of scalability and yield [3,81,82]. Molecular beam epitaxy, a bottom-up approach, offers precise control over the growth of TMD layers, but it is a complex and expensive technique that is not suitable for large-scale production [27,72,83].

To address these limitations, researchers are exploring alternative synthesis techniques, such as chemical vapor deposition (CVD) and metal-organic chemical vapor deposition (MOCVD), which offer greater scalability and control over the growth of TMDs [73,80,84]. However, these techniques still face challenges in terms of achieving high-quality, uniform, and large-area TMD films. Therefore, there is a pressing need to develop innovative synthesis techniques that can bridge the gap between laboratory-scale research and industrial-scale production of TMD materials. By addressing the scalability and cost challenges associated with current synthesis methods, researchers can pave the way for the widespread adoption of TMD-based technologies.

1.2.1 Current Challenges

Synthesis: One of the foremost challenges in the field of TMDs is the synthesis of high-quality, uniform materials. Traditional methods like chemical vapor deposition (CVD), mechanical exfoliation, and liquid-phase exfoliation have their limitations. For instance, mechanical exfoliation can produce high-quality monolayers but is not scalable for industrial applications. On the other hand, CVD can scale up the production but often results in non-uniform films with grain boundaries that impair the material's properties [81,85]. The control over the phase and composition during synthesis is another significant challenge. TMDs can exist in different phases (e.g., 1T, 2H), which exhibit drastically different electronic properties. Achieving a uniform phase is crucial for the consistency of device performance. Moreover, doping and alloying TMDs to tailor their properties require precise control over the synthesis process, which is difficult to achieve consistently [85].

Scalability and Cost: Scalability remains a major hurdle in the commercialization of TMDs. While methods like CVD show promise for large-scale production, the costs associated with these processes

are still prohibitive. Additionally, the equipment and conditions required for high-quality synthesis (such as high temperatures and vacuum environments) add to the complexity and cost [81]. Efforts are being made to develop cost-effective, scalable methods. For example, liquid-phase exfoliation offers a lower-cost alternative but often results in lower-quality materials with defects and impurities that can impact their performance. The challenge lies in balancing cost, quality, and scalability to make TMDs viable for industrial applications[81].

Integration with Existing Technologies: Integrating TMDs with existing semiconductor technologies presents both opportunities and challenges. TMDs offer the potential for novel device architectures, such as vertical transistors and flexible electronics, but their integration with silicon-based technologies requires overcoming several technical barriers. Issues such as contact resistance,

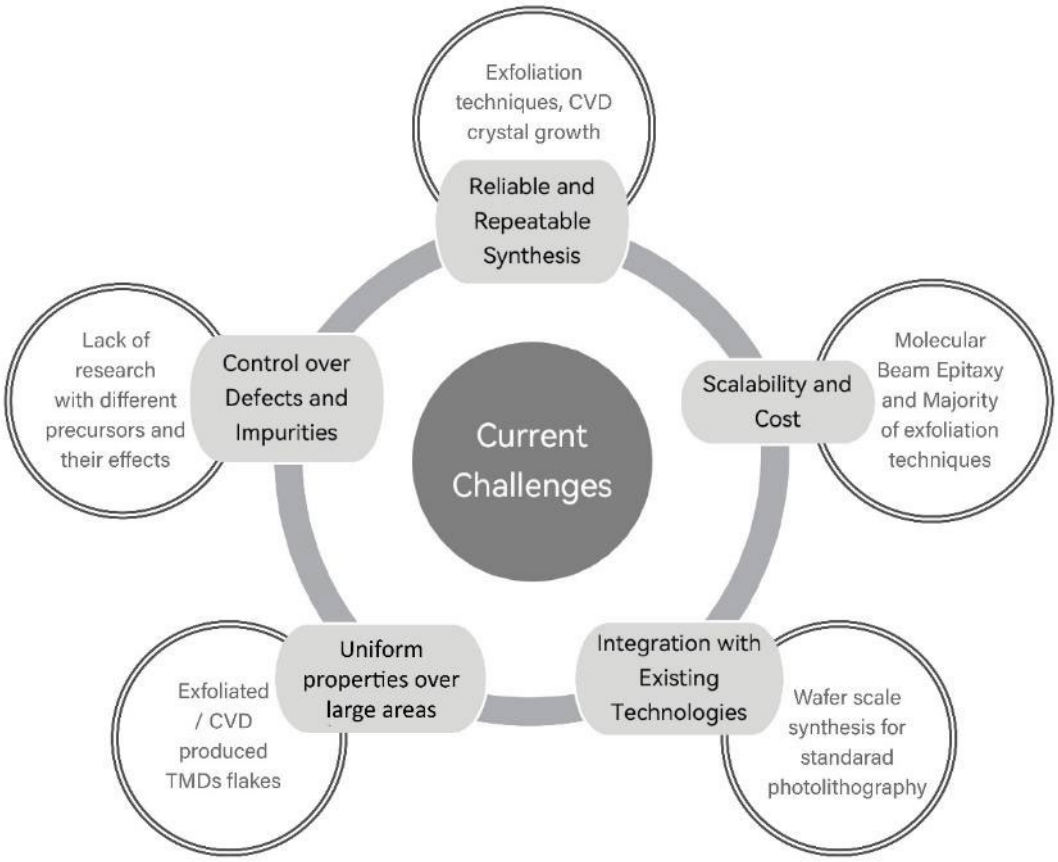

Figure 1.3: Graphical presentation of current few but important challenges in the field of Transition Metal Dichalcogenides which require attention and focused research

interface quality, and compatibility with current fabrication processes need to be addressed to achieve seamless integration. Efforts are being made to develop hybrid systems that combine TMDs with other materials like graphene or traditional semiconductors. These hybrid systems can exploit the unique properties of each component, but achieving high-quality interfaces and reliable performance remains challenging. Advanced fabrication techniques and interface engineering are critical to overcoming these hurdles.

Electronic and Optoelectronic Properties: While TMDs exhibit promising electronic and optoelectronic properties, tuning these properties for specific applications is complex. For instance, controlling the bandgap through layer thickness, strain, or chemical doping requires precise manipulation at the atomic level. Achieving uniform and predictable changes across large areas is

particularly challenging. Furthermore, the variability in electronic properties due to defects and impurities can significantly impact device performance. Identifying and controlling these defects are essential for the reproducibility and reliability of TMD-based devices. Advanced characterization techniques and theoretical modelling are vital to understanding and mitigating these issues.

Catalysis and Energy Applications: In catalysis, TMDs have shown potential for applications like hydrogen evolution reaction (HER), oxygen reduction reaction (ORR), and nitrogen fixation[6,24,67]. However, the activity and stability of TMD catalysts can be affected by their surface structure, defects, and phase purity. Enhancing the catalytic performance requires a deep understanding of the active sites and mechanisms at play, which is currently a significant research focus. For energy storage applications, such as in lithium-ion batteries and supercapacitors, the mechanical stability and electrical conductivity of TMDs are crucial. Developing TMDs with high specific surface areas, robust mechanical properties, and excellent conductivity while maintaining low production costs is a significant challenge. Research is ongoing to optimize these materials for better performance and durability.

This study is motivated by the need to address some key challenges hindering the practical application of TMDs in advanced technologies *(fig. 1.3)*. By exploring various existing synthesis technologies and their unique combinations, the study aims to improve the qualitative synthesis, scalability, repeatability, and stability of TMD films. Additionally, the study focuses on the integration of TMDs with existing technologies and the comprehensive understanding of their properties. Overcoming these challenges is critical for realizing the full potential of TMDs in a wide range of applications, including electronics, optoelectronics, catalysis, and energy storage. The findings of this study will contribute to the advancement of TMD research and take us a step further for their successful implementation in commercial applications.

1.3 Objectives of this work

The primary goal of this work was to synthesize and explore transition metal dichalcogenides through diverse methodologies and subsequently analyse the resulting materials. By doing so, the aim was set for assessing both the potential applications of the synthesized materials and the effectiveness of the methodologies employed for their synthesis *(fig. 1.4)*. Following objectives give detailed understanding of what was intended to achieve through this study:

1. Develop scalable synthesis methods for fabricating thin films of TMDs on various substrates, including one-dimensional nanowires and two-dimensional silicon or sapphire wafers, to enable large-scale applications of these materials.
2. Develop synthesis techniques for TMDs using their respective transition metals as precursors instead of their oxides, which often have high thermal stability. For instance, using Ta metal instead of Ta_2O_5 to produce $TaSe_2$ can be a more effective approach due to the challenges associated with the thermal stability of Ta_2O_5.
3. Synthesize a select few TMDs from their respective metal and metal oxide precursors under similar conditions to study the electrical properties and morphological differences, and identify potential applications based on these findings.
4. Use characterization techniques such as XRD, Raman, XPS to study the chemical and structural properties of the produced materials in addition to SEM, TEM, AFM for more deeper understanding, exploring their potential applications in various fields.

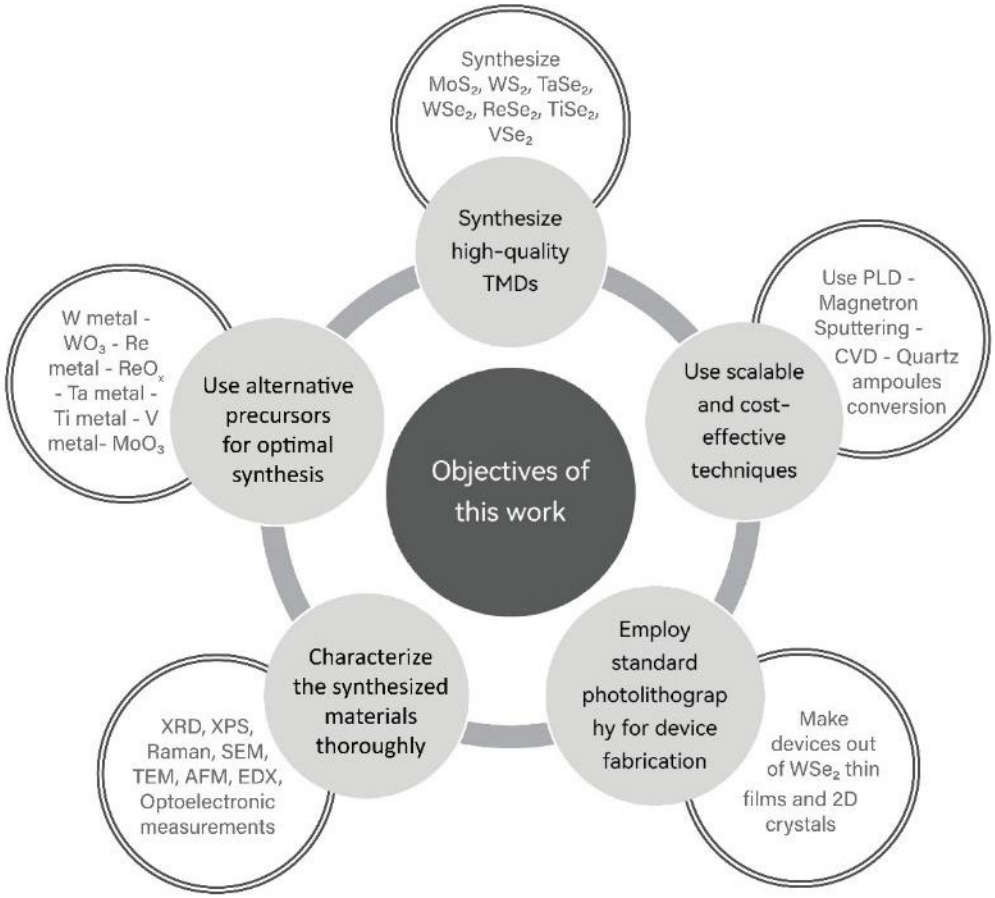

Figure 1.4: Directions of the desired results of this study to be obtained as the outcomes of this work illustration.

5. Showcase the use of standard photolithography and control the geometry of the produced TMD thin films to demonstrate the possible device fabrication as part of this methodology and its usability in various applications (e.g. photosensors).

All the research described in this dissertation was carried out in Institute of Solid State Physics of University of Latvia.

1.4 Scientific novelty

The research results presented in this thesis hold scientific significance and have been published in various international journals. To point the key novelties of the presented work here, following list is prepared:

- ***Comparison of two synthesis methodologies for growing GaN-MoS_2 and GaN-WS_2 core-shell nanowires:***

  The study explored two different methods for fabricating GaN-based core-shell nanowires, showing that by adjusting process parameters, it is possible to achieve uniform or island-like coatings with potential applications in energy and as photocatalysts for hydrogen production.

- ***Developed a robust method for fabricating core/shell nanowires with 2D TMD shells:***

This study presents a scalable four-step process for fabricating core/shell nanowires with a well-defined $TaSe_2$ shell, using a vacuum-sealed selenium atmosphere, demonstrating that this technique is versatile and applicable to a wide range of 2D chalcogenides.

- ***First-time synthesis of WSe_2 films using photolithography from WO_3 and W metal precursors:***

This work compared the characteristics of WSe_2 thin films synthesized from two distinct precursors, revealing that WO_3-based films generally had higher photocurrent and stability compared to those from W metal, suggesting that WO_3 is a more effective precursor for the CVT synthesis of WSe_2.

- ***First-time comparison of $ReSe_2$ films from Re metal and ReO_x precursors:***

The study introduced a novel method for $ReSe_2$ synthesis using atmospheric pressure CVT, showing significant differences in surface morphology based on precursor material and demonstrating potential for various applications, including non-linear optics.

- ***Developed a unique synthesis method for $TiSe_2$ and VSe_2 thin films with a 2-step process:***

This study used a scalable approach for the large-area synthesis of $TiSe_2$ and VSe_2 thin films, showing that both materials retained their continuity after selenization. This method provides opportunities to create continuous films on a large scale, with broader applications and extension to other TMDs.

1.5 Outline of this work

This work delves into the exciting realm of Transition Metal Dichalcogenides (TMDs), a class of materials with immense potential for next-generation electronics and optoelectronics. We begin by exploring the current state of the field and the key motivations driving our research (Chapter 1). Here, we identify existing challenges and highlight the specific TMDs targeted in this study (MoS_2, WS_2, $TaSe_2$, $ReSe_2$, $TiSe_2$, and VSe_2). We then clearly outline the objectives of our research, emphasizing the scientific novelty brought by our approach (Chapter 1.3-1.5).

Chapter 2 lays the groundwork by providing a fundamental understanding of TMDs and delves into various synthesis techniques employed for their fabrication in this work and to explore what concepts they were utilized. Chapter 3 focuses on the creation of heterostructures – novel structures combining different TMDs – with a specific emphasis on MoS_2/WS_2 grown on GaN nanowires and $TaSe_2$ grown on ZnS nanowires with an intermediary layer (Chapter 3.1-3.2). This chapter concludes by discussing the key results and their potential implications. Chapter 4 explores the growth of individual TMD thin films, investigating materials such as WSe_2, $ReSe_2$, $TiSe_2$, and VSe_2 (Chapter 4.1-4.3). Here, we detail the specific synthesis processes employed and present the key findings associated with each study.

Finally, Chapter 5 serves as a comprehensive summary, revisiting the initial objectives and evaluating our success in achieving them. Chapter 6 concisely presents the main theses of the work, providing a clear takeaway for the reader.

This work offers valuable insights into the synthesis of various TMD materials and heterostructures, paving the way for further exploration of their potential in advanced technological applications.

2. General topics

2.1 Fundamentals of Transition Metal Dichalcogenides

Transition metal dichalcogenides are a class of materials composed of layers of transition metal atoms sandwiched between layers of chalcogen atoms (sulphur, selenium, or tellurium) [86,87]. This unique layered structure imparts TMDs with a distinctive set of properties that have garnered significant attention in recent years [72,88–90]. The fundamental building block of TMDs is a single layer, often referred to as a monolayer. The weak van der Waals forces between these layers provide TMDs with their characteristic flexibility and ability to be exfoliated into individual layers. This layered structure is responsible for many of the remarkable properties exhibited by TMDs, including their exceptional mechanical flexibility, high surface area, and anisotropic electrical and optical properties [91–94].

A critical aspect of TMD behaviour is the concept of lattice matching. The lattice structure of a material refers to the arrangement of its atoms in a repeating pattern. When two materials with similar lattice parameters are brought into proximity, they can form a commensurate interface, where the atomic lattices align coherently. This lattice matching is crucial for the formation of high-quality heterostructures, which are composed of multiple layers of different materials stacked on top of each other [95,96]. For instance, the lattice mismatch between molybdenum disulfide (MoS_2) and hexagonal boron nitride (h-BN) is relatively small, allowing for the creation of high-quality heterostructures with minimal interfacial defects [45,97]. This has enabled the study of the electronic properties of MoS_2 in isolation, as well as the exploration of new phenomena arising from the interaction between the two materials. On the other hand, the lattice mismatch between MoS_2 and graphene is larger, leading to the formation of Moiré patterns at the interface [98,99]. These Moiré patterns can significantly modify the electronic properties of the heterostructure, giving rise to new electronic states and flat bands. Lattice mismatch can also play a role in the formation of defects and strain at the interface between two materials. While these defects can sometimes be detrimental to device performance, they can also introduce new and interesting properties. For example, strain-induced bandgap modulation has been observed in TMD heterostructures, offering opportunities for tuning the optical and electronic properties of these materials [12,14,100].

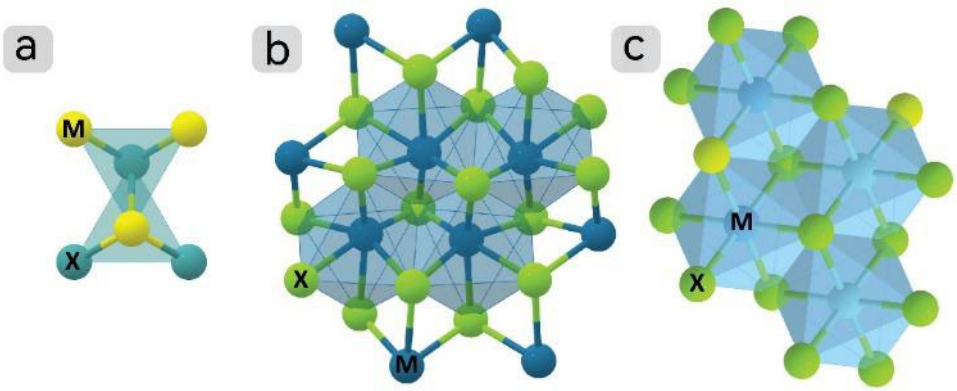

Figure 2.1: Graphical crystal structures of (a) hexagonal structure with a space group of $P6_3/mmc$ (b) triclinic crystal system with a space group of P-1 and (c) hexagonal crystal structure with a space group of P-3m1 where M represents atoms of Transition metals and X represents Chalcogen group atoms (S, Se). [106]

Understanding the interplay between layered structure and lattice matching is essential for the rational design and fabrication of TMD-based devices. By carefully selecting materials with compatible lattice parameters and controlling the growth conditions, it is possible to create high-quality heterostructures with desired properties [48,101–103]. As research in this field continues to advance, we can expect to see even more exciting developments in the field of TMD-based materials and devices. Below are some of the fundamental properties of the TMDs part of this work:

- MoS_2 (Molybdenum Disulfide): MoS_2 has a hexagonal crystal system *(fig. 2.1)* with a space group of $P6_3/mmc$ (194). The lattice parameters are a = 3.161 Å and c = 12.295 Å. MoS_2 is stable in its hexagonal phase and thermodynamically stable. The formation energy is -1.09 eV/atom, and it has a density of 5.06 g/cm^3. MoS_2 is known for its use in electronic and optoelectronic applications due to its unique electrical properties [104–106]. For this material, 2H phase is the most stable one, but there is also a metastable 1T phase [105].
- WS_2 (Tungsten Disulfide): WS_2 crystallizes in a hexagonal structure with a space group of $P6_3/mmc$ (194). The lattice parameters are a = 3.153 Å and c = 12.32 Å. It is thermodynamically stable in its hexagonal phase. The formation energy is -1.13 eV/atom, and a density of 7.54 g/cm^3. WS_2 is also notable for its potential in electronics and catalysis [106–109]. For WS_2 2H phase is the stable form, while the 1T phase is less common and less stable [107,109].
- $TaSe_2$ (Tantalum Diselenide): $TaSe_2$ has a hexagonal crystal system with a space group of $P6_3/mmc$ (194). The lattice parameters are a = 3.434 Å and c = 12.706 Å. It is stable in its hexagonal phase and thermodynamically stable. The formation energy is -0.80 eV/atom and a density of 9.16 g/cm^3. $TaSe_2$ is known for its superconducting properties and potential applications in electronics [106,110–112]. Both 2H and 1T phases are known, with the 2H phase being more stable at room temperature for $TaSe_2$ [110,112].
- WSe_2 (Tungsten Diselenide): WSe_2 forms a hexagonal crystal structure with a space group of $P6_3/mmc$ (194). The lattice parameters are a = 3.288 Å and c = 12.96 Å. It is stable in its hexagonal phase and thermodynamically stable. The formation energy is -1.03 eV/atom and it has a density of 9.32 g/cm^3. WSe_2 is used in electronics and optoelectronics due to its favourable electronic properties [71,106,113,114]. 2H phase is the most stable under normal conditions for WSe_2, but there is also a less common 1T phase [71,114].
- $ReSe_2$ (Rhenium Diselenide): $ReSe_2$ has a triclinic crystal system *(fig. 2.1)* with a space group of P-1 (2). The lattice parameters are a = 6.732 Å, b = 6.609 Å, and c = 6.626 Å. It is thermodynamically stable. The formation energy is -0.91 eV/atom and a density of 7.33 g/cm^3. $ReSe_2$ is noted for its unique anisotropic properties [51,106,115,116]. The triclinic phase is known to be the most stable under normal conditions [115,116].
- $TiSe_2$ (Titanium Diselenide): $TiSe_2$ has a hexagonal crystal structure with a space group of P-3m1 (164) *(fig. 2.1)*. The lattice parameters are a = 3.538 Å and c = 6.008 Å. It is thermodynamically stable in its hexagonal phase. The formation energy is -0.80 eV/atom and a density of 4.95 g/cm^3. $TiSe_2$ is known for its charge density wave properties and potential applications in electronics [106,117–119]. The 1T phase is the known stable phase under normal conditions [117,119].
- VSe_2 (Vanadium Diselenide): VSe_2 crystallizes in a hexagonal structure with a space group of P-3m1 (164). The lattice parameters are a = 3.356 Å and c = 6.108 Å. It is stable in its hexagonal phase. The formation energy is -0.67 eV/atom and a density of 5.81 g/cm^3. VSe_2 is noted for its potential use in energy storage and electronic applications [106,120–122]. 1T phase is the most stable one. VSe_2 can also exhibit charge density wave transitions [121,122].

The electrical properties of TMDs exhibit a remarkable diversity, ranging from metallic to semiconducting behaviour, and even superconductivity in certain conditions. These properties are

primarily determined by the number of layers, the specific transition metal and chalcogen elements, and external factors such as applied strain and electric fields. Bulk TMDs are generally indirect bandgap semiconductors, meaning that the energy required to excite an electron from the valence band to the conduction band is minimized when the electron and hole have different momenta[23,123,124]. This indirect bandgap nature limits their efficiency in optoelectronic applications. However, a dramatic transformation occurs as the material is thinned down to the monolayer limit. Most TMD monolayers exhibit a direct bandgap, implying that the energy minimum in the conduction band and the energy maximum in the valence band occur at the same point in momentum space. This transition from indirect to direct bandgap significantly enhances the optical properties of TMD monolayers and has spurred intense research in optoelectronics [125,126].

Beyond the bandgap nature, the carrier type (electrons or holes) in TMDs can also vary. Some TMDs, such as $MoTe_2$, exhibit a transition from semiconducting to metallic behaviour as the number of layers decreases [127,128]. This layer-dependent metal-semiconductor transition is attributed to changes in the electronic band structure caused by quantum confinement effects. Under specific conditions, TMDs can also exhibit superconducting properties. For instance, under high pressure, some TMDs have been found to transition into a superconducting state. The mechanism behind superconductivity in TMDs is still under investigation, but it is believed to be related to the interplay between electron-phonon coupling and electron-electron interactions [129,130]. Another intriguing phenomenon related to the electronic properties of TMDs is the formation of charge density waves (CDWs). A CDW is a periodic modulation of the electron density within a material. In TMDs, CDWs can arise due to the interplay between electron-electron interactions and the lattice structure. The formation of CDWs can lead to a variety of electronic and structural phase transitions, often accompanied by changes in electrical conductivity and magnetic properties. The coexistence of superconductivity and CDW order in TMDs is a topic of intense research interest [83,131,132]. Understanding the relationship between these two phenomena is crucial for designing novel superconducting materials.

The inherent electrical characteristics of transition metal dichalcogenides (TMDs) can be significantly influenced and tailored through a variety of external factors. This malleability is a cornerstone of their potential applications in advanced electronic and optoelectronic devices. One critical method to modify TMD properties is through the application of strain. When a TMD material is subjected to mechanical stress, its atomic lattice structure is distorted. This distortion directly impacts the electronic band structure, which is essentially the energy levels available for electrons to occupy [133–135]. By carefully controlling the type and magnitude of strain, it is possible to induce substantial changes in the bandgap, transforming a material from a semiconductor to a metal, or vice versa. This phenomenon, known as strain engineering, offers unprecedented control over the electrical behaviour of TMDs. In addition to strain, the introduction of defects or impurities into the TMD lattice can profoundly alter its electrical properties. These imperfections disrupt the regular arrangement of atoms, creating localized energy states within the bandgap. These states can act as electron traps or donors, significantly influencing the carrier concentration and mobility [134,135]. For instance, doping TMDs with specific elements can introduce additional charge carriers, enhancing conductivity [136–138]. Conversely, the creation of defects can act as scattering centres, reducing carrier mobility and affecting the overall electrical performance. The ability to manipulate the electrical properties of TMDs through strain engineering and defect engineering provides a powerful toolkit for materials scientists and device engineers. By carefully controlling these parameters, it is possible to optimize TMD materials for specific applications, such as high-performance transistors, light-emitting diodes, and energy storage devices. Moreover, the combination of these techniques with other methods, such as electric field effects and chemical

doping, opens up even greater possibilities for tailoring TMD properties to meet the demands of emerging technologies.

The versatility of TMDs in responding to external stimuli underscores their potential as a platform for groundbreaking advancements in electronics and optoelectronics. As research in this field progresses, the development of increasingly sophisticated devices that leverage the unique electrical properties of these remarkable materials can be expected.

2.2 Common Synthesis Techniques overview

From a variety of synthesis techniques for TMDs, a brief summary of each used technique in this work is discussed from their fundamental working to their usage *(fig. 2.2)*.

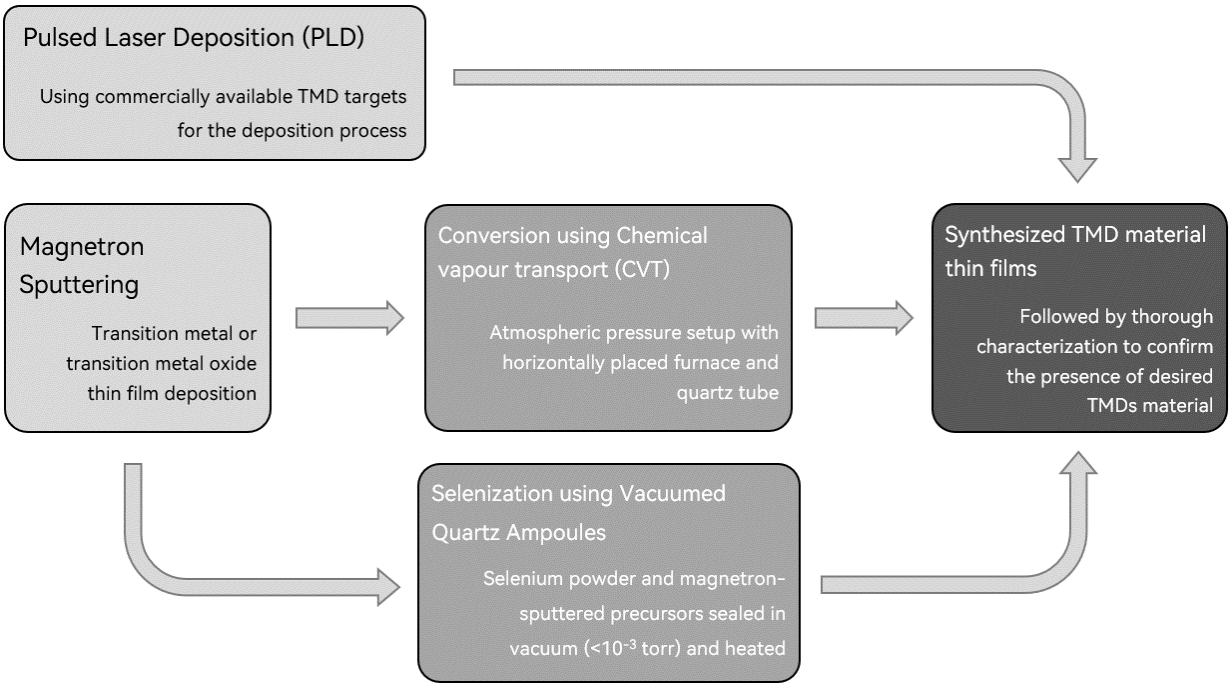

Figure 2.2: Flow chart of the three different methodologies consisting of at times more than one technique for the synthesis of TMDs films (left to right) in this work.

Pulsed laser deposition (PLD) is an advanced thin film deposition technique used extensively for producing high-quality films of various materials, including transition metals and their oxides. This process utilizes high-power laser pulses to ablate material from a target, which then deposits onto a substrate to form a thin film. PLD is known for its ability to precisely control film composition and structure, making it ideal for complex materials and heterostructures *(fig. 2.3)* [76,77].

The PLD process begins with selecting a target material, typically a high-purity transition metal or metal oxide. The target is placed in a vacuum chamber, which is then evacuated to achieve a low-pressure environment, often with a background gas such as oxygen for oxide films. A high-energy laser, usually an excimer or Nd:YAG laser, is directed through a window into the chamber, where it focuses onto the target material. The laser pulses ablate the target, creating a plume of ejected

material that travels towards the substrate. The substrate is positioned opposite the target, and its temperature can be controlled to influence the film's properties. As the ablated material condenses on the substrate, it forms a thin film with characteristics that can be precisely tailored by adjusting the laser parameters, such as energy, frequency, and pulse duration. The distance between the target and the substrate, as well as the ambient gas pressure, also play crucial roles in determining the film's morphology and quality. PLD offers several advantages for the deposition of transition metals and their oxides. One of the key benefits is its ability to maintain the stoichiometry of the target material, even for complex compositions. This is particularly important for oxides, where maintaining the correct oxygen content is critical for achieving desired electronic and optical properties. The high energy of the laser pulses ensures that even refractory materials can be efficiently ablated and deposited.

Additionally, PLD allows for the growth of epitaxial films and heterostructures with sharp interfaces, which are essential for applications in electronics, optoelectronics, and spintronics. By using multiple targets and rotating the substrate, multilayer films with distinct layers of different materials can be deposited in a single process, enabling the creation of advanced functional materials and devices. The properties of the deposited films can be further enhanced through post-deposition treatments such as annealing, which can improve crystallinity and reduce defects. The versatility and precision of PLD make it a valuable tool for research and development in materials science and nanotechnology.

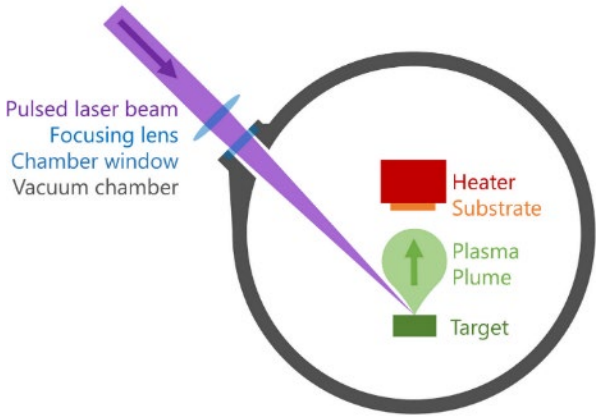

Figure 2.3: Simplified graphical illustration of the Pulsed Laser Deposition technique.

In summary, pulsed laser deposition is a powerful technique for creating high-quality thin films of transition metals and their oxides. By utilizing high-power laser pulses to ablate target materials in a controlled environment, PLD enables precise control over film composition and structure. This method is essential for producing advanced materials with tailored properties for a wide range of technological applications.

Magnetron sputtering is a versatile technique used for the deposition of thin films, particularly for transition metals and their oxides. This process involves ejecting material from a target using energetic ions generated in a plasma, which then deposit onto a substrate to form a thin film. Magnetron sputtering can be performed in either direct current (DC) or radio frequency (RF) modes, with DC sputtering being especially suitable for conductive materials like transition metals [139,140].

DC sputtering, in particular, is a widely used method for depositing transition metals and their oxides due to its efficiency and simplicity. In this process, a DC power supply is used to generate a plasma in a vacuum chamber, where argon ions are typically employed to bombard a metallic target. The impact of these ions causes atoms from the target to be ejected and subsequently deposited onto the substrate, forming a thin film. The deposition rate and film properties can be controlled by adjusting parameters such as the power applied to the target, the pressure of the argon gas, and the distance between the target and the substrate. The deposition of transition metals and their oxides via DC sputtering involves several critical steps. First, the target material, usually a high-purity transition metal or metal oxide, is selected based on the desired film properties. The target and substrate are then placed in the vacuum chamber, which is evacuated to create a low-pressure environment. Argon gas is introduced to maintain a plasma, and a DC voltage is applied to the target,

creating a glow discharge that ionizes the argon atoms. These ions are accelerated towards the target, causing sputtering of the target material, which then deposits onto the substrate*(fig. 2.4)*.

Transition metal oxides can also be deposited by DC sputtering, either by using an oxide target or by reactive sputtering, where a metal target is sputtered in the presence of a reactive gas like oxygen. This reactive sputtering process allows for the formation of oxide films with precise control over stoichiometry and composition. The properties of the deposited films, such as thickness, crystallinity, and electrical characteristics, can be tuned by varying the sputtering parameters. Post-deposition treatments, such as annealing, can further enhance the film properties by improving crystallinity and reducing defects. Magnetron sputtering, and specifically DC sputtering, is essential for creating high-quality thin films of transition metals and their oxides. These films have numerous applications, including in electronics, catalysis, and protective coatings, due to their excellent physical and chemical properties.

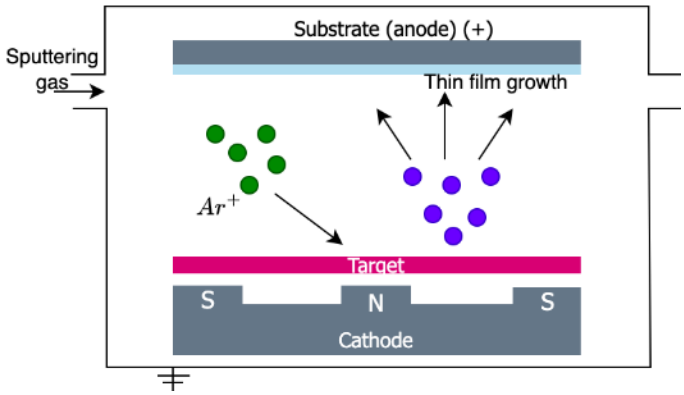

Figure 2.4: Graphical illustration for working principal of Magnetron Sputtering method.

In summary, magnetron sputtering, is a critical technique for depositing transition metals and their oxides. It involves sputtering material from a target in a controlled vacuum environment, allowing precise control over film properties. This method is integral to producing thin films for a wide range of advanced applications.

Chemical vapor deposition (CVD) has emerged as a powerful technique for synthesizing atomically thin transition metal dichalcogenide (TMD) crystals with precise control over their thickness, crystallinity, and morphology. In this process, precursor gases containing transition metal and chalcogen species react on a heated substrate, forming TMD thin films. To enhance the CVD synthesis of atomically thin TMD crystals, researchers have explored the use of salt as an additive. Rather than acting as a seed for crystal growth, salt serves to lower the energy required for the reaction between metal oxides and chalcogen species, thereby improving crystal growth. This enhancement occurs by increasing the partial pressure of TMD vapor at a given temperature [74,80].

The CVD synthesis process begins with the preparation of precursor gases and cleaning the substrate, often made of silicon dioxide (SiO_2) or sapphire. The substrate is then placed inside a CVD reactor. Precursor gases, typically delivered in a carrier gas such as hydrogen or argon, are introduced into the reactor at controlled flow rates. During deposition, the substrate is heated to temperatures ranging from a few hundred to a few thousand degrees Celsius. This elevated temperature facilitates the decomposition and reaction of precursor gases, leading to nucleation and growth of TMD crystals on the substrate surface. The growth mechanism of atomically thin TMD crystals via CVD involves nucleation, growth, and termination. Initially, nucleation sites form on the substrate surface as precursor gases adsorb and react to form atomic or molecular species. These nucleation sites then act as seeds for crystal growth. As the reaction progresses, TMD crystals continue to grow laterally and vertically on the substrate surface, dependent on precursor species diffusion and surface energy minimization. Growth rate and morphology can be controlled by adjusting parameters such as precursor flow rates, substrate temperature, and reactor pressure *(fig. 2.5)*.

The addition of salt to the precursor mixture lowers the energy barrier for reaction between metal oxides and chalcogen species. Salt reacts with the oxide creating a more reactive species of metal oxychlorides/hydro-oxychlorides which then in turn reacts with chalcogens to produce TMDs. This reduction in energy requirement promotes more efficient crystal growth by increasing the partial pressure of TMD vapor at a given temperature. Consequently, TMD crystals with improved crystallinity and uniformity are synthesized. The choice of substrate also influences TMD crystal growth. Substrates with lattice matching or similar thermal expansion coefficients to TMD crystals can promote epitaxial growth and enhance crystallinity. Surface properties, such as roughness and surface energy, can also affect nucleation and growth kinetics, making surface treatments or functionalization techniques important for optimizing growth conditions.

In conclusion, CVD offers a versatile and scalable approach for synthesizing atomically thin TMD crystals. The addition of salt as an additive in precursor mixtures can enhance crystal growth by reducing the energy barrier for reaction. By carefully controlling precursor chemistry, growth parameters, and substrate properties, researchers can achieve precise control over TMD crystal growth and tailor their properties for various applications.

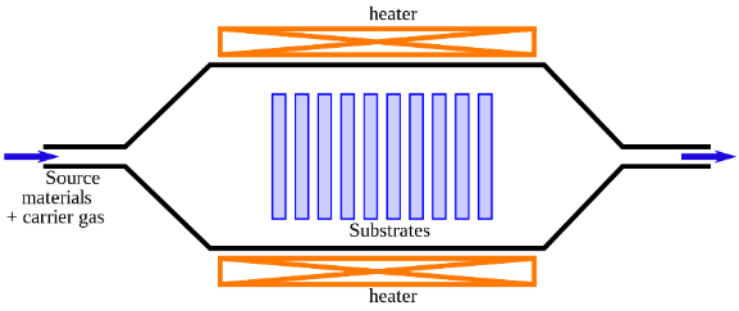

Figure 2.5: Schematics of the general working principal of Chemical vapour Deposition technique.

The adhesion of TMD thin films to substrates is crucial for their integration into devices and applications. Weak interlayer interactions in TMDs, such as van der Waals forces, can lead to poor adhesion and delamination from substrates. To improve adhesion, various strategies can be employed, including surface functionalization, interfacial engineering, and the use of adhesion promoters. Surface functionalization involves modifying the surface chemistry of substrates or TMDs to enhance adhesion through chemical bonding or interactions. The use of adhesion promoters or interlayers, such as graphene or hexagonal boron nitride (h-BN), can improve adhesion and mechanical stability by acting as intermediate layers between TMDs and substrates.

Quartz ampoule fabrication plays a crucial role in the synthesis of various materials, typically made of high-purity quartz glass, provide a sealed environment for conducting high-temperature reactions under controlled conditions [141]. These ampoules are used to house precursor materials and facilitate their conversion into TMD thin films through processes such as selenization or sulfurization.

The fabrication of quartz ampoules involves several steps to ensure their integrity and functionality for high-temperature reactions. First, high-quality quartz glass tubes are selected based on purity and thermal stability. These tubes are then cut to the desired length and cleaned thoroughly to remove any contaminants that could affect the reaction process. Next, the ampoules are sealed using a high-temperature torch or a specialized sealing machine to create a hermetic seal that prevents leakage of gases and maintains a controlled environment inside the ampoule during the reaction process *(fig. 2.6)*. In the synthesis of TMD thin films, quartz ampoules serve as reaction vessels for housing precursor materials and facilitating their conversion into TMDs through controlled thermal processes. One common approach involves depositing a transition metal precursor onto a substrate using techniques such as magnetron sputtering, as discussed earlier. The substrate with the precursor film is then placed inside a quartz ampoule along with a chalcogen source, such as sulphur (S) or selenium (Se). The sealed quartz ampoule is then placed in a high-

temperature furnace, where it undergoes heating to initiate the conversion of the precursor film into TMD thin films through sulfurization or selenization processes. The ampoule heating process creates a controlled environment with high partial pressures of Se/S vapor inside the ampoule, which is essential for promoting the reaction between the precursor film and the chalcogen vapor to form TMDs.

The vacuum conditions created inside the quartz ampoule play a critical role in controlling the precursor conversion process and determining the properties of the resulting TMD thin films. By maintaining a high vacuum or low-pressure inert gas atmosphere inside the ampoule, researchers can minimize unwanted chemical reactions and ensure the purity and stoichiometry of the TMD thin films. Furthermore, the high partial pressure of Se/S vapor inside the quartz ampoule promotes the efficient conversion of the precursor film into TMDs by providing a sufficient supply of chalcogen species for reaction with the transition metal precursor. This ensures the formation of high-quality TMD thin films with uniform composition and crystal structure.

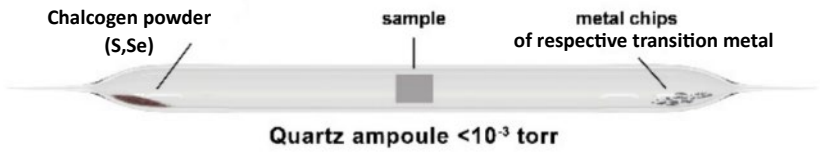

Figure 2.6: Graphical illustration of a quartz ampoule prepared during this study and its inside components before the heating process.

In summary, quartz ampoule fabrication plays a crucial role in the synthesis of TMD thin films through processes such as selenization or sulfurization. By combining techniques such as magnetron sputtering for precursor deposition with ampoule heating in a high-temperature furnace, researchers can control the conversion of precursor materials into TMDs under vacuum conditions with high partial pressures of Se/S vapor. This approach enables the production of high-quality TMD thin films with tailored properties for a wide range of applications in electronics, optoelectronics, catalysis, and beyond.

2.3 Material synthesis and investigation details

GaN nanowires and MoS_2/WS_2 shell synthesis: GaN NWs were synthesized via atmospheric pressure chemical vapour transport method in a horizontal quartz tube reactor. 2 g metallic Ga (99.999%, Alfa Aeasar) was loaded in a ceramic boat and placed in the centre of the quartz tube, oxidized silicon wafers SiO_2/Si (100) (Semiconductor Wafer, Inc.) coated with spherical Au nanoparticles (NPs, Alfa Aesar, water suspension, 100nm diameter) were placed downstream in a lower temperature region. Au NPs were used as a catalyst for the vapour-liquid–solid (VLS)mechanism. The reactor was heated to 940°C under a flow of carrier gas mixture Ar/H_2-35%, then gaseous NH_3 flow in 1:1 ratio to the carrier gas was introduced and maintained for 30 min for the gas-phase reaction and NW growth, followed by natural cooling to the room temperature under Ar/H_2 flow. As a result, 5–20 μm long GaN NWs were produced on the SiO_2/Si substrate. Few-layers of MoS_2 and WS_2 on GaN NWs were obtained with two different routes. The first route consists of two steps – deposition of amorphous MoO_3 and WO_3 coating on GaN NWs via reactive DC magnetron sputtering of a metallic target in a mixed Ar/O_2 atmosphere, followed by subsequent sulfurization of the samples in a quartz tube reactor at high temperatures. The optimal sacrificial precursor film thickness (on a flat substrate) was found to be 30 nm and 40 nm for MoO_3 and WO_3, respectively. Optimal sulfurization temperature was 750°C for MoS_2 and 800°C for WS_2 coatings. The second route

was pulsed laser deposition (PLD) from stoichiometric MoS_2 and WS_2 targets. 500 mJ 248 nm KrF laser beam was used for target ablation at 10Hz repetition frequency and 10^{-5} Torr background pressure. A few-layer MoS_2 coating was obtained with 1500 pulses at 600°C substrate temperature, and WS_2 coating with 3000 pulses at 650°C substrate temperature.

ZnS nanowires and Al_2O_3-$TaSe_2$ shell synthesis: Zinc sulphide (ZnS) nanowires (NWs) were synthesized on oxidized silicon (Si/SiO_2) substrates (Semiconductor Wafer, Inc., Hsinchu, Taiwan) using a vapor-liquid-solid (VLS) growth mechanism. Gold nanoparticles (50 nm in diameter) (BBI International, Grand Forks, ND, USA) served as catalysts for the growth process. ZnS powder (0.4 g, >97%, Sigma Aldrich, St. Louis, MO, USA) was thermally sublimated at 950°C in a quartz tube reactor, and the resulting vapor was carried by an Ar/H_2-5% gas mixture to the substrate. Subsequently, an aluminium oxide (Al_2O_3) layer, approximately 6 nm thick, was deposited on the ZnS NWs using atomic layer deposition (ALD) at 150°C in a Savannah S100 reactor. Trimethylaluminum (TMA) and H_2O were used as precursors, with N_2 serving as the carrier gas. A thin layer of tantalum (Ta), approximately 15 nm thick, was deposited onto the ZnS/Al_2O_3 NWs using direct current (DC) magnetron sputtering from a Ta target (GoodFellow, Huntingdon, UK) in an argon atmosphere. Finally, the coated NWs were annealed in a selenium environment at 650 °C to transform the Ta layer into tantalum diselenide ($TaSe_2$). The annealing process was conducted in a vacuum-sealed quartz ampoule containing selenium pellets (50 mg, Sigma Aldrich) and Ta foil (100 mg, GoodFellow, Huntingdon, UK) to maintain a stable vapor pressure of $TaSe_2$ and minimize the vapor's transport to cooler areas of the ampoule.

Tungsten diselenide film synthesis: Sacrificial precursor films with varying thicknesses, from 3 nm to 50nm, were deposited on oxidized silicon wafers SiO_2/Si (100) (Semiconductor Wafer, Inc.) by reactive DC magnetron sputtering of a metallic tungsten target in a mixed Ar/O_2 atmosphere ($5\cdot10^{-3}$ torr, 30 sccm Ar, and 20 sccm O_2 gas flow at 300 W DC power). After the precursor material deposition, synthesis of WSe_2 was performed from W metal film and WO_3 film using CVT. The CVT setup consists of a horizontal open-end quartz tube reactor. For the procedure, selenium powder was loaded in a ceramic boat at one end of the quartz tube. The vapour of selenium was transported downstream to the W/WO_3 precursor material on a silicon substrate using the carrier gas mixture: Ar/H_2-5% in the case of WO_3 and 35% Ar/H_2 in the case of W. The temperatures (ranging from 600 to 850°C) were held constant for 20 min, followed by uninterrupted cooling to the room temperature.

Rhenium diselenide film synthesis: A two-step approach was employed, starting with the deposition of thin rhenium (Re) and rhenium oxide (ReO_x) films with thicknesses ranging between ~10 and 70 nm on substrates of a ~1 cm^2 square (cut by a diamond scriber) size at room temperature by reactive DC magnetron sputtering of a metallic rhenium target (99.9%) in an Ar or mixed Ar/O_2 (20 sccm: 10 sccm) atmosphere ($5\cdot10^{-3}$ torr, 100 W DC power). Prior to the magnetron deposition of the precursor thin films, the substrates underwent a cleaning process. This involved immersing them in an ultrasonic bath with acetone for 3 min, followed by a subsequent 3 min ultrasonic bath in deionized water (DIW). After the ultrasonic cleaning, the substrates were blow-dried using nitrogen (N_2) gas to ensure the removal of any residual contaminants. These deposited precursor films served as the foundation for the subsequent conversion to $ReSe_2$ via CVT. The CVT setup was operated at atmospheric pressure using a 5% H_2/Ar gas mixture. The temperature range tested was from 550°C to 1000°C, with a process duration of 15 min (with a pre-heated furnace), and selenium powder (99.99%, Sigma Aldrich, St. Louis, MO, USA) placed at the intake end of the carrier gas. The furnace used here exhibited a temperature gradient, maintaining the target temperature primarily within the central 5 cm region, beyond which, the temperature decreased. Depending on the selected process temperature, the selenium powder was positioned in a zone where the temperature reached 350–400°C to facilitate its evaporation, to be carried by the flow of the carrier gas to placed samples.

Titanium and Vanadium diselenide film synthesis: Cleaned 10 mm^2 sapphire substrates (r-plane, Biotain Crystal Co.) were prepared using standard ultrasonic cleaning techniques with acetone and DI water. Thin films of Ti or V metal, approximately 15 nm thick, were deposited onto the cleaned substrates using DC magnetron sputtering in an argon atmosphere ($3 \cdot 10^{-3}$ torr, 30 sccm Ar, at 100 W DC power). The ampules were made from quartz tubes of 13 mm OD with 1 mm wall thickness and length of 120 ± 10 mm, were loaded with the metal-coated sapphire substrate, 50 mg of selenium powder, and 100 mg of grinded metal chips to absorb excess selenium. After lowering the pressure inside to $<10^{-3}$ torr, they were sealed and heated in a horizontal furnace at 650°C, 700°C, or 750°C for an hour, followed by rapid cooling to room temperature by exposing these ampoules to atmosphere.

Details of the investigative tools used:

- X-ray Diffraction (XRD): Rigaku MiniFlex 600 X-ray powder diffractometer with Cu Kα radiation (λ = 1.5406 Å). Rietveld analysis was performed using the BGMN program.
- X-ray Photoelectron Spectroscopy (XPS): ESCALAB Xi spectrometer from ThermoFisher with an Al Kα X-ray tube.
- Transmission Electron Microscopy (TEM): Tecnai GF20, FEI, operating at 200 kV.
- Scanning Electron Microscopy (SEM): Lyra, Tescan, and Helios 5 UX, Thermo Fisher Instruments.
- Energy Dispersive X-ray Spectroscopy (EDX): X-Max detector, SATW window.
- Optical Microscopy: Standard optical microscope.
- Atomic Force Microscopy (AFM): PARK NX10, Suwon, Korea.
- Hall Effect Measurement: HMS5000, Ecopia Hall Effect Measurement Systems.
- Spectrophotometry: Cary 7000 spectrophotometer, Agilent.
- Z-scan Measurement: ORPHEUS-HP + PHAROS PH2 femtosecond laser.
- Micro-Raman Spectroscopy: TriVista 777 confocal Raman system, Princeton Instruments.
- Photoresponse and I-V Measurements: Two-contact microprobe station, low-noise current preamplifier (SR570, Stanford Research Systems), oscilloscope (TDS2004B, Tektronix), and 405 nm semiconductor diode laser.

2.4 Unique Concepts explored in this work

Nanowires as substrate: The integration of TMDs with nanowires presents exciting opportunities, but it also introduces unique challenges. One of the critical factors to consider is the lattice mismatch between the TMD and the nanowire substrate [47,142,143]. A significant lattice mismatch can lead to strain, defects, and ultimately, a degradation in the electronic properties of the TMD layer. Careful selection of nanowire materials with lattice parameters closely matching those of the desired TMD is crucial to achieve high-quality heterostructures. Additionally, the chemical reactivity between the TMD and the nanowire substrate must be considered. Incompatibility can lead to interfacial reactions, forming undesired compounds and degrading the overall device performance. Therefore, choosing a substrate material that is inert or exhibits controlled reactivity with the TMD is essential [142].

Despite these challenges, the benefits of using nanowires as substrates for TMD growth are substantial. One of the primary benefits of using nanowires as substrates is the increased surface area available for TMD growth [47,144,145]. This can lead to enhanced material utilization and improved device performance. Additionally, the high aspect ratio of nanowires can facilitate efficient charge carrier transport along the wire axis, which is crucial for many electronic applications [146]. This is particularly beneficial for devices such as field-effect transistors (FETs) where high carrier mobility

is essential. Moreover, the curvature of the nanowire surface can induce strain in the grown TMD layer. This strain can modify the electronic band structure of the TMD, leading to tuneable properties. For instance, it can induce a bandgap shift or modify carrier mobility. This ability to control material properties through strain engineering opens up new possibilities for designing tailored devices [146,147]. The integration of TMDs with nanowires can also create unique device architectures. For example, core-shell nanostructures, where a TMD layer encapsulates a nanowire core, can exhibit enhanced properties due to synergistic effects between the two materials. Such structures have potential applications in energy storage, catalysis, and sensing [148].

To summarize, employing nanowires as substrates for TMD growth offers a versatile platform for exploring new device concepts and functionalities. The combination of the high aspect ratio, increased surface area, and potential for strain engineering makes this approach highly promising for future technological advancements.

TMDs thin film growth in large area: The realization of the full potential of transition metal dichalcogenides necessitates the development of efficient methods for producing large-area, high-quality thin films. Several techniques have emerged as promising candidates for this purpose. Physical vapor deposition (PVD) methods, including PLD and magnetron sputtering, offer routes to deposit directly TMDs or their precursors onto large substrates. PLD, in particular, can achieve high deposition rates and excellent film quality, but it can be challenging to maintain uniformity over large areas [79]. Magnetron sputtering provides a more scalable approach, but often results in lower film quality compared to PLD. To convert these deposited precursors to TMDs, subsequent thermal processing is typically required. A common method involves annealing the films in a sulphur or selenium atmosphere within a vacuumed sealed quartz ampoule[149,150]. This approach allows for the pristine quality growth of TMD materials. However, achieving uniform and large-area TMD films through this method can be challenging due to temperature gradients and uncontrolled flow dynamics in the system[151].

While significant progress has been made in large-area TMD growth, challenges such as uniformity, defect density, and control over layer number persist. Addressing these issues is crucial for the successful commercialization of TMD-based devices. Moreover, the development of novel growth techniques that combine the advantages of different methods, such as hybrid approaches combining PVD and CVD, holds promise for overcoming these limitations [152–154]. The potential applications of large-area TMD thin films are vast. They encompass electronics, optoelectronics, energy storage, and catalysis. For instance, flexible electronics, transparent conductive films, and large-area photodetectors are among the potential applications that can benefit from the development of high-quality, large-area TMD films [153].

Choice of precursors: The selection of appropriate precursors is a critical factor influencing the quality and properties of grown TMD thin films. Traditionally, transition metal oxides have been employed as precursors due to their relative stability and availability. However, the conversion of these oxides to TMDs often requires high temperatures, which can introduce impurities and defects into the final product. In contrast, metallic precursors can offer advantages in certain cases [155,156]. Certain transition metals exhibit lower conversion temperatures compared to their oxide counterparts, reducing the risk of thermal decomposition and impurity incorporation. However, metal precursors may be more reactive and susceptible to humidity and oxidation, requiring careful handling and processing conditions [155].

The optimal precursor choice depends on various factors, including the desired TMD composition, target film thickness, and growth technique. For some TMDs, both metal and oxide precursors may be viable options, and a comparative study can help determine the most suitable approach [157–159]. To achieve ultrathin TMD crystals, which often demand precise control over thickness and

uniformity, salt-assisted chemical vapor deposition (CVD) has emerged as a promising technique [160–162]. By incorporating salts into the growth environment, the activation energy for TMD formation can be reduced, allowing the synthesis of high-quality TMDs under lower temperature conditions. This approach enables the synthesis of high-quality, large-area TMD films with atomically thin thicknesses.

In conclusion, the careful selection of precursors is essential for the successful growth of TMD thin films. By carefully considering the specific requirements of the target application and the limitations of different precursor types, researchers can optimize the growth process and produce high-quality TMD materials.

3. Producing Heterostructures with TMDs

3.1 MoS_2 and WS_2 grown on GaN nanowires

This study focused on the synthesis of GaN-MoS_2 and GaN-WS_2 core-shell nanowires using two distinct methods. The first approach involved a two-step process of sputter-deposition of a sacrificial transition metal oxide coating on GaN NWs followed by sulfurization. The second method utilized pulsed laser deposition of a few layers of TMDs on GaN NWs derived from MoS_2/WS_2 targets. Characterization results from both synthesis routes demonstrated that high-quality crystalline core-shell NW heterostructures could be achieved. The theoretical analysis supported the experimental findings by investigating the electronic structure of a model designed to replicate the structural properties of core-shell NWs, reinforcing the consistency and effectiveness of the proposed synthesis methods *(fig. 3.1)*.

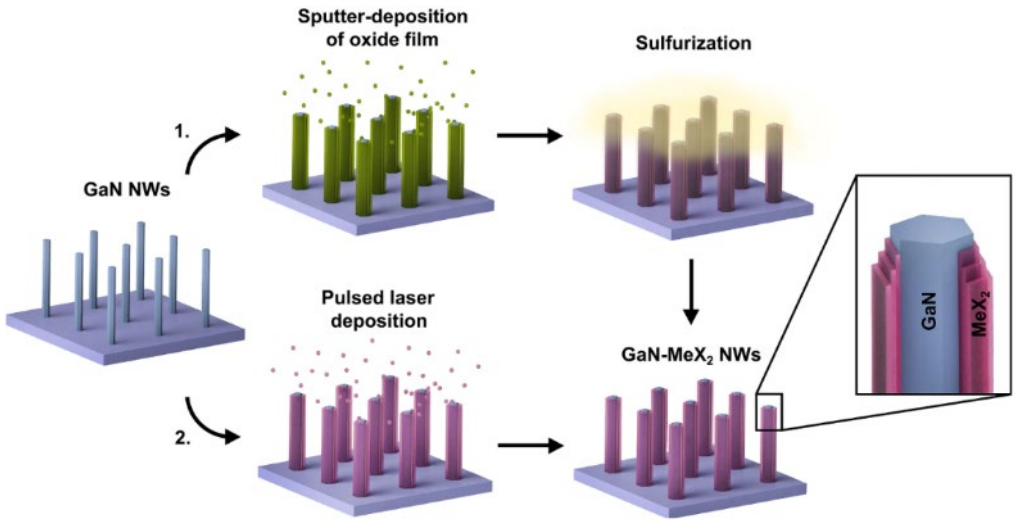

Figure 3.1: A schematic of both demonstrated GaN-MeX_2 core–shell NW preparation methods on Si/SiO_2 substrates: (1) two-step method, which includes sulfurization of pre-deposited metal oxide coating; and (2) direct deposition of MoS_2 or WS_2 with pulsed laser deposition

The morphology and internal structure of the as-grown core-shell nanowires (NWs) were analysed using TEM, while SEM confirmed that the NWs maintained their length after the shell deposition procedures. Lower magnification TEM images displayed the typical coating morphologies resulting from different MoS_2 and WS_2 synthesis methods. PLD and pre-deposited WO_3 sulfurization yielded a smooth and uniform shell around NWs, whereas MoO_3 sulfurization at optimal conversion temperatures led to a non-uniform island-like coating. Although a uniform shell is often crucial for good electrical properties, a higher surface roughness can be advantageous for energy applications due to increased active edge sites on the TMD shell, with the NW core maintaining its highly crystalline structure.

Higher-resolution TEM images *(fig. 3.2)* revealed the inner crystalline structure of the synthesized nanostructures, showing the parallel black and white lines that represent the atomic planes of the

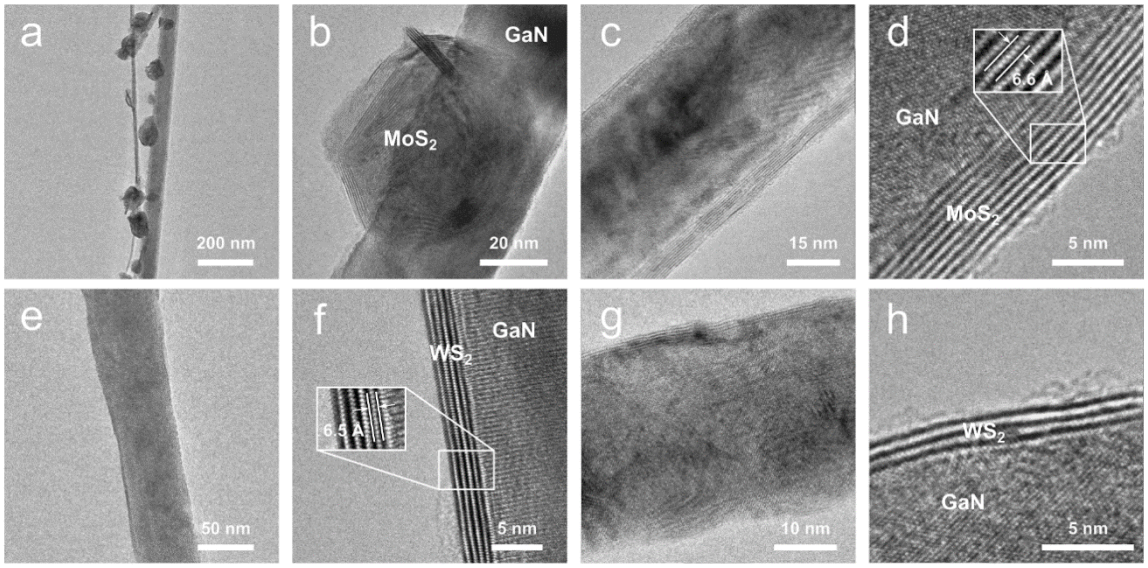

Figure 3.2: Transmission electron microscope images at different magnifications of individual (a-b) GaN-MoS_2 NW prepared via MoO_3 coating sulfurization, (c-d) GaN-MoS_2 NW prepared via pulsed laser deposition, (e-f) GaN-WS_2 NW prepared via WO_3 coating sulfurization, (g-h) GaN-WS_2 NW prepared via pulsed laser deposition; the insets show the measured d-spacings.

MeX_2 shells. The typical thickness of uniform coatings varied from 4 to 10 monolayers, but with careful control, single-monolayer deposition was also achievable. The measured interplanar distance values for MoS_2 ranged from 6.4 to 6.6 Å, and for WS_2 from 6.2 to 6.5 Å, consistent with the known lattice parameters for bulk MoS_2 and WS_2[46,163]. The single-crystalline nature of the GaN NW core

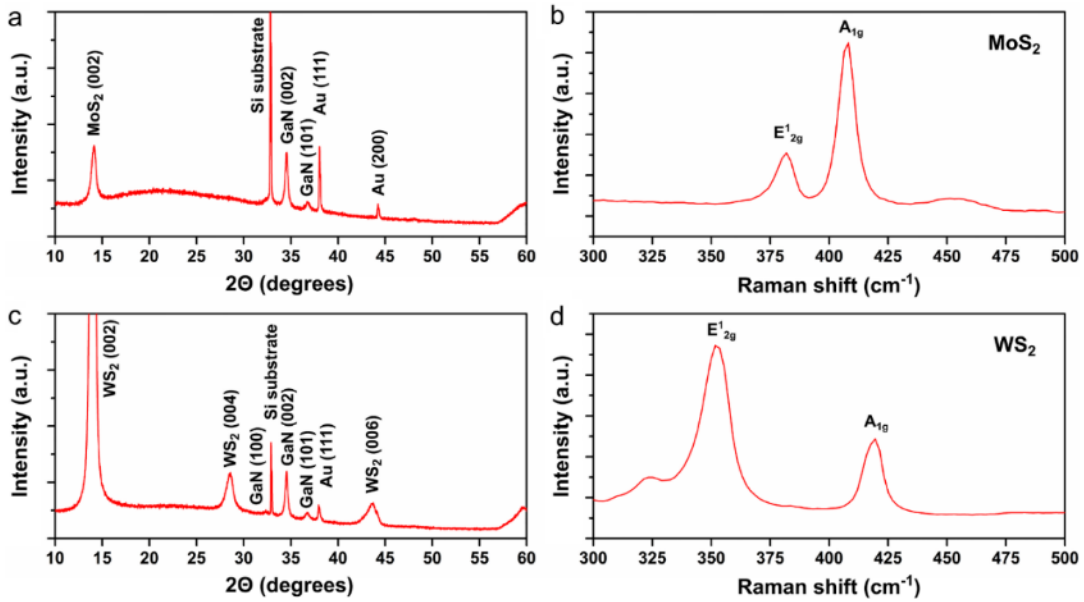

Figure 3.3: (a) X-ray diffraction and (b) micro-Raman spectrum of GaN-MoS_2 NW arrays on a Si/SiO_2 substrate; (c) X-ray diffraction and (d) micro-Raman spectrum of GaN-WS_2 NW arrays on a Si/SiO_2 substrate.

was also evident, with an interplanar distance closely matching the known values for hexagonal GaN.

The TEM measurements *(fig. 3.2)* highlighted the high crystalline quality of the prepared core-shell NWs, indicating their potential for further application in both electronic and energy-related fields.

To verify the phases present in the as-grown core–shell nanowire samples, X-ray diffraction measurements *(fig. 3.3)* were conducted on the NW arrays positioned on Si(100)/SiO_2 substrates. The results, focusing on nanostructures created using the two-step sacrificial coating method, revealed consistent Bragg peaks corresponding to the expected crystalline phases: hexagonal GaN NWs, MoS_2 shells, and WS_2 shells [164,165]. This confirmation aligned with the data obtained from TEM. Additionally, the XRD patterns contained peaks related to the silicon substrate and gold nanoparticles used for vapor-liquid-solid growth. These findings corroborate the TEM observations and demonstrate that the desired phases were achieved in the core–shell NWs.

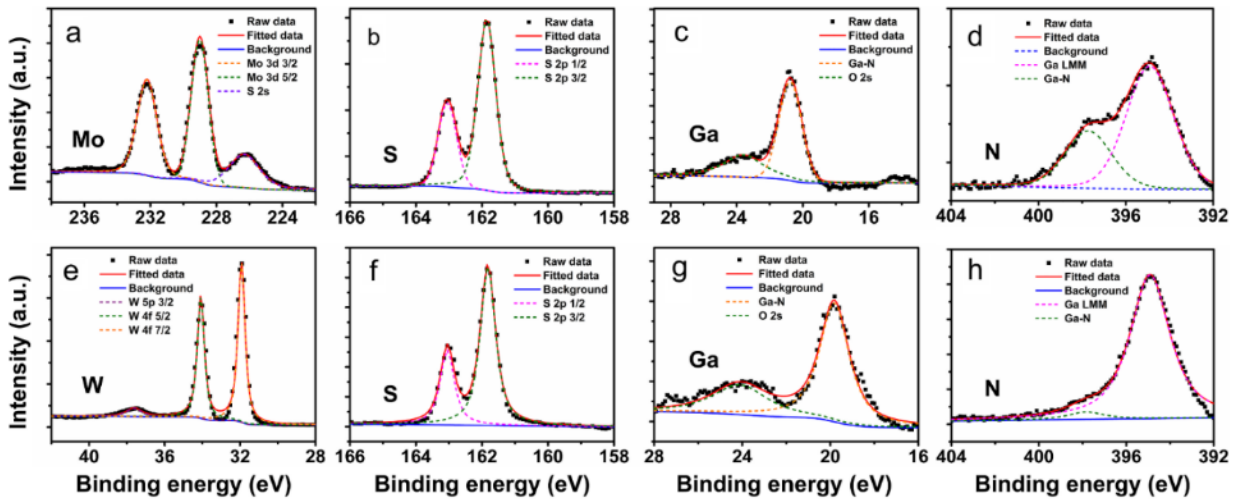

Figure 3.4: High-resolution XPS core-level spectra and peak fits of GaN-MoS_2 core–shell NWs for (a) Mo 3d, (b) S 2p, (c) Ga 3d and (d) N 1 s. High-resolution XPS core-level spectra and peak fits of GaN-WS_2 core–shell NWs for (e) W 4f, (f) S 2p, (g) Ga 3d and (h) N 1s

Room-temperature micro-Raman spectroscopy *(fig. 3.3)* was employed to further confirm the presence of WS_2 and MoS_2 in the core–shell nanostructures. The Raman spectrum of GaN-MoS_2 NWs exhibited characteristic peaks for the in-plane E^1_{2g} mode at 383cm^{-1} and the out-of-plane A_{1g} mode at 408 cm^{-1}, indicating the successful formation of MoS_2 shells on GaN NWs. Similarly, the Raman spectrum for GaN-WS_2 NWs showed two distinct bands at 352cm^{-1} and 420cm^{-1}, corresponding to the E^1_{2g} and A_{1g} modes, respectively [164,165]. These spectroscopic results confirmed the presence of the expected TMD layers in the nanostructures, further validating the effectiveness of the synthesis process used in this study.

An X-ray Photoelectron Spectroscopy (XPS) analysis *(fig. 3.4)* was conducted to confirm the chemical composition of core-shell nanowire (NW) arrays on Si(100)/SiO_2 substrates. High-resolution spectra were obtained for Mo 3d, W 4f, S 2p, Ga 3d, and N 1s peaks, with all data calibrated relative to the adventitious C 1s peak at 285 eV binding energy. For both the GaN-MoS_2 and GaN-WS_2 samples, the S 2p peaks consisted of spin–orbit doublets ($\Delta_{3/2\text{-}1/2}$ = 1.2 eV), with the $2p_{3/2}$ peak measured at 161.8 eV, aligning with MoS_2 and WS_2 compounds. In the GaN-MoS_2 nanowires, the Mo 3d peak displayed a spin–orbit splitting ($\Delta_{5/2\text{-}3/2}$ = 3.2 eV), with the Mo $3d_{5/2}$ component at 229.0 eV, consistent with the MoS_2 chemical state. Additionally, the S 2s peak at 226.2 eV was observed in the scan. In the GaN-WS_2 nanowires, the W $4f_{7/2}$ peak for the WS_2 chemical state was measured at 32.0 eV, with a spin–orbit splitting ($\Delta_{7/2\text{-}5/2}$ = 2.2 eV) [166,167].

The close lattice constants between GaN substrates and dichalcogenides result in a geometric mismatch of only 1.8% during stacking. The alignment of Ga and S atoms resembles the arrangement found between Ga and N atoms in bulk GaN. The constructed 2D nano heterostructure shows that the distance between Ga atoms in the middle is 3.18 Å, indicating adequate substrate thickness. The relaxation of atomic positions is more pronounced at the GaN substrate edges, ranging from 3.02 Å to 3.21 Å. The gap between the GaN and WS_2 or MoS_2 layers decreases from 4.25 Å to 4.24 Å for WS_2@GaN and increases to 4.27 Å for MoS_2@GaN as the number of layers grows. The band edge diagram *(fig. 3.5)* for WS_2-on-GaN and MoS_2-on-GaN nano heterostructures shows that the free-standing monolayers have their valence band (VB) tops below the oxygen redox potential and conduction band (CB) bottoms above the standard hydrogen electrode (SHE). When these monolayers contact the GaN NW, the CB bottom is about 0.5 eV above SHE, indicating efficient hydrogen evolution during water splitting. The VB top of WS_2-on-GaN and MoS_2-on-GaN is around 1 eV above the oxygen redox level, suggesting potential water splitting with red and near-infrared irradiation [168,169]. These results point to WS_2-on-GaN and MoS_2-on-GaN core-shell NWs as promising candidates for photocatalysts in hydrogen production.

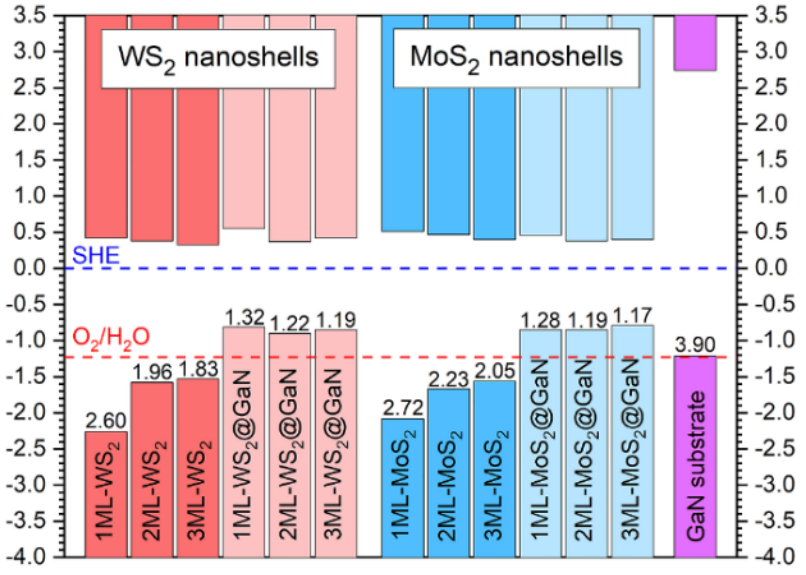

Figure 3.5: Schematic representation of the GaN-WS_2 and GaN-MoS_2 band edges positions with respect to the standard hydrogen electrode (SHE). Blue and red horizontal dashed lines correspond to the redox potentials for $H+/H_2$ and O_2/H_2O dissociation, respectively.

3.2 Growth of $TaSe_2$ on ZnS nanowire with Al_2O_3 as intermediary layer

This study presents a novel approach for fabricating $ZnS/Al_2O_3/TaSe_2$ core-shell nanowires (NWs). Utilizing pre-synthesized ZnS/Al_2O_3 NWs as a template, a thin tantalum (Ta) metal film is deposited via magnetron sputtering. Subsequent selenization at temperatures ranging from 650 to 750 °C within a vacuum-sealed quartz ampoule, employing a selenium precursor, results in the formation of the $TaSe_2$ shell. The proposed magnetron sputtering method offers a scalable and environmentally friendly alternative to traditional Ta-based TMD precursors by significantly reducing Ta consumption. The synthetic strategy outlined herein can be extended to the production of other core-shell NWs incorporating various layered 2D chalcogenide shells (e.g., selenides, sulphides) by substituting the Ta precursor with appropriate metal precursors. The $ZnS/Al_2O_3/TaSe_2$ core/shell nanowires (NWs) were fabricated using a four-step process *(fig. 3.6)*:

1. **Growth of ZnS NWs:** ZnS nanowires were grown on oxidized silicon wafers with a 50 nm thermal oxide layer, using gold nanoparticles (50 nm in diameter) as catalysts for the vapor–

liquid–solid mechanism. The ZnS powder was sublimated at 950°C in a quartz tube reactor for 30 minutes, and the ZnS vapor was carried to the substrates by an argon/hydrogen gas mixture, where the nanowires formed.

2. **Deposition of Al_2O_3 Layer:** Aluminium oxide (Al_2O_3) layers were deposited on the ZnS NWs using the atomic layer deposition (ALD) technique at 150°C, completing 66 cycles to achieve a thickness of about 6 nm. Trimethylaluminum (TMA) and water were used as precursors, with nitrogen serving as the inert carrier gas.
3. **Magnetron Sputtering of Ta Thin Film:** A tantalum (Ta) layer, approximately 15 nm thick on flat substrates, was sputtered onto the ZnS/Al_2O_3 NWs using direct current (DC) magnetron sputtering from a Ta target in an argon atmosphere. The actual thickness of the Ta film on the vertical NWs may be less than 15 nm due to the substrate's geometry.

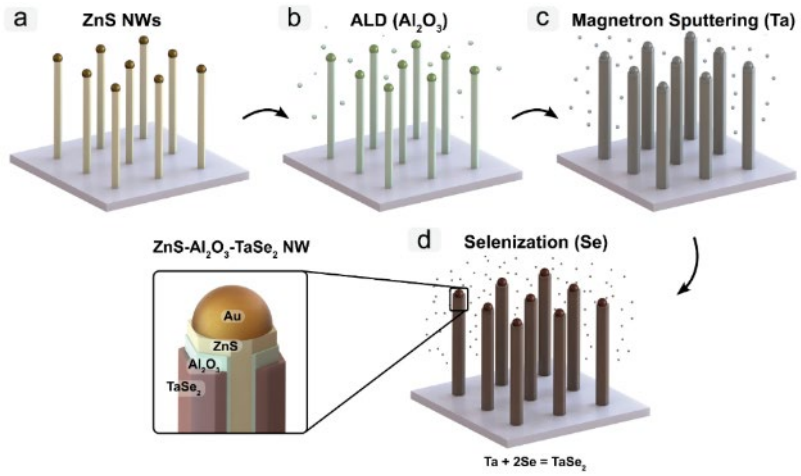

Figure 3.6: A scheme for the four-step method for the fabrication of ZnS/ Al_2O_3/ $TaSe_2$ core/shell NWs. Growth of ZnS NWs via VLS mechanism using Au NPs catalysts (a). Al_2O_3 layer deposition by ALD around ZnS NWs (b). Ta thin film deposition on ZnS/Al_2O_3 NWs (c). Selenization of Ta thin film and formation of NWs ZnS/Al_2O_3/$TaSe_2$ NWs (d)

4. **Selenization of Ta to $TaSe_2$:** The coated NWs underwent a selenization process through annealing in a selenium-rich environment. This was achieved by sealing the NWs within a vacuum-sealed quartz ampoule with selenium pellets and additional Ta foil to maintain a stable vapor pressure. The ampoule was placed in an oven and annealed at 650°C for 50 minutes, ensuring the transformation of the Ta layer into $TaSe_2$. The setup of the ampoule ensured cooler ends, allowing any unreacted selenium to condense.

These steps collectively facilitated the conversion of a Ta layer into a $TaSe_2$ shell, resulting in core/shell $ZnS/Al_2O_3/TaSe_2$ NWs. The phase composition of selenized ZnS/Al_2O_3/Ta nanowires (NWs) on oxidized Si/SiO_2 substrates was analysed using X-ray diffraction (XRD) and the Rietveld refinement method *(fig. 3.7)*. The results confirmed the successful selenization of the Ta coating, indicated by the characteristic 4Hb-$TaSe_2$ peak (004). Similarly, Ta layer was deposited on a flat substrate (silicon) which also showed successful selenization of the deposited Ta thin film to $TaSe_2$. Additionally, the presence of the wurtzite ZnS phase for the NWs' core was identified, indicating that the selenization process did not affect the ZnS core. No peaks corresponding to ZnSe were detected, suggesting that the ZnS NW core did not undergo selenization. However, a β-Ta_2O_5 peak was observed, potentially due to oxidation of the Ta coating when exposed to air, followed by crystallization during high-temperature processing in the ampoule [170–172]. Despite this, no peaks for Al_2O_3 were detected, likely because the ALD coating was amorphous and had a high crystallization temperature. Additional Bragg peaks found in the XRD patterns were attributed to the Si(100) substrate and the gold nanoparticles used in the vapor–liquid–solid growth process. The Rietveld analysis employed crystallographic data for 4Hb-$TaSe_2$, Zn, Ta_2O_5, and Au, confirming the phase composition and structural integrity of the fabricated $ZnS/Al_2O_3/TaSe_2$ NWs.

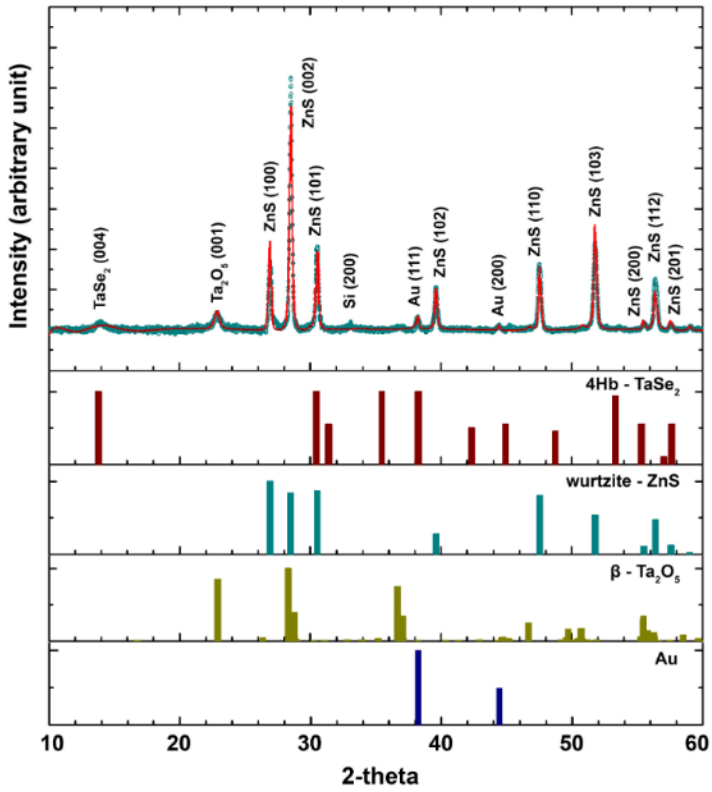

Figure 3.7: Rietveld refinement (solid line) of the X-ray diffraction pattern (open circles) for selenized ZnS/Al_2O_3/Ta NWs on an oxidized Si/SiO_2 substrate. The corresponding Bragg indexes for each crystalline phase have been identified and marked, as well as XRD patterns for 4Hb-$TaSe_2$, wurtzite ZnS phase, β-Ta_2O_5 and Au.

X-ray Photoelectron Spectroscopy analysis was used to further validate the chemical states within the shell of the hetero-structured nanowires *(fig. 3.8)*. The high-resolution spectra for Ta 4f and Se 3d peaks were acquired, calibrated relative to the adventitious C 1s peak at 284.8 eV. The XPS analysis did not detect any additional elements, confirming the presence of tantalum selenide in the shell and carbon from the substrate's surface. The Ta 4f scan displayed two doublets, with a spin-orbit splitting of 1.91 eV between the Ta $4f_{7/2}$ and $4f_{5/2}$ components in each doublet, and an area ratio held at 4:3. The first doublet, with a Ta $4f_{7/2}$ peak at 25.2 eV, indicated a valence state of 4+ in the $TaSe_2$ compound [171]. The second doublet, with a Ta $4f_{7/2}$ peak shifted to 27.0 eV, was associated with the Ta_2O_5 compound, reflecting a valence state of 5+. The detection of this β-Ta_2O_5 phase aligned with earlier XRD measurements. Due to the susceptibility of $TaSe_2$ to oxidation, particularly in its nanostructured form, care must be taken to handle and store the material in oxygen-free environments to prevent degradation. The Se $3d_{5/2}$ peak, located at 55.6 eV with a spin-orbit splitting of 0.86 eV, confirmed the presence of tantalum selenide in the core-shell

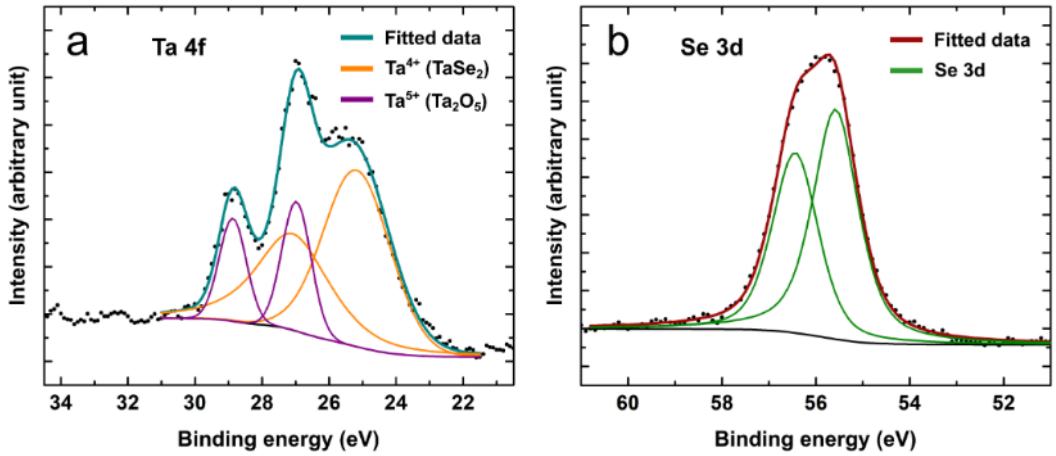

Figure 3.8: High-resolution XPS spectra of the selenized ZnS/Al_2O_3/Ta NWs elements for (a) Ta and (b) Se. Ta 4f peak scan fitting revealed two chemical states (Ta 4+ and 5+) present in the sample.

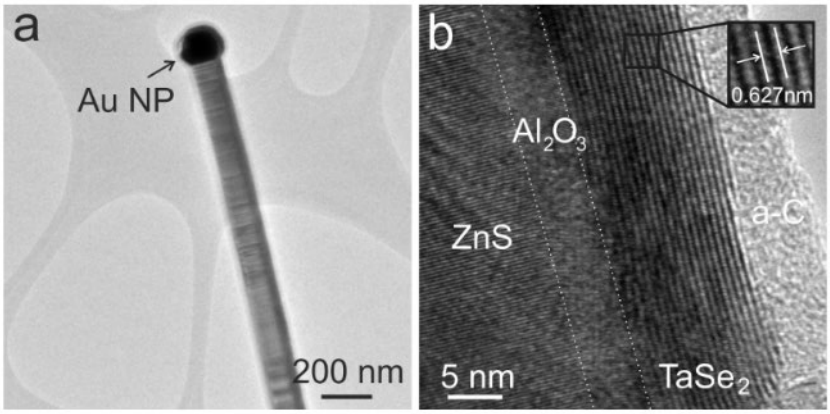

Figure 3.9: TEM images of ZnS/Al_2O_3/$TaSe_2$ NWs at different magnifications. A single ZnS/Al_2O_3/$TaSe_2$ NW with a Au NP at the end on a Lacey carbon-coated TEM grid (a). ZnS/Al_2O_3/$TaSe_2$ NW at high magnification; the individual layers of the heterostructure are identified, and amorphous carbon (a-C) is also present on top of the $TaSe_2$ shell (b).

NWs. This comprehensive analysis validates the chemical composition of the fabricated heterostructures and underscores the need for controlled storage to maintain stability.

Transmission Electron Microscopy (TEM) was used to examine the morphology and internal structure of core/shell nanowires (NWs). Typical images revealed that each NW's ends contained gold nanoparticles, a hallmark of the vapor–liquid–solid (VLS) growth mechanism. In the TEM images, these Au nanoparticles appeared as black dots, indicating the use of Au NPs in the synthesis process *(fig. 3.9)*. Following the selenization of the tantalum shell, a layer of $TaSe_2$ was observed surrounding the NWs, visible as parallel black lines. The shell thickness ranged from about 10 to 20 layers, with an interlayer distance of approximately 0.627 nm, closely matching the interlayer distances found in various $TaSe_2$ phases, including 1T, 2H, and 4Hb structures [173]. A non-crystalline carbon layer was also discovered on top of the $TaSe_2$ surface, likely due to carbon in the ambient atmosphere catalysed during the selenization process. Although atomic resolution of the Al_2O_3 interlayer, which separates the ZnS NWs from the $TaSe_2$ shell, could not be achieved, the observed amorphous spacing thickness aligned with the expected Al_2O_3 thickness. In an additional experiment with ZnO/Al_2O_3/Ta NWs, the ZnO NWs core completely sublimated during the selenization process, but the Al_2O3 shell remained intact, and the $TaSe_2$ layer formed successfully, suggesting potential for creating hollow-core tube-like Al_2O3/$TaSe_2$ heterostructures.

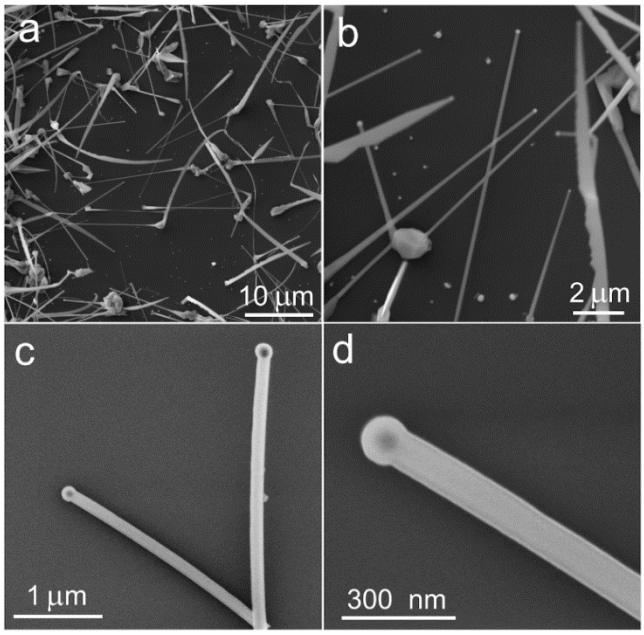

Figure 3.10: SEM images of selenized ZnS/ Al_2O_3/Ta NWs grown on Si/SiO_2 substrate at different magnifications taken at 12 keV (a,b) and 5 keV (c,d), respectively.

Using this technique, the metallic Ta layer was completely transformed into a well-defined $TaSe_2$ shell surrounding the ZnS/Al_2O_3 nanowires. Characterization of the synthesized core/shell ZnS/Al_2O_3/$TaSe_2$ NWs with X-ray diffraction, X-ray photoelectron spectroscopy, transmission electron microscopy, and scanning electron microscopy *(fig. 3.10)* confirmed that the core/shell structure formed as intended, while the integrity of the NWs was maintained throughout the selenization process.

3.3 Key results and Implications

3.3.1 GaN-MoS_2 and GaN-WS_2 Core–Shell NWs

- **Methodology**:

  Two methods demonstrated for growing GaN-MoS_2 and GaN-WS_2 core–shell NWs:

  1. Two-step process of sputter-deposition of a sacrificial transition metal oxide coating on GaN NWs followed by sulfurization with chemical vapor transport

  2. Pulsed laser deposition of few-layer MoS_2 or WS_2 on GaN NWs from the respective material targets

- **Material Characterization**:

  Characterization techniques used include scanning electron microscopy, transmission electron microscopy, X-ray diffraction, micro-Raman spectroscopy, and X-ray photoelectron spectroscopy.

- **Surface Morphology:**

  Process parameters could be adjusted to achieve either smooth and uniform shell around NWs or non-uniform, island-like coating with increased surface roughness.

- **Material Composition:**

  GaN NWs were identified as an ideal substrate for MoS_2 and WS_2 growth due to matching crystal lattice and high chemical stability in sulphur atmosphere

- **Potential Applications:**

  Density Functional Theory (DFT) calculations suggested potential use of GaN-MoS_2 and GaN-WS_2 core–shell NWs as photocatalysts for efficient hydrogen production from water.

3.3.2 Core/Shell NWs with $TaSe_2$ Shell by Selenizing Ta Film

- **Methodology**:

  Four-step synthesis routine for fabricating core/shell NWs with a 2D transition metal dichalcogenide (TMD) shell by selenizing a thin film of tantalum:

  I. synthesis of ZnS NWs,
  II. deposition of an Al_2O_3 layer by atomic layer deposition (ALD),
  III. magnetron sputtering of a Ta layer, and
  IV. annealing in selenium atmosphere.

- **Material Characterization**:

  Characterization techniques used include scanning electron microscopy, transmission electron microscopy, X-ray diffraction, and X-ray photoelectron spectroscopy.

- **Material Composition:**

Achieved complete transformation of metallic Ta layer into well-defined $TaSe_2$ shell around ZnS/Al_2O_3 NWs.

- **Potential Applications:**

  Unique properties of 2D materials and the presented method open avenues for future research and development in nanostructures, with potential breakthroughs in energy harvesting, sensing, and nanodevice fabrication.

3.3.3 Unique and novel aspects

- **GaN-MoS_2 and GaN-WS_2 heterostructures:** In other research work, these concepts were explored but in a planer form of these materials [165,167,168]. Here we offer an alternative form of these heterostructures in a form of core-shell nanowires. As these materials have shown potential for HER applications, increased surface area formed by our proposed methodology could improve its reactivity. In addition to that, we show comparison of two approaches (one is direct deposition of the TMD materials with PLD and other is by combining magnetron sputtering and CVT) and their pros and cons.
- **ZnS-Al_2O_3-$TaSe_2$ heterostructures:** Material of $TaSe_2$ has been shown to have potential as catalyst for HER application but using exfoliated crystals [174]. With our approach we have synthesized $TaSe_2$ material as a shell on a nanowire from Ta metal deposited via magnetron sputtering, which increases the surface area of this catalyst material as well as makes it possible for a scalable production of such materials. One thing to note here is also we avoided the use of Ta_2O_5 as precursor as it has high thermal stability which proves challenges when trying to convert it into its chalcogenide form. Another unique aspect of this study is the use of ZnS as the core of nanowire, where we have sulphur as the chalcogen atom and in shell material we have selenium as chalcogen atom. These two materials were protected or separated from each other using Al_2O_3 deposited by ALD. This also highlights the various use cases for how different TMDs heterostructures can be created without harming the structural integrity of each and harness the full potential of that heterostructure.

4. Growth of TMDs thin films

4.1 WSe_2 thin films and crystals

WSe_2 Thin Films: This work investigated the synthesis of tungsten diselenide (WSe_2) thin films via chemical vapor transport (CVT) employing two distinct sacrificial precursor films: tungsten trioxide (WO_3) and metallic tungsten (W). The primary objective was to comparatively analyse the resulting WSe_2 films and correlate their properties to the precursor material. Given the scalability and efficiency of the CVT method, it was selected for this study to facilitate potential future upscaling.

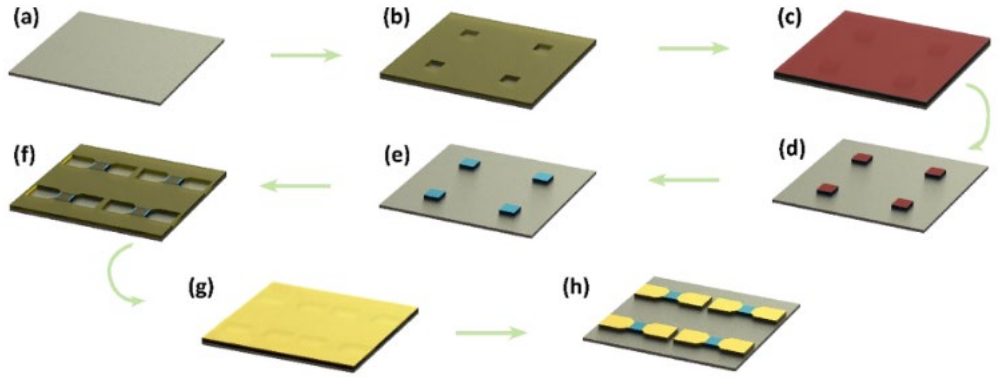

Figure 4.1: Schematic of the process of on-chip device fabrication. First the SiO_2/Si substrate is cleaned using acetone and isopropanol (a), then the first mask is made using the standard photolithography process (b) on which precursor material is deposited (c). After first mask lift-off, the precursor material film is in the desired pattern (d) which is subsequently selenized (e). Afterwards, the second photoresist mask is deposited (f) for the deposition of contact material (Cr ~ 5 nm, Ag ~ 95nm, Al ~ 50 nm) using the thermal evaporation method (g) followed by lift-off to obtain the photoconductor device array on a chip (h).

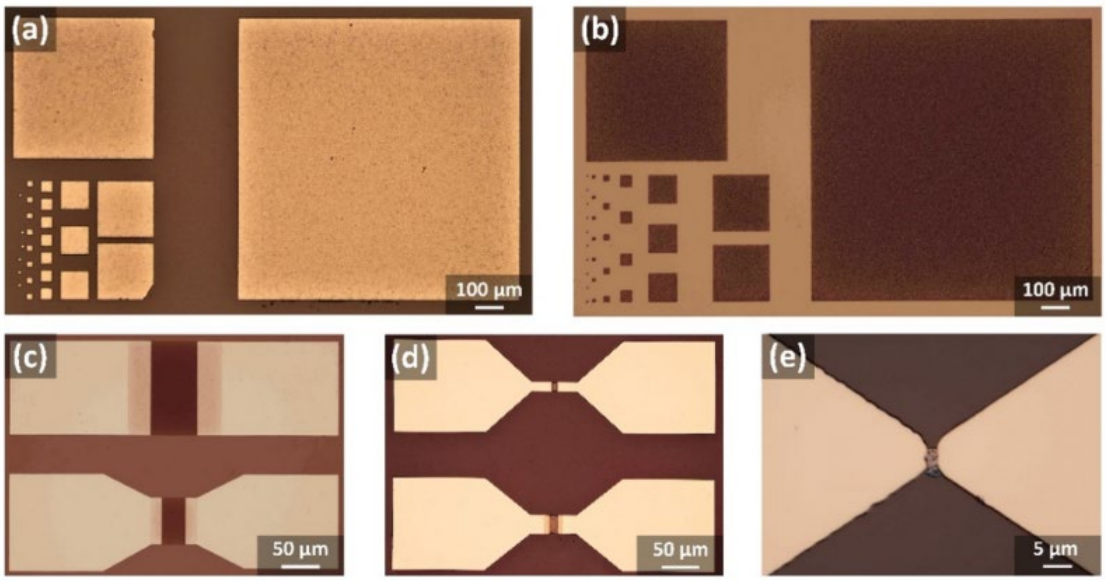

Figure 4.2: Optical images of the synthesized patterned WSe_2 films made by photolithography (a,b), and devices with various gap widths between the two electrodes were fabricated (c–e) using WSe_2 films.

To demonstrate the photoelectric properties of the synthesized WSe_2 films, on-chip device fabrication and characterization were performed *(fig. 4.1)*. The synthesis of WSe_2 thin films was conducted using the chemical vapor transport method, employing two different sources of magnetron sputtered sacrificial precursor films: WO_3 and W metal.

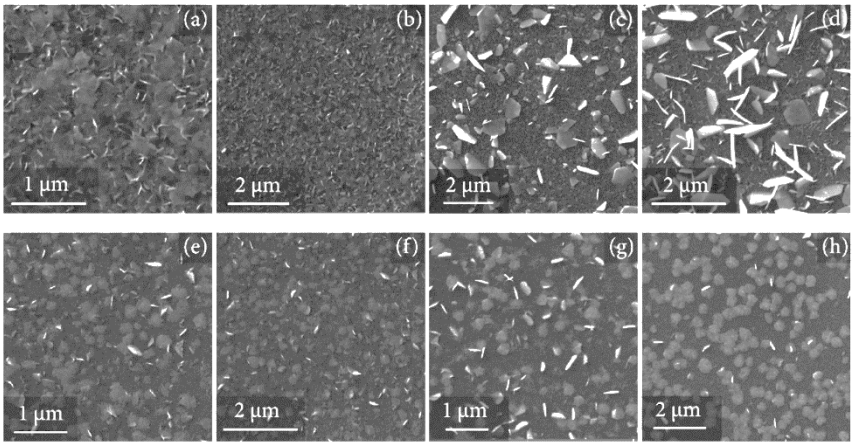

Figure 4.3: Scanning electron microscope images at different magnifications of WSe_2 films made from a WO_3 precursor at 700°C (a,b) and 800°C (c,d) and from a W metal precursor at 700°C (e,f) and 800°C (g,h)

After experimenting with various thicknesses of the deposited precursor materials, WO_3 and W, ranging from 3 nm to 40 nm, thicknesses of near 30 nm were chosen for both precursors for this study. WSe_2 films using chemical vapor transport. Here are some optical images of the synthesized films with patterns created using standard photolithography *(fig. 4.2)*. SEM analysis *(fig. 4.3)* revealed that films from WO_3 typically had larger crystals, reaching up to 1 µm at higher temperatures (800 °C). Below 700 °C, WSe_2 crystals did not form, while above 800 °C, films began to sublimate. Films from the W metal precursor had smaller, more consistent crystals with clear boundaries, with diameters of 0.5 µm regardless of temperature. The smaller crystal size from W metal contrasted with WO_3-based films, which had greater variability in crystal size, from 0.2 to 1.5 µm. The larger out-of-plane crystal growth in WO3-based films is likely due to higher volatility and diffusivity during selenization.

AFM Z-drive images *(fig. 4.4)* further supported these observations, with films from WO_3 showing more random crystal growth, while those from W metal had flatter surfaces with more uniform crystal distribution. The out-of-plane crystal growth in WO_3-based films could be due to vapor-phase selenization and re-deposition of WSe_2.

The crystalline phase composition of WSe_2 films grown on $Si(100)/SiO_2$ substrates was investigated through X-ray diffraction analysis. XRD patterns obtained from films synthesized from WO_3 and W metal precursors at 700 °C and 800 °C are presented in *(fig. 4.5)*. All diffraction patterns exhibit characteristic peaks corresponding to crystalline WSe_2 (ICDD-PDF #38-1388), indicating the successful formation of the desired phase. No extraneous peaks attributable to secondary phases or impurities were detected. The prominent

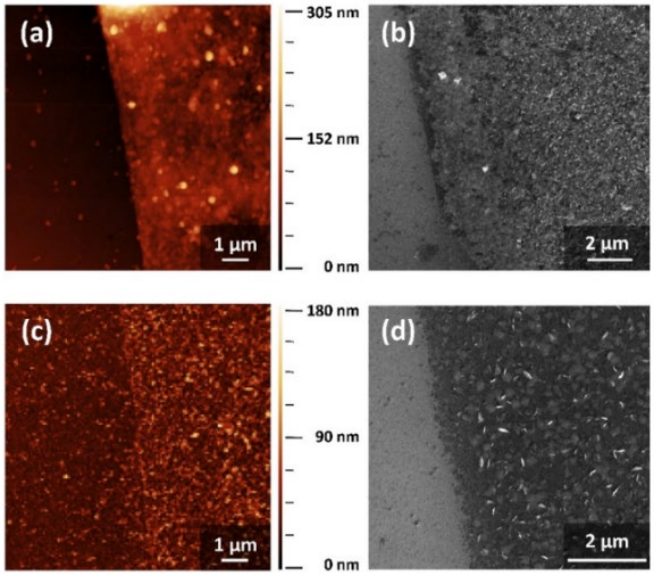

Figure 4.4: Atomic force microscope (AFM) Z-drive images of WSe_2 films made from a WO_3 precursor (a) and from a W metal precursor (c) showing the difference between film surfaces and further complimented by SEM images of the same samples in the respective order of (b) and (d)

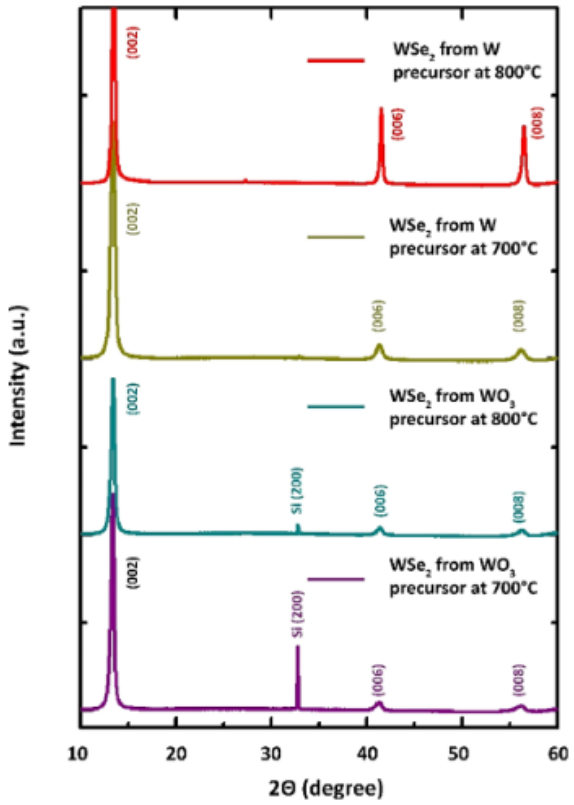

Figure 4.5: X-ray diffraction patterns of WSe_2 films from both precursors (WO_3 and W) at different temperatures, 700°C and 800°C, show peaks confirming the phase of the synthesized WSe_2 film

peak observed at approximately 33° is ascribed to the Si(100) substrate. To further corroborate the XRD findings, micro-Raman spectroscopy was performed on the synthesized films at ambient temperature *(fig. 4.6).* The presence of distinct Raman peaks cantered around 250.2 cm^{-1} and 259 cm^{-1} unequivocally confirms the formation of WSe_2, corresponding to the in-plane (E^1_{2g}) and out-of-plane (A^1_g) vibrational modes, respectively [175,176]. The combined XRD and Raman analyses conclusively demonstrate the effective conversion of both WO_3 and W precursors into crystalline WSe_2 thin films via the chemical vapor transport (CVT) process. These results establish the reliability and efficacy of the CVT method for producing high-quality WSe_2 films.

Figure 4.7(a-c) illustrate the photoelectric characteristics of WSe_2 films synthesized from WO_3, while figure 4.7(d–f) show those synthesized from the W metal precursor. Both sets of films exhibit linear current–voltage (I–V) behaviour in the dark, suggesting the formation of Ohmic contacts. The devices were tested under a 405 nm wavelength light source to study their photo-response. The on-off measurements revealed a rapid and repeatable change in current (rise and fall times below 20 ms), indicating good device reversibility when the light source is switched on and off. However, WSe_2 films synthesized from the W metal precursor displayed unstable photocurrent, with transient spikes upon light exposure that quickly returned to dark current levels. This behaviour is attributed to charge trapping/de-trapping at the semiconductor/electrode interfaces and space-charge effects. Additionally, WSe_2's susceptibility to defects, like selenium vacancies, can degrade photoelectric properties. Films made from the WO_3 precursor demonstrated better photoelectric performance compared to those from W metal. The improved performance could be due to oxygen impurities introduced during the formation of WSe_2 from WO_3,

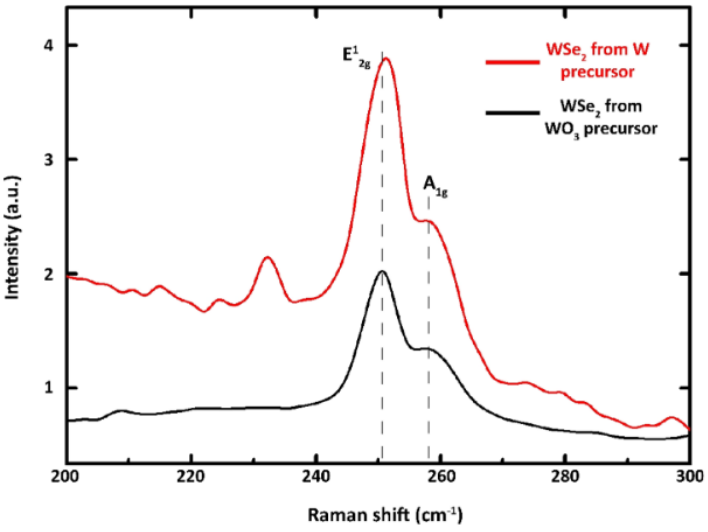

Figure 4.6: Raman spectra of WSe_2 thin films synthesized from both precursors (WO_3 and W) using CVT method showing the peaks respective to E^1_{2g} and A^1_g vibrational modes

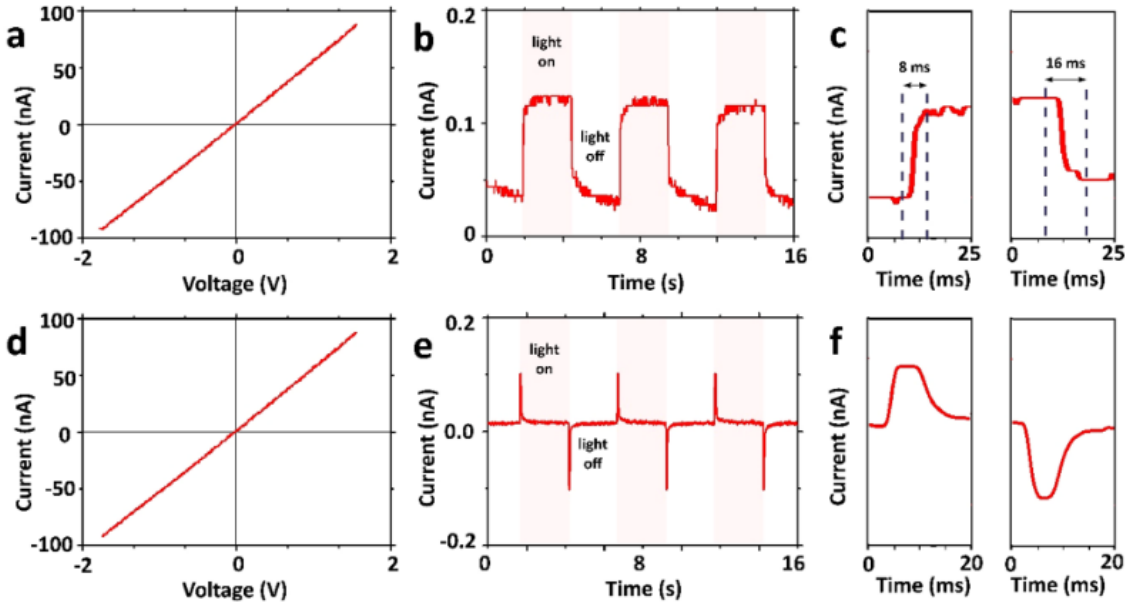

Figure 4.7: WSe_2 two-terminal photoconductor devices prepared from WO_3 and W metal as the precursor materials, respectively, showing dark state I–V characteristics (a,d), on–off response (b,e), and response time (c,f) measurements at 2 V bias voltage and 1 W/cm² light intensity with a 405 nm wavelength light source.

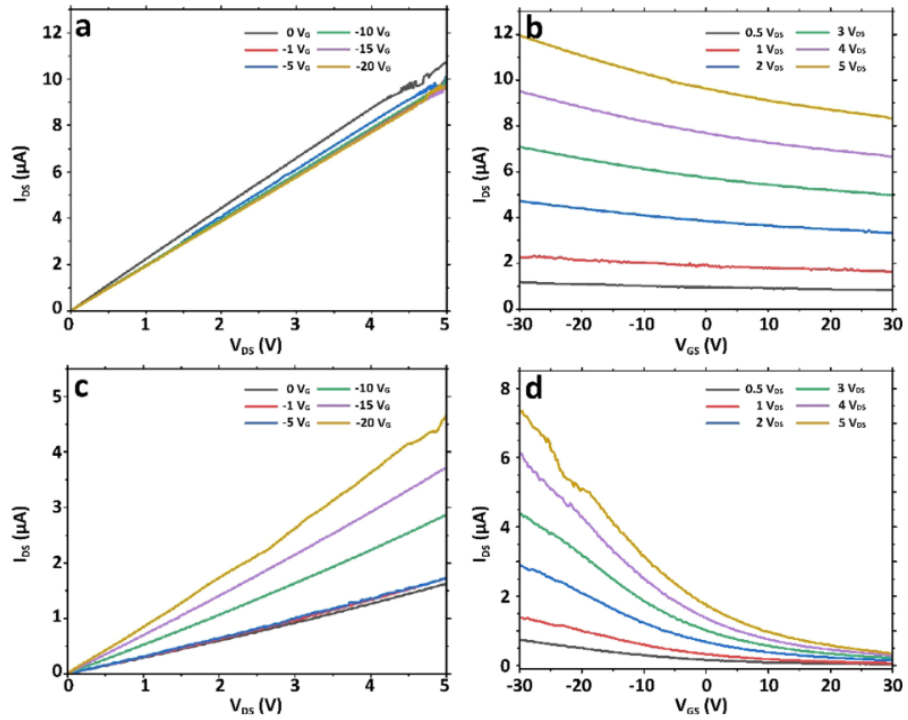

Figure 4.8: WSe_2 two-terminal photoconductor devices, prepared from W(a,b) and WO_3(c,d) metal as the precursor (I_{DS}-drain source current, V_{DS}-drain source bias voltage, V_{GS}- gate source bias voltage).

which might help passivate selenium vacancies. Oxygen passivation of these defects has been shown to enhance photodetector performance. In contrast, W metal-based films lack oxygen atoms for such

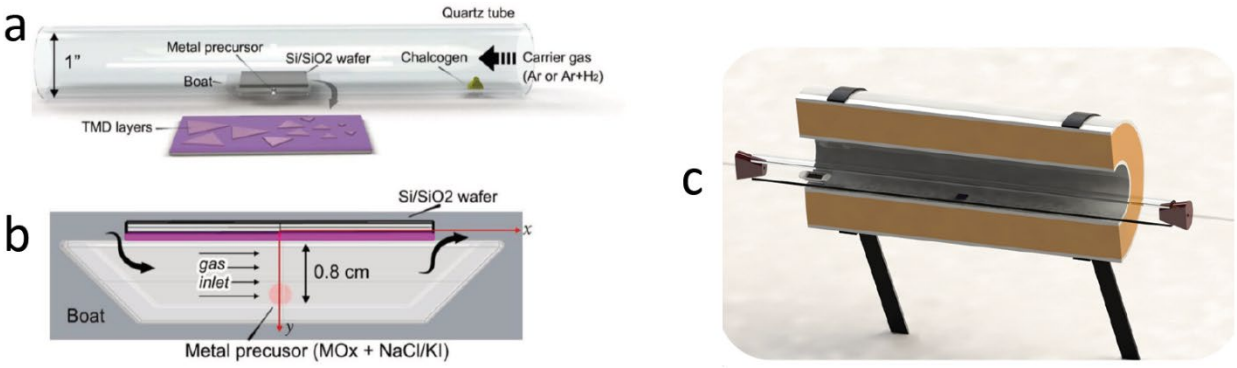

Figure 4.9: WSe_2 crystal synthesis setup (c) used for the synthesis of crystals. Image a,b are crucial parameters shown by Zhou et al. which this setup was configured for [186].

passivation, resulting in degraded photoelectric properties. Field effect transistors (FETs) were fabricated to conduct electrical characterization of the WSe_2 films *(fig. 4.8)*. The output and transfer curves were measured to assess the electrical properties. The output curve for WSe_2 films synthesized from W metal precursors showed minimal response to gate bias potential, indicating incomplete conversion from W metal to WSe_2. This suggests that the residual metal phase could be acting as a shunt resistance, affecting the semiconducting layers. In contrast, FETs made from WSe_2 films derived from the WO_3 precursor exhibited a stronger field-effect and clear p-type conductivity. The output curves displayed nonlinear behaviour at high gate voltages, potentially due to a small Schottky barrier at the metal/semiconductor junction, which could be caused by differences in work function between chromium and WSe_2. The transfer curves revealed that reducing the gate-source voltage from +30 V to -30 V resulted in a 95.9% increase in source-drain current at 5 V source-drain voltage, compared to only a 31.6% increase for films made from W metal precursors. These findings suggest that WSe_2 synthesized from WO_3 precursors has superior electrical properties compared to those made from W metal, highlighting the effectiveness of the chemical vapor transport (CVT) method with WO_3 in producing higher-quality WSe_2 films.

WSe_2 crystals: In addition to the thin film synthesis, using salt assisted CVT process WSe_2 crystals were also synthesized from NaCl and WO_3 mixture with weight ratio of 5:1. The setup used for that is shown here in *(fig. 4.9)*. The furnace used in this setup was movable and only after it reaching its targated temperature of 800C it was moved onto the area of horizontal quartz tube where selenium powder, samples and carmaic boat containing the NaCl-WO_3 mixture were placed beforehand with gas flow of 5% H_2/Ar. The heated furnace was moved in the position where centre part of it would be over the samples and it was kept threr only for a short period of time (150-180 seconds) and after that the furnace was switched off and moved away from the selenium powder source to begin colling down of the system. If the furnace was moved too quickly, droplets of selenium were noticed on the samples, and to avoid that, usually after beginning of the cooling down period, furnace kept at its newly move position for next 5 minutes. After which it was moved again completely away from the samples and waited for the samples to cool down completely to room temperature, and later taken out for analysis.

Optical microscopy is used to capture images *(fig. 4.10)* of the synthesized WSe_2 crystals on the Si/SiO_2 substrate. Here it is important to note that, taking SEM images was avoided due to its potential harmful effects on the crystals. These optical images reveal the morphology and distribution of the WSe_2 crystals. The crystals appear as well-defined, layered structures with varying shapes and sizes, indicating successful deposition on the substrate. Characterization techniques such as X-ray diffraction (XRD) and Raman spectroscopy are employed to analyze the structural and compositional

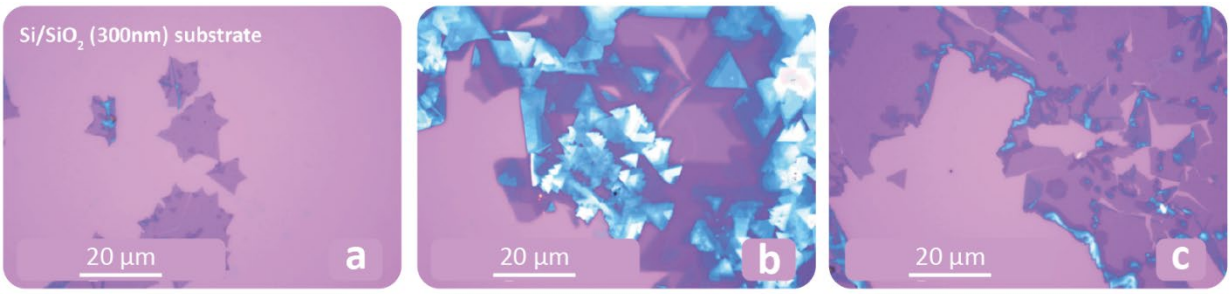

Figure 4.10: Optical images of the synthesized WSe_2 crystals on different samples.

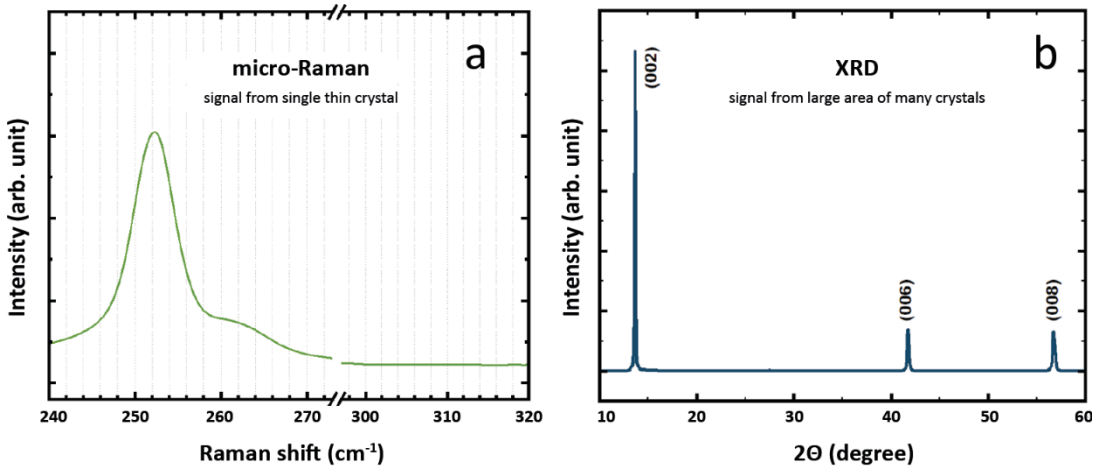

Figure 4.11: (left)Raman and (right) XRD of the synthesized WSe_2 crystals of different samples. For Raman, the signal was obtained by focusing laser on an atomically thin crystal whereas XRD data was obtained through large area scan over the whole substrate.

properties of the WSe_2 crystals. The XRD pattern *(fig. 4.11)* confirms the crystalline nature of the WSe_2, showing distinct peaks corresponding to the hexagonal lattice structure. Raman spectroscopy provides further confirmation of the material, with characteristic peaks indicative of WSe_2 [176,177].

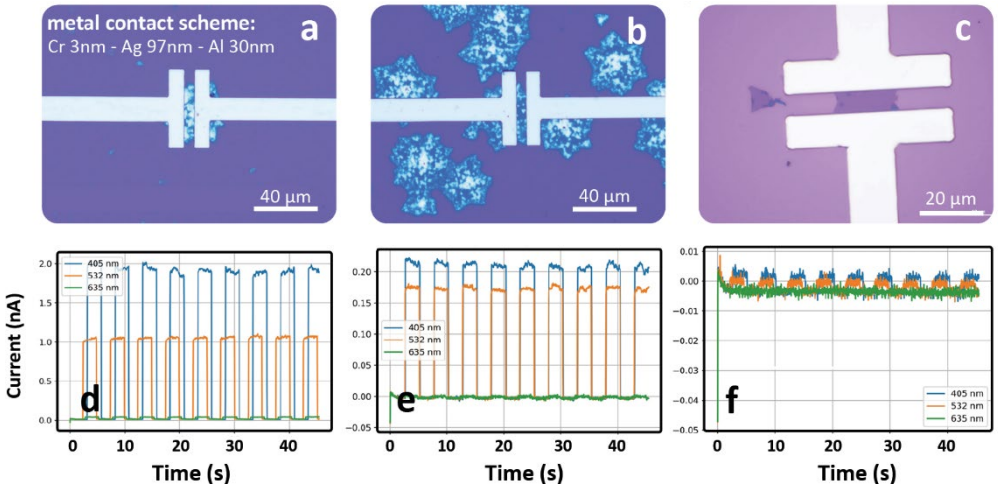

Figure 4.12: (a-c) Optical images of the devices made and (d-f) photo measurements. 1V bias applied for all measurements

For device fabrication, a metal contact scheme comprising layers of chromium (3 nm), silver (97 nm), and aluminum (30 nm) was employed. Optical images of the devices showed the layout and contact points *(fig. 4.12)*. The photoresponse of these devices was measured under different illumination conditions, demonstrating sensitivity to light. Photocurrent response graphs under 405 nm, 532 nm, and 635 nm light intensities were provided, highlighting the potential of these devices in optoelectronic applications.

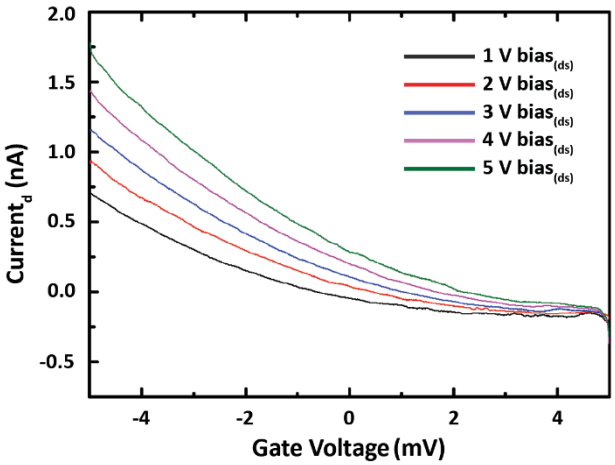

Figure 4.13: FET measurements performed on 2D crystals to show its p-type of conductivity of these crystals.

Field-effect measurements on WSe_2-based transistors evaluated their performance, with transfer characteristics plotted *(fig. 4.13)* to show the relationship between drain current (I_d) and gate voltage (V_g) for different drain-source voltages (V_{ds}). These measurements offered insights into the electronic properties of WSe_2 crystals, emphasizing their suitability for field-effect transistors (FETs). The analysis of the synthesis process, structural characterization, and device performance illustrates the significant potential of WSe_2 crystals in advancing optoelectronic and electronic applications..

4.2 $ReSe_2$ thin films

To find the optimal conditions for producing high-quality $ReSe_2$ thin films in the framework of this study, investigation of different precursors (metallic rhenium Re and rhenium oxide ReO_x) as well as two substrates: SiO_2/Si (100) from Semi-conductor Wafer, Inc. and sapphire (c-plane) from Biotain Crystal Co. was carried out. A two-step approach was employed, starting with the deposition of thin rhenium (Re) and rhenium oxide (ReO_x) films with thicknesses ranging between ~10-70 nm on both substrates of ~100 mm^2 square size using magnetron sputtering *(fig. 4.14)*. These precursor films served as the foundation for the subsequent conversion to $ReSe_2$ via chemical vapor transport (CVT).

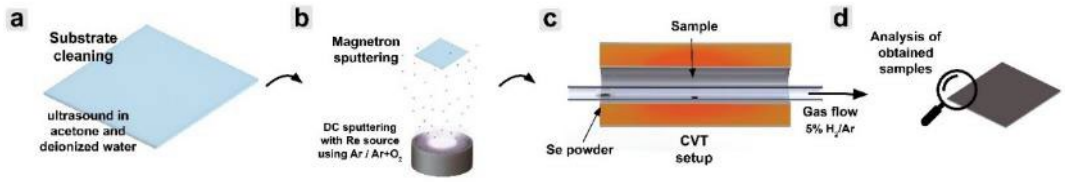

Figure 4.14: Graphical illustration of the methodology followed in this work starting with (a) substrate preparation by cutting them in ~100 mm^2 square size and cleaning them in ultrasound, (b) magnetron sputtering of Re and ReO_x precursor films, (c) selenization process at elevated temperatures in horizontal quartz tube CVT setup for 15 minutes followed by (d) analysis of the synthesized material via various techniques.

To determine the optimal synthesis temperature for producing $ReSe_2$ thin films using an atmospheric pressure CVT setup, temperatures ranging from 550°C to 1000°C were investigated for both Re metal and ReO_x precursors. Initial XRD patterns *(fig. 4.15)* showed that at lower temperatures

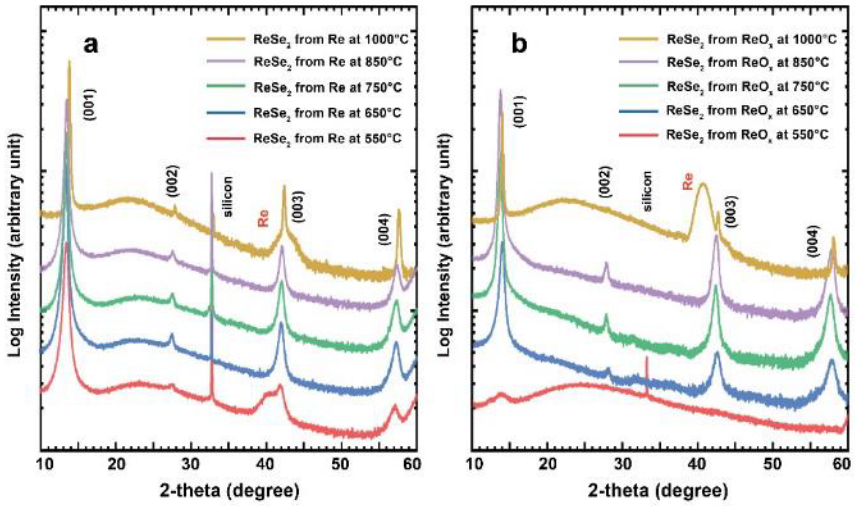

Figure 4.15: X-ray diffraction patterns for the synthesized $ReSe_2$ films from (a) Re metal precursor films and (b) ReO_x precursor films at 650°C, 750°C, 850°C and 1000°C on SiO_2/Si substrate for 15 minutes.

(550°C), the precursors did not fully react with selenium, while at higher temperatures (1000°C), reduction of $ReSe_2$ films was observed, likely due to the use of a 5% H_2/Ar carrier gas mixture. Notably, in this CVT process, the presence of H_2 in the carrier gas accelerates the reaction and selenization rate by producing highly reactive H_2Se gas. Additionally, H_2 helps limit the formation of undesired oxides during cooling.

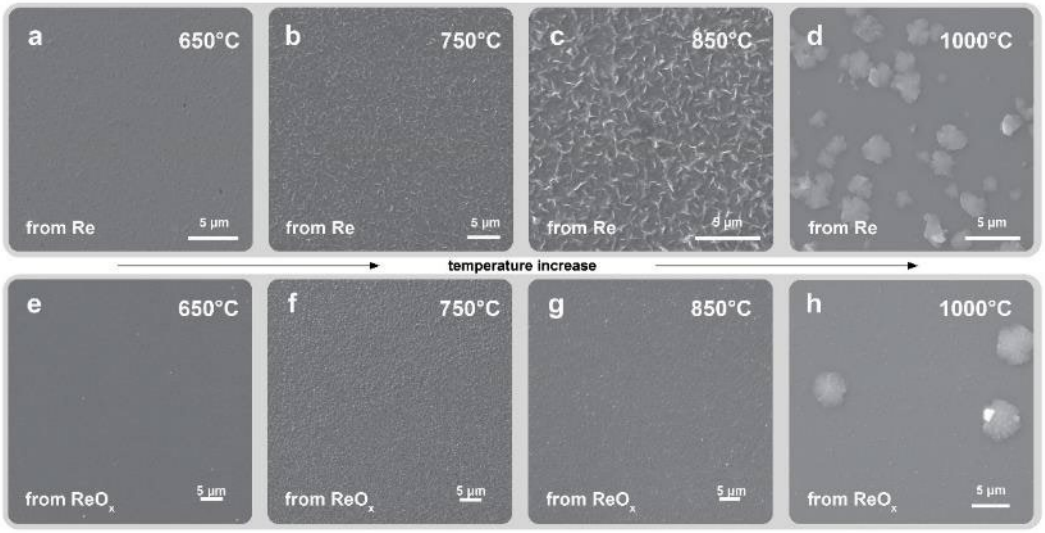

Figure 4.16: SEM images of the synthesized $ReSe_2$ films from (a-d) Re metal precursor films and (e-h) ReO_x precursor films using 650°C to 1000°C temperatures on silicon as substrate.

The obtained XRD patterns matched well with ICDD card no. 04-007-1113 and previous studies on this material, indicating the presence of highly crystalline films of $ReSe_2$ in a distorted 1T′ structure with triclinic symmetry (P$\bar{1}$) in the temperature range of 650°C to 850°C [51]. To further investigate

the selenization temperatures and their effects on the surface morphology of the $ReSe_2$ films, SEM images were taken *(fig. 4.16)*. Samples synthesized at lower temperatures were discarded as they showed partially converted precursor materials from the XRD analysis. SEM images revealed that with increasing temperature, surface roughness became more noticeable for both precursors. Specifically, films synthesized from Re metal precursors displayed an increase in out-of-plane filamentary structures as the temperature increased, and at the highest synthesis temperature tested (1000°C), both precursor materials exhibited surface crystal formation.

We hypothesize that the formation of out-of-plane filamentary structures in Re precursor-based films could be due to the high density of Re metal, which expands when selenized, adding two Se

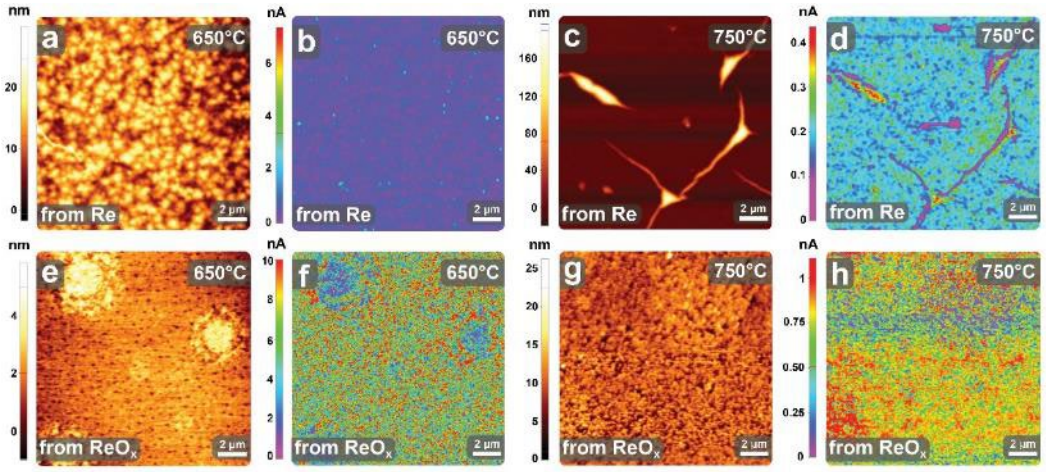

Figure 4.17: AFM images of the synthesized $ReSe_2$ films on sapphire substrate from (a-d) Re metal precursor and (e-h) ReO_x precursor at 650°C and 750°C temperatures are shown here. Fig. a, c, e, g are topographical images and fig. b, d, f, h are of conductive AFM measurements with platinum tip and 0.02V bias. All images were taken in 255 µm² area.

atoms per Re atom. If expansion is restricted due to interlayer forces, these out-of-plane features develop to relieve the stress. This behaviour becomes more pronounced with increasing selenization temperature, resulting in higher density and elevations of these features compared to lower temperature conversions. Based on these initial findings, synthesis temperatures were narrowed down to two optimal points: 650°C and 750°C, to further study the effects of temperature variation on the properties of the synthesized films. For AFM and optical measurements, sapphire substrates were used to synthesize the $ReSe_2$ films, with no impact on the growth process observed as XRD and SEM analyses showed identical results on both substrates under the same synthesis parameters.

AFM results revealed a highly conductive, fine-grained surface with crystallite sizes ranging from 50 to 100 nm, varying with the sample *(fig. 4.17)*. AFM topography results for $ReSe_2$ films synthesized at 650°C and 750°C from Re and ReO_x precursors showed notable differences. At 650°C, Re-derived films exhibited significant roughness, whereas ReOx-derived films had a more uniform and smoother texture. At 750°C, Re-derived films displayed pronounced out-of-plane filamentary structures, indicating substantial changes in surface morphology, while ReO_x-derived films remained relatively smooth with slightly increased roughness compared to lower temperatures. Conductivity mapping further highlighted the differences in the films' electronic properties. At 650°C, c-AFM mapping for Re-derived films showed varied conductivity distribution, corresponding to the rough surface morphology. In contrast, ReO_x-derived films had a more homogeneous conductivity map, reflecting their smoother surface. At 750°C, Re-derived films continued to show significant conductivity variations due to complex surface features, while ReO_x-derived films maintained a more uniform conductivity distribution, consistent with their relatively smoother surface.

XPS analysis was employed to determine the chemical states of elements in $ReSe_2$ films synthesized from both metal and oxide precursors at 650°C. The XPS spectra *(fig. 4.18, a-d)* revealed the presence of only Re and Se elements, along with organic surface contaminants like carbon and oxygen. High-resolution spectra of Re 4f and Se 3d peaks were calibrated against the adventitious C 1s peak at 284.8 eV. Both precursor types yielded identical XPS spectra. The Re 4f scan showed a peak with a single doublet, with a spin-orbit splitting $\Delta_{7/2-5/2}$ of 2.43 eV fixed between the Re $4f_{7/2}$ and $4f_{5/2}$

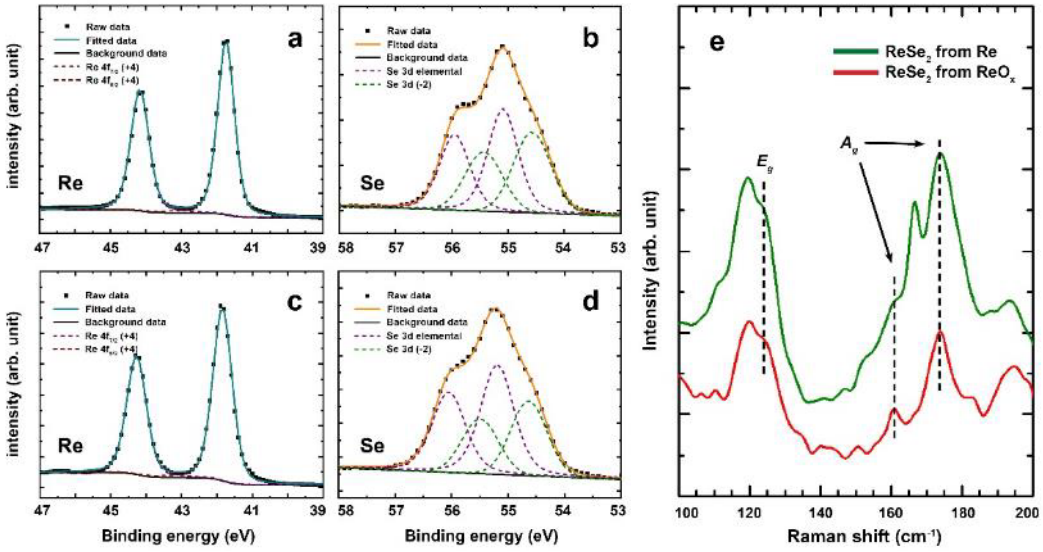

Figure 4.18: XPS spectra of $ReSe_2$ films synthesized at 650°C from (a,b) Re precursor films and (c,d) ReO_x precursor films. (e) Raman spectra of the $ReSe_2$ films synthesized at 650°C measured with 532 nm wavelength laser.

components, and an area ratio of 4:3. The Re $4f_{7/2}$ peak was located at approximately 41.8 eV, indicating a valence state of 4+ in the $ReSe_2$ compound [50,178]. The Se 3d peak displayed two doublets (spin-orbit splitting $\Delta_{5/2-3/2}$ = 0.86 eV, area ratio 0.735), with the first doublet at 54.7 eV corresponding to the 2- chemical state in $ReSe_2$, and the second doublet at 55.2 eV suggesting the presence of elemental Se on the selenide surface.

Raman spectroscopy further verified the composition and structure of $ReSe_2$ films synthesized at 650°C. The Raman spectra*(fig. 4.18, e)* revealed distinct vibrational modes corresponding to the Eg and Ag modes of $ReSe_2$, aligning well with previous studies. These Eg and Ag modes are characteristic of the in-plane and out-of-plane vibrations of Re and Se atoms in the $ReSe_2$ crystal lattice. The

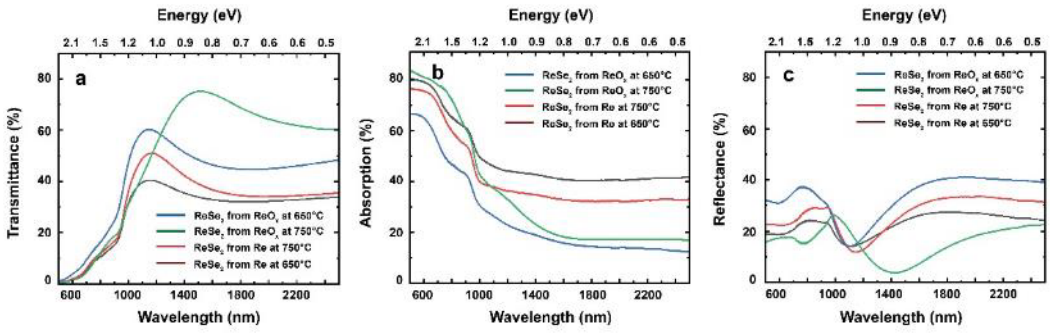

Figure 4.19: (a) Transmittance, (b) absorption and (c) reflectance of the produced $ReSe_2$ films on sapphire substrate from both precursor materials in the range of 500-2500 nm wavelength.

consistency of these Raman peaks with literature values confirms the successful formation of $ReSe_2$ with the expected crystalline structure and chemical composition [50,178].

Figure 4.19 shows the transmittance, absorbance, and specular reflectance of $ReSe_2$ films synthesized on c-plane sapphire, measured across the spectrum from 500 to 2500 nm. $ReSe_2$ films synthesized from ReO_x exhibit higher transparency in the infrared region, specifically within the range of approximately 1100 to 2500 nm *(fig. 4.19, a)*. This higher transmittance is attributed to

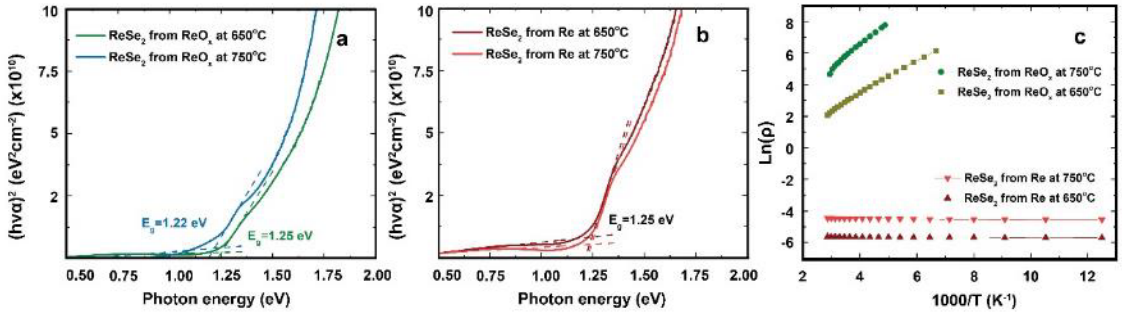

Figure 4.20: Tauc plot to deduce the direct optical bandgap of the $ReSe_2$ films synthesized from (a) ReO_x and (b) Re metal. (c) Change in Resistivity with temperature was measured using Van der Pauw configuration with a Hall effect system. Used samples for these measurements were covered with $ReSe_2$ films in 100 mm^2 square area.

significantly lower absorbance within this spectrum *(fig. 4.19, b)*. The optical properties correlate with temperature-dependent electrical resistivity measurements *(fig. 4.20, c)*, indicating that films produced from ReO_x are semiconductors, while those from Re exhibit higher conductivity and metallic behaviour. The pronounced absorbance is attributed to the higher concentration of charge carriers. Additionally, the selenization temperature influences the optical properties for both ReO_x and Re precursors, with a more pronounced effect in the case of ReO_x.

Figure 4.19(c) presents the corresponding specular reflectance of the films. Reflectance is influenced by factors like charge carrier concentration and surface roughness, making comprehensive interpretation challenging. However, more intense reflection observed at wavelengths >1200 nm in $ReSe_2$ films synthesized from ReO_x at 650°C compared to 750°C is related to smaller roughness, as confirmed by SEM and AFM analysis, which increases specular reflectance.

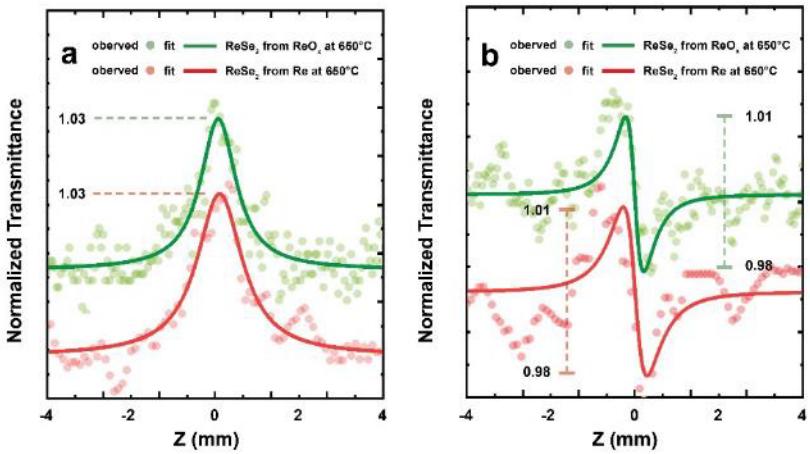

Figure 4.21: Open aperture Z-scan curves of the $ReSe_2$ thin films (a) synthesized from Re at 650°C and 750°C measured with the power of 16.4 W and 20.1 W respectively, (b) from ReO_x at 650°C and 750°C with the power of 21.2 W and 24.2 W with 900nm wavelength laser source.

All synthesized films exhibit a dark grey colour and high absorption (70–80%) in the visible light range *(fig. 4.19, b)*, due to the small direct optical band gap of approximately 1.2 eV determined from the Tauc plots *(fig. 4.20, a-b)*. These values are consistent with literature reports [179,180].

The Z-scan method was used to assess nonlinear optical properties *(fig. 4.21)*. The closed-aperture measurements were fitted using the standard Z-scan equation:

$$T_{OA} = 1 + \frac{4 \cdot \Delta\Phi \cdot \frac{z}{z_R}}{\left(\frac{z^2}{{z_R}^2} + 9\right)\left(\frac{z^2}{{z_R}^2} + 1\right)} \quad (1)$$

Where $\Delta\Phi = n_2 \cdot k \cdot I \cdot L_{eff}$ is induced phase change, n_2 is Kerr coefficient, k is wave number, I is optical intensity, $L_{eff} = (1-\exp(\alpha_0 \cdot L))/\alpha_0$ is effective length, α_0 is optical absorption, L is thickness, z is sample position and z_R is Rayleigh length. To calculate nonlinear absorption coefficient from Open-aperture data the fallowing expression was used:

$$T_{CA} = \sum_{n=0}^{\infty} \frac{\left(\beta \cdot I \cdot L_{eff}\right)^n}{\left(\frac{z^2}{{z_R}^2} + 1\right)^n (n+1)^{3/2}} \quad (2)$$

Where β is nonlinear absorption. In case of absorption saturation, this equation can only be used for low laser intensities ($I<I_S$) in which case $\beta = -\alpha_0/I_S$, where I_S is saturation intensity. A sample of Saphire substrate was used as reference measurement. The measured value was $n_2 = (2.16 \pm 0.42) \cdot 10^{-16}$ cm^2/W that corresponds to values demonstrated in literature. No nonlinear absorption effect was observed.

A Kerr signal was consistently observed for all samples of value $n_2 = (-1.23 \pm 0.65) \cdot 10^{-2}$ cm^2/W, exhibiting minimal variation depending on preparation procedure. Previous studies of $ReSe_2$/PVA thin films has presented Kerr values at 1560 nm ($n_2 = -2.81 \cdot 10^{-2}$ cm^2/W) and 1900 nm ($n_2 = -6.3 \cdot 10^{-2}$ cm^2/W). The current findings align with these previous studies and indicates that Kerr value decrease with wavelength in infra-red region [52,181].

Regarding saturation absorption the values for samples produced from Re was β=(-950±290) cm/GW and for sample produced from ReO_x was β=(-730±330) cm/GW. The SA coefficient has been demonstrated to exhibit a dependency on the layer number for $ReSe_2$, ranging from -4156 cm/GW for a single layer (0.71 nm) to -878 cm/GW for 42 layers (bulk sample; 29.81 nm) at 800 nm. Acquired values in this work align well with literature findings for bulk samples. For longer wavelengths, the SA value has been measured for $ReSe_2$/PVA thin films and increased to -5670 cm/GW at 1560 nm and -13800 cm/GW at 1900 nm, indicating an increase for SA values for longer wavelengths. The saturation absorption values of these samples indicate that they could be applicable for Q-switching or mode-locking in laser systems as 2D materials has been shown to play a key role for ultrafast laser systems. To implement these samples in practice either samples closer to few layers (thickness <7 nm as fewer layers lead to higher nonlinearities) or fabricating them in the form of $ReSe_2$/PVA structure should be considered.

4.3 $TiSe_2$ and VSe_2 thin films

The synthesis of $TiSe_2$ and VSe_2 involves a two-step process. Initially, metal precursor films are deposited using magnetron sputtering, followed by annealing in a Se vapor atmosphere within a sealed quartz ampoule. Utilizing magnetron sputtering for precursor film deposition enables

covering large surface areas, including the centimetre-scale substrates utilized in this study. This method could also be extended to non-flat surfaces, such as nanostructures, to augment their surface area and improve their properties for potential applications in catalysis, sensors, etc.

From our experiments, a 15 nm thickness of the metal precursor resulted in continuous diselenide

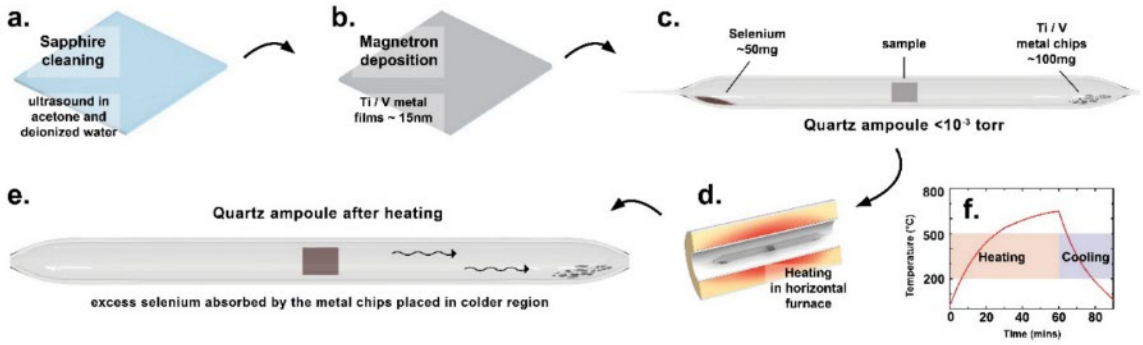

Figure 4.22: Graphical illustration of the methodology used here to synthesize $TiSe_2$ and VSe_2 thin films starting from (a) substrate cleaning in acetone and DIW using ultrasound for 5 mins each, followed by (b) deposition of Ti / V metal film using magnetron sputtering (c) sample placed in a quartz ampoule with Se powder and respective metal chips in shown configuration (d) ampoules heated up using a horizontal furnace (e) after heating the ampoule, no excess selenium vapour were found near edges of any ampoules. (f) heating cycle of an ampoule, shown with ramp rate of heating and cooling.

films after the selenization process, so this thickness was kept constant for all samples for this study. Initially, when ampoules were made without their respective metal chips (Ti/V), excess selenium vapor condensed near the edges of the samples or formed droplets on top of the synthesized material *(fig. 4.22)*. To resolve this, extra metal chips were introduced after several trials, which eliminated the excess Se issues and yielded the best results.

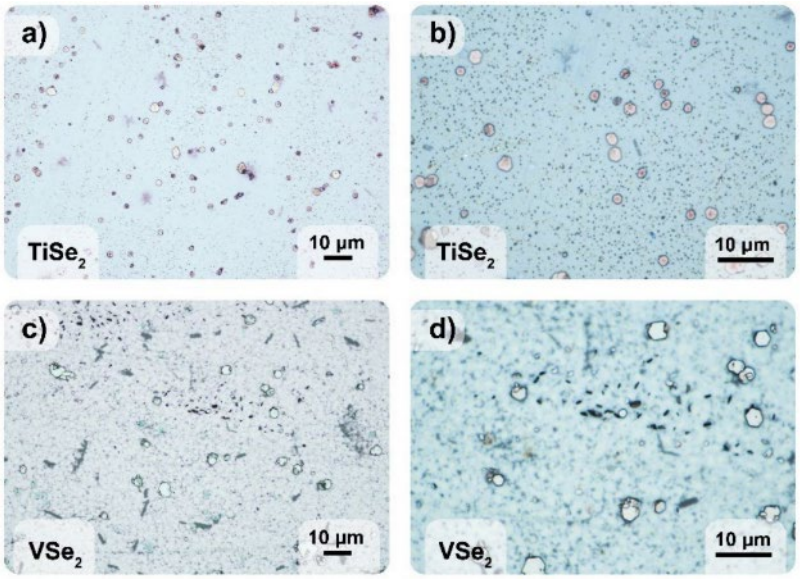

Figure 4.23: Optical images of $TiSe_2$ (a,b) and VSe_2 (c,d) thin films converted at 700°C with different magnifications, used to confirm the presence of surface crystals indicating a successful conversion of metal precursor films to their respective diselenide material.

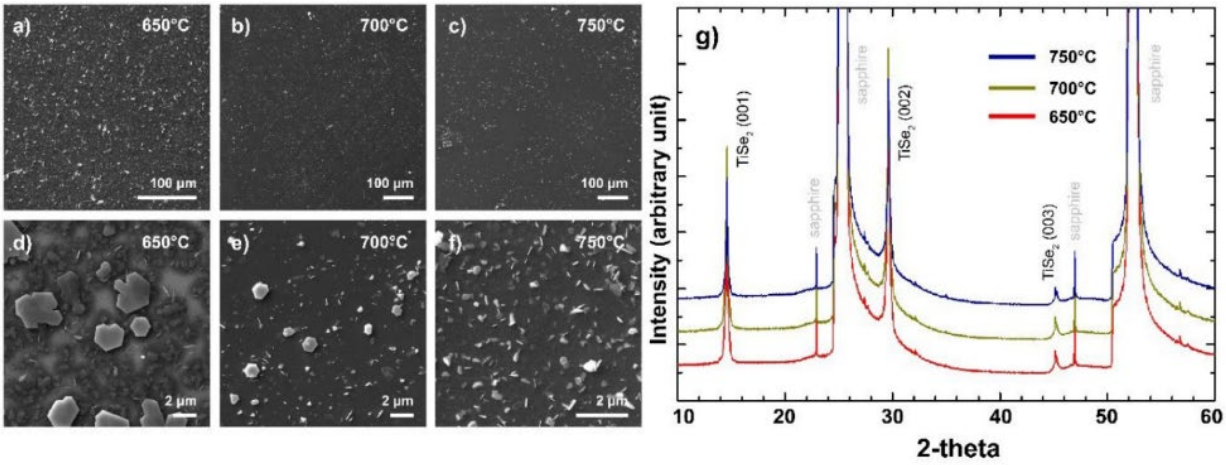

Figure 4.24: SEM images of $TiSe_2$ thin films (a,d) converted at 650°C, (b,e) at 700°C and (c,f) at 750°C. (g) XRD spectra of $TiSe_2$ thin films synthesized using different temperatures.

It's noteworthy that attempts to selenize Ti/V films using elemental Se in a quartz tube at atmospheric pressure did not trigger the desired chemical reaction. Post-selenization in ampoules, optical images *(fig. 4.23)* were taken to observe the general surface area of the films, supplemented by SEM images for closer inspection. SEM and XRD data from $TiSe_2$ films showed *(fig. 4.24)* a visible difference in surface morphology at various temperatures. At 650°C, the surface appeared coarse with large crystals, but at 700°C and 750°C, the films became smoother. The crystal size decreased from over 2µm at 650°C to less than 1µm at 750°C. The film at 650°C had uneven thickness and large crystals, while higher temperatures resulted in better thickness consistency.

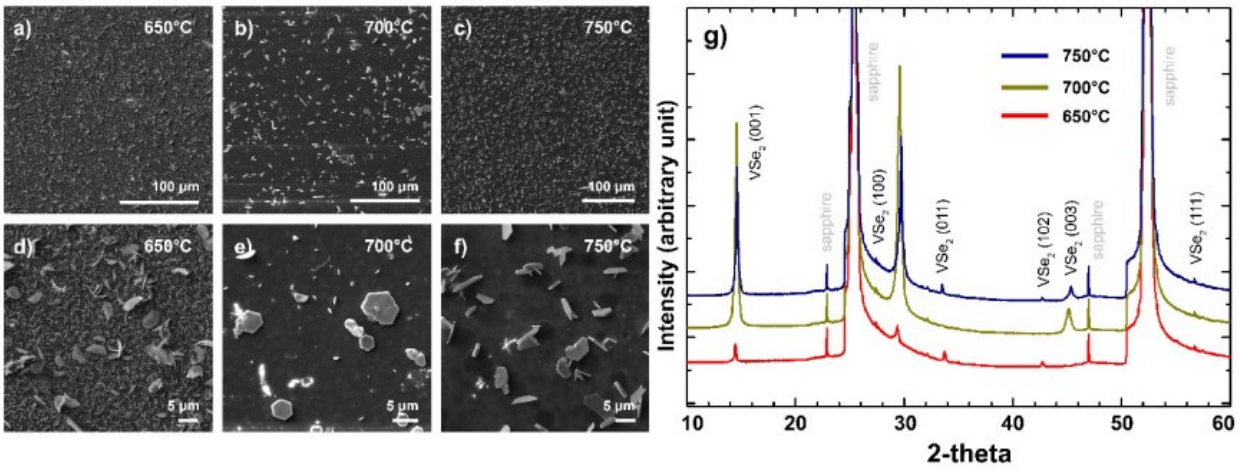

Figure 4.25: SEM images of VSe_2 thin films (a,d) converted at 650°C, (b,e) at 700°C and (c,f) at 750°C. (g) XRD spectra of synthesized VSe_2 thin films using different temperatures.

XRD patterns compared with ICDD #01-083-0980 confirmed the material composition. No drastic variations in peak positions or widths were found, though minor changes in peak intensity suggested sublimation at higher temperatures, producing thinner films. Similarly, SEM and XRD data for VSe_2 films showed *(fig. 4.25)* that, on a larger scale, the films were similar across temperatures. However, at a smaller scale, the 650°C film had out-of-plane nanocrystals, making it rougher. At 700°C and 750°C, the film lacked these nanocrystals, resulting in a smoother profile. XRD data, compared with

ICDD #04-007-5442, confirmed successful VSe_2 synthesis, with significant differences in peak intensity between 650°C and 700°C, indicating smaller crystallite size at 650°C [119–121,182].

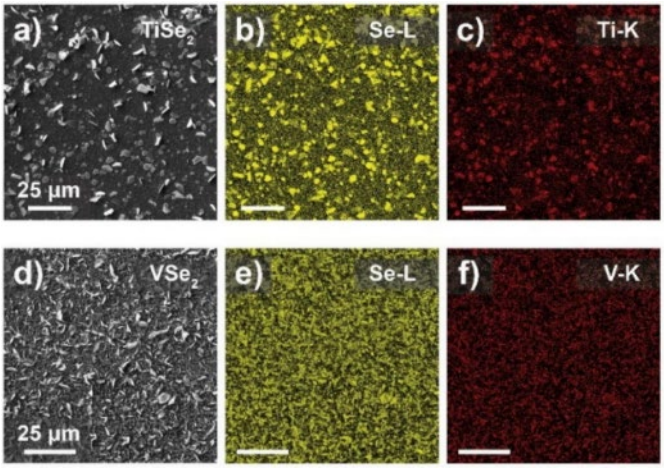

Figure 4.26: EDX elemental mapping of (a-c) $TiSe_2$ and (d-f) VSe_2 films synthesized at 650°C, shows presence and distribution of their respective elements across the film.

EDX measurements *(fig. 4.26)* for films synthesized at 650°C showed higher intensity for Ti and Se in surface crystal areas, indicating concentrated material, a trend also seen in VSe_2 films. The atomic ratio of Ti/V and Se was roughly 1:2, indicating proper stoichiometry.

4.4 Key results of the studies

4.4.1 WSe_2 Thin Films from WO_3 and W Metal Precursors

- **Methodology**:
  - Two precursor materials used: WO_3 and W metal.
  - Precursor materials deposited by DC magnetron sputtering followed by selenization using CVT at atmospheric pressure in 700°C – 800°C temperature range.
- **Characterization Findings**:
  - SEM and AFM images showed lower surface roughness in films grown from W metal precursor.
  - Films from W precursor had smaller crystal sizes (~0.4 µm) compared to WO_3 (~0.8 µm) with random orientation.
- **Photoelectric Measurements**:
  - WO_3 films exhibited higher and stable photocurrent despite out-of-plane crystal growth.
  - Both films displayed p-type conductivity.
  - WO_3 precursor films performed better electrically than W metal precursor films.

4.4.2 $ReSe_2$ Thin Films from Re Metal and ReO_x Precursors

- **Methodology**:
  - Precursor materials: Re metal and ReO_x, deposited by DC magnetron sputtering followed by selenization using CVT at atmospheric pressure.
  - Optimal synthesis temperatures: 650°C to 750°C.
- **Characterization Findings**:
  - XRD, Raman spectroscopy, and XPS confirmed polycrystalline $ReSe_2$ regardless of precursor.
  - SEM and AFM revealed surface morphology variations with temperature for Re metal-derived films.
  - ReO_x-derived films showed less temperature-dependent morphology changes.
- **Optical Properties**:
  - Minimal impact of synthesis temperature on optical properties.
  - Slight variations in absorption, with Re metal films being less sensitive to temperature changes.
  - $ReSe_2$ films found to be suitable for non-linear optics applications (Q-switching, mode-locking in laser systems).
- **Electronic Properties**:
  - Semiconductor behaviour observed only in films synthesized from ReO_x precursors.
  - Highlighted influence of precursor material on electronic properties.

4.4.3 Synthesis of $TiSe_2$ and VSe_2 thin films

- **Methodology**:
  - Two-step process: first, deposit Ti/V metal film using magnetron sputtering on substrates followed by placing the sample in a quartz ampoule with Se powder and respective metal chips, heat the ampoules in a horizontal furnace.
- **Surface Morphology**:
  - SEM revealed hexagonal crystals on the surface of both materials, varying in size and number with synthesis temperature.
  - Films remained continuous after selenization regardless of temperature.
- **Material Composition**:
  - XRD patterns confirmed $TiSe_2$ and VSe_2 composition.
  - Crystalline $TiSe_2$ synthesized successfully at 650-750°C, and VSe_2 at 700-750°C.

– EDX showed higher material concentration in surface crystal spots, with identical intensity levels in the rest of the film, confirming film continuity.

- **Potential Applications**:
  - –Approach opens possibilities for coating various substrates on a large scale.
  - –Can be extended to synthesize other TMDs.

4.4.4 Unique and novel aspects

- **WSe_2 thin films:** In other studies, it is common to use the WSe_2 obtained by exfoliation, dispersed crystals synthesized by CVD and so on [113,183–185] to show the potential applications of WSe_2. In our work, instead of trying to improve some reported quality of this material, we aim to show how combining a few main-stream techniques, we can create a novel methodology where we can readily synthesize usable quality of WSe_2 material for electronic applications on a large scale with reliability and that too involving standard photolithography for the geometry control over the material area. The quality of the material synthesized was also tested on various metrics, such as chemical state, surface morphology, electrical properties etc. where it may have not shown pristine results which one may find in exfoliated / MBE grown material, but the material shows usability and promises for the proposed method with some fine tuning. It is important to note that the synthesized material did show p-type conductivity as it is expected from this material further proving its usability for a p-n junction fabrication.
- **$ReSe_2$ thin films:** Similar to WSe_2, this material is also just exfoliated or grown using MBE or CVD for the dispersed crystals usually for the lab experiments [50,52,179,180]. To test the robustness of our methodology for a large-scale synthesis of TMD materials, $ReSe_2$ films were also synthesized in a similar way as WSe_2 thin films. The subsequent characterization of the material revealed a good quality of films which also maintained to have non-linear optical properties which is expected of this material [52,181]. In addition to that, another unique part of this study was the use of two precursors to test the effects of it on the synthesized material, where it was revealed that Re metal based $ReSe_2$ material may have in-general a unique surface texture which could be useful for surface sensitive applications such as photocatalyst [50,178].
- **$TiSe_2$ and VSe_2 thin films:** For these two materials, the methodology proposed for the synthesis of WSe_2 and $ReSe_2$ could not work, as the magnetron sputtered precursor could not be converted to their chalcogen form using ambient pressure CVT setup, due to the either precursor's high thermal stability or instability. So, for that reason, second step of our methodology was slightly tweaked for this material synthesis, where we used quartz ampoule to achieve the full conversion of these magnetron sputtered metal (Ti, V) precursors to their diselenide form. Here the main mechanism which assists in the conversion of these precursors is local low pressure, and within it high partial pressure of selenium vapour. Theoretically, these conditions can be created in a vacuum chamber if large scale production of these materials is desired. Conventionally, large scale production is not thought about [60,117,119,131,182].

5. Summary: Objectives in retrospect

1. The study developed innovative synthesis techniques tailored for producing thin films of transition metal dichalcogenides on diverse surface morphologies, spanning from one-dimensional nanowires to two-dimensional silicon and sapphire wafers. It explored a wide array of TMD materials, achieving successful growth of GaN/MoS_2 and GaN/WS_2 core–shell nanowires, ZnS/Al_2O_3/$TaSe_2$ nanowires, and WSe_2 on silicon, as well as $ReSe_2$, $TiSe_2$, and VSe_2 on sapphire substrates.

2. The study introduced novel synthesis techniques for transition metal dichalcogenides utilizing the respective transition metal as a precursor, bypassing the use of their thermally stable oxides. Specifically, $TaSe_2$ and $TiSe_2$ were synthesized from Ta and Ti metal, respectively, employing a two-step process. Initially, metal deposition was accomplished using DC magnetron sputtering, followed by the selenization of the precursor film within a vacuum-sealed quartz ampoule.

3. In this study, WSe_2 and $ReSe_2$ were successfully synthesized from their respective metal and oxide precursors using a two-step synthesis approach. Magnetron sputtering was employed to deposit the precursors onto the substrate, followed by selenization under atmospheric pressure using chemical vapor transport. This methodology, involving two types of precursors to achieve the same TMD material, facilitated a comparative analysis of the electrical properties and morphological differences between the synthesized TMDs. This comparison highlighted potential advantages of using specific precursors for particular applications.

4. The chemical and structural properties of the produced materials, MoS_2, WS_2, WSe_2, $ReSe_2$, $TaSe_2$, $TiSe_2$, and VSe_2, were comprehensively investigated using a range of characterization techniques. X-ray diffraction, Raman spectroscopy, and X-ray photoelectron spectroscopy were employed to analyse the crystalline structure and chemical composition of the synthesized materials. Additionally, scanning electron microscopy, transmission electron microscopy, and atomic force microscopy were utilized for detailed imaging and morphological analysis. These characterization methods provided a deeper understanding of the properties of each material, allowing for exploration of their potential applications in various fields. The obtained data will serve as a valuable resource for future investigations in this field, facilitating further research and development in the study of transition metal dichalcogenides.

5. In this study, standard photolithography techniques were employed to precisely control the geometry of the produced WSe_2 thin films, enabling the fabrication of tailored devices to meet specific application requirements. By integrating photolithography into the synthesis process, we successfully demonstrated the fabrication of two-contact field-effect transistors (FETs) using the synthesized WSe_2 material. Through systematic measurements and analysis conducted on the FETs, we gained insights into the electrical behaviour and performance of the synthesized material, paving the way for potential applications in electronic and optoelectronic field.

6. Main theses

1. Using Pulsed Laser Deposition, well-layered MoS_2 and WS_2 shells can be produced around GaN nanowires at temperatures near 650°C and a process pressure of $\sim 10^{-5}$ torr. Known for their potential in hydrogen evolution applications, GaN/MoS_2 and GaN/WS_2 in this core-shell nanowire form exhibit significantly increased reactive surface area, thereby enhancing their applicability in hydrogen evolution reactions. [A1]

2. Layered $TaSe_2$ is possible to produce on a variety of morphological substrates (1D nanowires, 2D flat wafers) by selenizing magnetron sputtered Ta metal film around 650°C in a vacuum-sealed quartz ampoule ($\sim 10^{-3}$ torr base pressure). [A2]

3. Patterned p-type WSe_2 thin films can be produced by integrating standard photolithography with the process of selenizing magnetron-sputtered WO_3 in a chemical vapor transport system at temperatures around 750°C and ambient pressure. [A3]

4. $ReSe_2$ film formation, achieved by selenization of magnetron-sputtered Re and ReO_x films in 750°C-850°C range using an ambient pressure chemical vapor transport system, results in films of distinct surface morphology depending on the precursor used. $ReSe_2$ films derived from Re metal exhibit a more textured surface, whereas those derived from ReO_x produce a smoother surface. [A4]

5. Production of $TiSe_2$ and VSe_2 thin films is achievable from their respective magnetron-sputtered metal films via selenization at 700°C in a selenium-rich low-pressure environment ($\sim 10^{-3}$ torr base pressure) in contrast to atmospheric pressure selenization process. [A5]

Author's publication list

Publications related to this work:

A1 – Butanovs, E., **Kadiwala, K.**, Gopejenko, A., Bocharov, D., Piskunov, S. & Polyakov, B. Different strategies for GaN-MoS_2 and GaN-WS_2 core–shell nanowire growth. Appl Surf Sci 590, (2022).

A2 – Polyakov, B., **Kadiwala, K.**, Butanovs, E., Dipane, L., Trausa, A., Bocharov, D. & Vlassov, S. Synthesis of ZnS/Al_2O_3/Ta_Se_2 Core/Shell Nanowires Using Thin Ta Metal Film Precursor. ChemEngineering 8, (2024).

A3 – **Kadiwala, K.**, Butanovs, E., Ogurcovs, A., Zubkins, M. & Polyakov, B. Comparative study of WSe_2 thin films synthesized via pre-deposited WO_3 and W precursor material selenization. J Crystal Growth 593, (2022).

A4 – **Kadiwala, K.**, Dipane, L., Dipans, E., Bundulis, A., Zubkins, M., Ogurcovs, A., Gabrusenoks, J., Bocharov, D., Butanovs, E. & Polyakov, B. Synthesis and investigation of $ReSe_2$ Thin Films Derived from Magnetron Sputtered Re and ReO_x. Crystals 14, (2024).

A5 – **Kadiwala, K.**, Dipans, E., Dipane, L., Butanovs, E. & Polyakov, B. Towards Scalable Synthesis of $TiSe_2$ and VSe_2 Thin Films. Latvian Journal of Physics and Technical Sciences 61, 13–22 (2024).

Author's other publications:

B1 – Ogurcovs, A., **Kadiwala, K.**, Sledevskis, E., Krasovska, M. & Mizers, V. Glyphosate Sensor Based on Nanostructured Water-Gated CuO Field-Effect Transistor. Sensors 22, 8744 (2022).

B2 – Ogurcovs, A., **Kadiwala, K.**, Sledevskis, E., Krasovska, M., Plaksenkova, I. & Butanovs, E. Effect of DNA Aptamer Concentration on the Conductivity of a Water-Gated Al:ZnO Thin-Film Transistor-Based Biosensor. Sensors 22, 3408 (2022).

B3 – Polyakov, B., Novikovs, A., Leimane, M., **Kadiwala, K.**, Zubkins, M., Butanovs, E., Oras, S., Damerchi, E., Zadin, V. & Vlassov, S. Comparison of the resistivities of nanostructured films made from silver, copper-silver and copper nanoparticle and nanowire suspensions. Thin Solid Films 784, 140087 (2023).

B4 – Butanovs E., Zubkins M., Strods E., Vibornijs V., **Kadiwala K.**, Ignatane L., Polyakov B., Vlassov S., Purans J., Impact of temperature and film thickness on α- and β- phase formation in Ga2O3 thin films grown on a-plane sapphire substrate, Thin Solid Films, Volume 803,2024,140467 (2024).

Author's contribution in listed publications:

A1 - Data visualization, material synthesis (PLD experiments – Shell on nanowires)

A2 - Data visualization, material synthesis (Nanowire synthesis- Core and Shell), XRD measurements.

A3 - Corresponding author, body of the article written, material synthesis (CVD synthesis), SEM, XRD measurements, device fabrication (Optical Lithography) and characterization.

A4 - Corresponding author, body of the article written, material synthesis (Magnetron Sputtering, CVD synthesis), SEM, XRD measurements and data analysis and visualization.

A5 - Corresponding author, body of the article written, material synthesis (Magnetron Sputtering, CVD synthesis), Optical images, SEM, XRD measurements and data analysis.

Participation in schools and conferences

PhD Schools

1. CAMART2 Remote Summer School [Sept 2021, online]
2. COST - International Training school Modern directions in Epitaxy [June 2022, Denmark]
3. FORTHEM – 'Escola d'Estiu Erasmus de Fisica' mobility program [July 2022, Spain]
4. European School on Nanosciences and Nanotechnologies [Aug 2022, France]
5. International Winterschool on Electronic Properties of Novel Materials [March 2023, Austria]

Conferences

1. ISSP UL 37th Scientific Conferences – [Presentation: Bottom-up synthesis of tungsten diselenide thin films and electric contact fabrication - Kevon Kadiwala, Edgars Butanovs, Martins Zubkins, Boris Polyakov] [Feb 2021, online]
2. ISSP UL 38th Scientific Conferences – [Presentation: Synthesis and characterization of 2D crystals and nanowires for the fabrication of heterojunctions - Kevon Kadiwala, Edgars Butanovs, Andrejs Ogurcovs, Boris Polyakov] [Feb 2022, Latvia]
3. Physics and Natural sciences - Open Readings – [Poster: WSe_2 thin films comparison synthesized via pre-deposited WO_3 and W precursor material selenization - Kevon Kadiwala, Edgars Butanovs, Andrejs Ogurcovs, Martins Zubkins, Boris Polyakov] [March 2022, online]
4. European Materials Research Society (E-MRS) – [Presentation: Comparative study of WSe_2 thin films synthesized via pre-deposited WO_3 and W precursor material selenization - Kevon Kadiwala, Edgars Butanovs, Andrejs Ogurcovs, Martins Zubkins, Boris Polyakov] [May 2022, online]
5. Functional materials and Nanotechnologies (FMNT) – [Poster: Thin films of WSe_2 synthesized via selenization of WO_3 and W precursor materials for characteristic comparison - Kevon Kadiwala, Edgars Butanovs, Andrejs Ogurcovs, Martins Zubkins, Boris Polyakov] [July 2022, Latvia]
6. Advanced Materials and Technologies conference (AMT) – [Poster: Characteristic assessment of WSe_2 thin films synthesized from W and WO_3 precursor materials - Kevon

Kadiwala, Edgars Butanovs, Andrejs Ogurcovs, Martins Zubkins, Boris Polyakov] [Aug 2022, Lithuania]

7. ISSP UL 39th Scientific Conferences – [Presentation: Different strategies for GaN-MoS_2 and GaN-WS_2 core–shell nanowire growth – Edgars Butanovs, Kevon Kadiwala, Aleksejs Gopejenko, Dmitry Bocharov, Sergei Piskunov, Boris Polyakov] [March 2023, Latvia]

8. ISSP UL 40th Scientific Conferences – [Presentation: Synthesis and investigation of $ReSe_2$ Thin Films Derived from Magnetron Sputtered Re and ReO_x – Kevon Kadiwala, Luize Dipane, Eriks Dipans, Arturs Bundulis, Martins Zubkins, Andrejs Ogurcovs, Jevgenijs Gabrusenoks, Dmitry Bocharov, Edgars Butanovs, Boris Polyakov] [March 2024, Latvia]

References

[1] J.D. Cain, E.D. Hanson, F. Shi, V.P. Dravid, Emerging opportunities in the two-dimensional chalcogenide systems and architecture, Curr Opin Solid State Mater Sci 20 (2016) 374–387. https://doi.org/10.1016/j.cossms.2016.06.001.

[2] P. Wang, Y. Yang, E. Pan, F. Liu, P.M. Ajayan, J. Zhou, Z. Liu, Emerging Phases of Layered Metal Chalcogenides, Small 18 (2022). https://doi.org/10.1002/smll.202105215.

[3] Y. Liu, N.O. Weiss, X. Duan, H.-C. Cheng, Y. Huang, X. Duan, Van der Waals heterostructures and devices, Nat Rev Mater 1 (2016) 16042. https://doi.org/10.1038/natrevmats.2016.42.

[4] A. McCreary, O. Kazakova, D. Jariwala, Z.Y. Al Balushi, An outlook into the flat land of 2D materials beyond graphene: synthesis, properties and device applications, 2d Mater 8 (2021) 013001. https://doi.org/10.1088/2053-1583/abc13d.

[5] S. Jain, R. Trivedi, J.K. Banshiwal, A.S. Singh, B. Chakraborty, Two-dimensional materials (2DMs): classification, preparations, functionalization and fabrication of 2DMs-oriented electrochemical sensors, in: 2D Materials-Based Electrochemical Sensors, Elsevier, 2023: pp. 45–132. https://doi.org/10.1016/B978-0-443-15293-1.00005-7.

[6] Y. Fu, Y. Liao, P. Li, H. Li, S. Jiang, H. Huang, W. Sun, T. Li, H. Yu, K. Li, H. Li, B. Jia, T. Ma, Layer structured materials for ambient nitrogen fixation, Coord Chem Rev 460 (2022) 214468. https://doi.org/10.1016/j.ccr.2022.214468.

[7] C. Tan, Z. Lai, H. Zhang, Ultrathin Two-Dimensional Multinary Layered Metal Chalcogenide Nanomaterials, Advanced Materials 29 (2017). https://doi.org/10.1002/adma.201701392.

[8] A. Majid, A. Jabeen, Transition Metal Dichalcogenides—An Important Class of Layered Materials, in: 2023: pp. 103–140. https://doi.org/10.1007/978-981-99-6299-0_5.

[9] X. Chia, Exploring layered metal chalcogenides : electrochemistry and application, Nanyang Technological University, 2018. https://doi.org/10.32657/10220/47379.

[10] J.J. Heath, M.A. Kuroda, Spin-Injection Enhancements in van der Waals Magnetic Tunnel Junctions through Barrier Engineering, Phys Rev Appl 16 (2021) L041001. https://doi.org/10.1103/PhysRevApplied.16.L041001.

[11] G. Ghimire, K.P. Dhakal, W. Choi, Y.A. Esthete, S.J. Kim, T.T. Tran, H. Lee, H. Yang, D.L. Duong, Y.-M. Kim, J. Kim, Doping-Mediated Lattice Engineering of Monolayer ReS_2 for Modulating In-Plane Anisotropy of Optical and Transport Properties, ACS Nano 15 (2021) 13770–13780. https://doi.org/10.1021/acsnano.1c05316.

[12] R. Roldán, A. Castellanos-Gomez, E. Cappelluti, F. Guinea, Strain engineering in semiconducting two-dimensional crystals, Journal of Physics: Condensed Matter 27 (2015) 313201. https://doi.org/10.1088/0953-8984/27/31/313201.

[13] J.H. Kim, H. Sung, G.-H. Lee, Phase Engineering of Two-Dimensional Transition Metal Dichalcogenides, Small Science 4 (2024). https://doi.org/10.1002/smsc.202300093.

[14] F. Yang, P. Song, M. Ruan, W. Xu, Recent progress in two-dimensional nanomaterials: Synthesis, engineering, and applications, FlatChem 18 (2019) 100133. https://doi.org/10.1016/j.flatc.2019.100133.

[15] L.M. Xie, Two-dimensional transition metal dichalcogenide alloys: preparation, characterization and applications, Nanoscale 7 (2015) 18392–18401. https://doi.org/10.1039/C5NR05712D.

[16] H. Li, Y. Shi, M.-H. Chiu, L.-J. Li, Emerging energy applications of two-dimensional layered transition metal dichalcogenides, Nano Energy 18 (2015) 293–305. https://doi.org/10.1016/j.nanoen.2015.10.023.

[17] Y. Zhao, Y. Yan, J.-M. Lee, Recent progress on transition metal diselenides from formation and modification to applications, Nanoscale 14 (2022) 1075–1095. https://doi.org/10.1039/D1NR07789A.

[18] W. Chen, E.J.G. Santos, W. Zhu, E. Kaxiras, Z. Zhang, Tuning the Electronic and Chemical Properties of Monolayer MoS_2 Adsorbed on Transition Metal Substrates, Nano Lett 13 (2013) 509–514. https://doi.org/10.1021/nl303909f.

[19] K.K. Pawar, A. Kumar, A. Mirzaei, M. Kumar, H.W. Kim, S.S. Kim, 2D nanomaterials for realization of flexible and wearable gas sensors: A review, Chemosphere 352 (2024) 141234. https://doi.org/10.1016/j.chemosphere.2024.141234.

[20] B. Radisavljevic, A. Radenovic, J. Brivio, V. Giacometti, A. Kis, Single-layer MoS2 transistors, Nat Nanotechnol 6 (2011) 147–150. https://doi.org/10.1038/nnano.2010.279.

[21] D. Lembke, S. Bertolazzi, A. Kis, Single-Layer MoS_2 Electronics, Acc Chem Res 48 (2015) 100–110. https://doi.org/10.1021/ar500274q.

[22] Q.H. Wang, K. Kalantar-Zadeh, A. Kis, J.N. Coleman, M.S. Strano, Electronics and optoelectronics of two-dimensional transition metal dichalcogenides, Nat Nanotechnol 7 (2012) 699–712. https://doi.org/10.1038/nnano.2012.193.

[23] A. Diebold, T. Hofmann, Optical and Electrical Properties of Transition Metal Dichalcogenides (Monolayer and Bulk), in: 2021: pp. 295–361. https://doi.org/10.1007/978-3-030-80323-0_8.

[24] J. Cao, Y. Zhang, C. Zhang, L. Cai, Z. Li, C. Zhou, Construction of defect-rich 1T-MoS2 towards efficient electrocatalytic hydrogen evolution: Recent advances and future perspectives, Surfaces and Interfaces 25 (2021) 101305. https://doi.org/10.1016/j.surfin.2021.101305.

[25] A. Sinha, Dhanjai, B. Tan, Y. Huang, H. Zhao, X. Dang, J. Chen, R. Jain, MoS2 nanostructures for electrochemical sensing of multidisciplinary targets: A review, TrAC Trends in Analytical Chemistry 102 (2018) 75–90. https://doi.org/10.1016/j.trac.2018.01.008.

[26] J.M. Vandenberg-Voorhoeve, Structural and Magnetic Properties of Layered Chalcogenides of the Transition Elements, in: Optical and Electrical Properties, Springer Netherlands, Dordrecht, 1976: pp. 423–457. https://doi.org/10.1007/978-94-010-1478-6_8.

[27] A. Taffelli, S. Dirè, A. Quaranta, L. Pancheri, MoS2 Based Photodetectors: A Review, Sensors 21 (2021) 2758. https://doi.org/10.3390/s21082758.

[28] S. Kim, All-2D material photonic devices, Nanoscale Adv 5 (2023) 323–328. https://doi.org/10.1039/D2NA00732K.

[29] F. Yan, C. Hu, Z. Wang, H. Lin, K. Wang, Perspectives on photodetectors based on selenides and their van der Waals heterojunctions, Appl Phys Lett 118 (2021). https://doi.org/10.1063/5.0045941.

[30] A. Pal, S. Zhang, T. Chavan, K. Agashiwala, C. Yeh, W. Cao, K. Banerjee, Quantum-Engineered Devices Based on 2D Materials for Next-Generation Information Processing and Storage, Advanced Materials 35 (2023). https://doi.org/10.1002/adma.202109894.

[31] M. Brotons-Gisbert, B.D. Gerardot, Quantum Photonics with 2D Semiconductors, in: Photonic Quantum Technologies, Wiley, 2023: pp. 563–579. https://doi.org/10.1002/9783527837427.ch20.

[32] M. Turunen, M. Brotons-Gisbert, Y. Dai, Y. Wang, E. Scerri, C. Bonato, K.D. Jöns, Z. Sun, B.D. Gerardot, Quantum photonics with layered 2D materials, Nature Reviews Physics 4 (2022) 219–236. https://doi.org/10.1038/s42254-021-00408-0.

[33] A. Reserbat-Plantey, I. Epstein, I. Torre, A.T. Costa, P.A.D. Gonçalves, N.A. Mortensen, M. Polini, J.C.W. Song, N.M.R. Peres, F.H.L. Koppens, Quantum Nanophotonics in Two-Dimensional Materials, ACS Photonics 8 (2021) 85–101. https://doi.org/10.1021/acsphotonics.0c01224.

[34] M. Kianinia, Z.-Q. Xu, M. Toth, I. Aharonovich, Quantum emitters in 2D materials: Emitter engineering, photophysics, and integration in photonic nanostructures, Appl Phys Rev 9 (2022). https://doi.org/10.1063/5.0072091.

[35] G.S. Lee, J.G. Kim, J.T. Kim, C.W. Lee, S. Cha, G.B. Choi, J. Lim, S. Padmajan Sasikala, S.O. Kim, 2D Materials Beyond Post-AI Era: Smart Fibers, Soft Robotics, and Single Atom Catalysts, Advanced Materials 36 (2024). https://doi.org/10.1002/adma.202307689.

[36] Y.-T. Guo, S.-S. Yi, Recent Advances in the Preparation and Application of Two-Dimensional Nanomaterials, Materials 16 (2023) 5798. https://doi.org/10.3390/ma16175798.

[37] Y. Jung, J. Shen, J.J. Cha, Surface effects on electronic transport of 2D chalcogenide thin films and nanostructures, Nano Converg 1 (2014) 18. https://doi.org/10.1186/s40580-014-0018-2.

[38] D.M. Soares, S. Mukherjee, G. Singh, TMDs beyond MoS_2 for Electrochemical Energy Storage, Chemistry – A European Journal 26 (2020) 6320–6341. https://doi.org/10.1002/chem.202000147.

[39] X. Wu, M. Sun, H. Yu, B. Huang, Z.L. Wang, Unraveling the unique response behaviors of ultrathin transition metal dichalcogenides to external excitations, Nano Energy 115 (2023) 108721. https://doi.org/10.1016/j.nanoen.2023.108721.

[40] S. Noreen, M.B. Tahir, A. Hussain, T. Nawaz, J.U. Rehman, A. Dahshan, M. Alzaid, H. Alrobei, Emerging 2D-Nanostructured materials for electrochemical and sensing Application-A review, Int J Hydrogen Energy 47 (2022) 1371–1389. https://doi.org/10.1016/j.ijhydene.2021.10.044.

[41] Z. Huo, Y. Wei, Y. Wang, Z.L. Wang, Q. Sun, Integrated Self-Powered Sensors Based on 2D Material Devices, Adv Funct Mater 32 (2022). https://doi.org/10.1002/adfm.202206900.

[42] J.H. Appel, D.O. Li, J.D. Podlevsky, A. Debnath, A.A. Green, Q.H. Wang, J. Chae, Low Cytotoxicity and Genotoxicity of Two-Dimensional MoS_2 and WS_2, ACS Biomater Sci Eng 2 (2016) 361–367. https://doi.org/10.1021/acsbiomaterials.5b00467.

[43] P. Karfa, K. Chandra Majhi, R. Madhuri, Synthesis of two-dimensional nanomaterials, in: Two-Dimensional Nanostructures for Biomedical Technology, Elsevier, 2020: pp. 35–71. https://doi.org/10.1016/B978-0-12-817650-4.00002-4.

[44] M. Ahmadi, O. Zabihi, S. Jeon, M. Yoonessi, A. Dasari, S. Ramakrishna, M. Naebe, 2D transition metal dichalcogenide nanomaterials: advances, opportunities, and challenges in multi-functional polymer nanocomposites, J Mater Chem A Mater 8 (2020) 845–883. https://doi.org/10.1039/C9TA10130F.

[45] Y.Y. Illarionov, G. Rzepa, M. Waltl, T. Knobloch, A. Grill, M.M. Furchi, T. Mueller, T. Grasser, The role of charge trapping in MoS2 /SiO2 and MoS2 /hBN field-effect transistors, 2d Mater 3 (2016) 035004. https://doi.org/10.1088/2053-1583/3/3/035004.

[46] L. Wei, C. Jun-fang, H. Qinyu, W. Teng, Electronic and elastic properties of MoS2, Physica B Condens Matter 405 (2010) 2498–2502. https://doi.org/10.1016/j.physb.2010.03.022.

[47] N. Choudhary, C. Li, H.-S. Chung, J. Moore, J. Thomas, Y. Jung, High-Performance One-Body Core/Shell Nanowire Supercapacitor Enabled by Conformal Growth of Capacitive 2D WS2 Layers, ACS Nano 10 (2016) 10726–10735. https://doi.org/10.1021/acsnano.6b06111.

[48] P. Lin, J. Yang, Tunable WSe2/WS2 van der Waals heterojunction for self-powered photodetector and photovoltaics, J Alloys Compd 842 (2020) 155890. https://doi.org/10.1016/j.jallcom.2020.155890.

[49] W.T. Hsu, L.S. Lu, D. Wang, J.K. Huang, M.Y. Li, T.R. Chang, Y.C. Chou, Z.Y. Juang, H.T. Jeng, L.J. Li, W.H. Chang, Evidence of indirect gap in monolayer WSe2, Nat Commun 8 (2017) 1–7. https://doi.org/10.1038/s41467-017-01012-6.

[50] A. Pandey, R. Verma, A. Srivastava, Two-dimensional ReSe2 nanosheets as a high-performance photocatalyst, New Journal of Chemistry 47 (2023) 12983–12991. https://doi.org/10.1039/D3NJ01440A.

[51] F. Cui, X. Li, Q. Feng, J. Yin, L. Zhou, D. Liu, K. Liu, X. He, X. Liang, S. Liu, Z. Lei, Z. Liu, H. Peng, J. Zhang, J. Kong, H. Xu, Epitaxial growth of large-area and highly crystalline anisotropic ReSe2 atomic layer, Nano Res 10 (2017) 2732–2742. https://doi.org/10.1007/s12274-017-1477-7.

[52] Y. Mao, H. Wang, I. Kislyakov, Z. Wang, N. Dong, J. Wang, Nonlinear optical properties and ultrafast carrier dynamics of ultrathin ReSe2, Opt Lett 48 (2023) 6259. https://doi.org/10.1364/OL.510204.

[53] X. Ye, F. Zhuang, Y. Si, J. He, Y. Xue, H. Li, K. Wang, G. Hao, R. Zhang, Direct Z-scheme GaN/WSe2 heterostructure for enhanced photocatalytic water splitting under visible spectrum, RSC Adv 13 (2023) 20179–20186. https://doi.org/10.1039/D3RA00928A.

[54] A. Kagkoura, S. Wei, L. Zeng, E. Olsson, F.M. Oliveira, J. Luxa, Z. Sofer, Mn-doped WSe2 as an efficient electrocatalyst for hydrogen production and as anode material for lithium-ion batteries, Nanoscale (2025). https://doi.org/10.1039/D4NR04348K.

[55] R. Hu, H. Wang, Y. Gao, Y. Li, A. Cao, Z. Wang, L. Shang, Y. Li, K. Jiang, J. Zhang, L. Zhu, Z. Hu, Near-Infrared Photoresponse Driven by Strong Interlayer Transition in 2D MoSe2 /WSe2 van der Waals Heterostructures: Implications for Broadband Photodetectors, ACS Appl Nano Mater (2024). https://doi.org/10.1021/acsanm.4c06290.

[56] X.P. Le, A. Venkatesan, D. Daw, T.A. Nguyen, M. Baithi, H. Bouzid, T.D. Nguyen, High-Performance p-Type Quasi-Ohmic of WSe2 Transistors Using Vanadium-Doped WSe_2 as Intermediate Layer Contact, ACS Appl Mater Interfaces 16 (2024) 52645–52652. https://doi.org/10.1021/acsami.4c10249.

[57] A.M.R. Ramírez, S. Heidari, A. Vergara, M.V. Aguilera, P. Preuss, M.B. Camarada, A. Fischer, Rhenium-Based Electrocatalysts for Water Splitting, ACS Materials Au 3 (2023) 177–200. https://doi.org/10.1021/acsmaterialsau.2c00077.

[58] B. Silva, J. Rodrigues, B. Sompalle, C.-D. Liao, N. Nicoara, J. Borme, F. Cerqueira, M. Claro, S. Sadewasser, P. Alpuim, A. Capasso, Efficient ReSe2 Photodetectors with CVD Single-Crystal Graphene Contacts, Nanomaterials 11 (2021) 1650. https://doi.org/10.3390/nano11071650.

[59] Y. Sang, M. Xu, J. Huang, L. Jian, W. Gao, Y. Sun, Z. Zheng, Y. Yan, M. Yang, J. Li, Polarization-sensitive UV photodetector based on ReSe2 /GaN mixed-dimensional heterojunction, Opt Lett 48 (2023) 6108. https://doi.org/10.1364/OL.505797.

[60] J. Joshi, B. Scharf, I. Mazin, S. Krylyuk, D.J. Campbell, J. Paglione, A. Davydov, I. Žutić, P.M. Vora, Charge density wave activated excitons in TiSe2–MoSe2 heterostructures, APL Mater 10 (2022). https://doi.org/10.1063/5.0067098.

[61] S. Lee, T.B. Park, J. Kim, S.-G. Jung, W.K. Seong, N. Hur, Y. Luo, D.Y. Kim, T. Park, Tuning the charge density wave quantum critical point and the appearance of superconductivity in <math> <mrow> <mi>Ti</mi> <msub> <mi>Se</mi> <mn>2</mn> </msub> </mrow> </math>, Phys Rev Res 3 (2021) 033097. https://doi.org/10.1103/PhysRevResearch.3.033097.

[62] H.D. Ozaydin, H. Sahin, J. Kang, F.M. Peeters, R.T. Senger, Electronic and magnetic properties of 1 T-TiS2 nanoribbons, 2d Mater 2 (2015) 044002. https://doi.org/10.1088/2053-1583/2/4/044002.

[63] Y. Wang, J. Wan, W. Tian, Z. Hou, X. Gu, Y. Wang, Theoretical screening of VSe2 as support for enhanced electrocatalytic performance of transition-metal single atoms, J Colloid Interface Sci 590 (2021) 210–218. https://doi.org/10.1016/j.jcis.2021.01.062.

[64] J.S. Ponraj, Z.-Q. Xu, S.C. Dhanabalan, H. Mu, Y. Wang, J. Yuan, P. Li, S. Thakur, M. Ashrafi, K. Mccoubrey, Y. Zhang, S. Li, H. Zhang, Q. Bao, Photonics and optoelectronics of two-dimensional materials beyond graphene, Nanotechnology 27 (2016) 462001. https://doi.org/10.1088/0957-4484/27/46/462001.

[65] C.C. Mayorga-Martinez, A. Ambrosi, A.Y.S. Eng, Z. Sofer, M. Pumera, Transition metal dichalcogenides (MoS2, MoSe2, WS2 and WSe2) exfoliation technique has strong influence upon their capacitance, Electrochem Commun 56 (2015) 24–28. https://doi.org/10.1016/j.elecom.2015.03.017.

[66] M. Dragoman, D. Dragoman, I. Tiginyanu, Atomically thin semiconducting layers and nanomembranes: a review, Semicond Sci Technol 32 (2017) 033001. https://doi.org/10.1088/1361-6641/aa5206.

[67] J. Zhu, R. Yang, G. Zhang, Atomically thin transition metal dichalcogenides for the hydrogen evolution reaction, ChemPhysMater 1 (2022) 102–111. https://doi.org/10.1016/j.chphma.2021.11.005.

[68] J. Lee, S. Cho, S. Park, H. Bae, M. Noh, B. Kim, C. In, S. Yang, S. Lee, S.Y. Seo, J. Kim, C.-H. Lee, W.-Y. Shim, M.-H. Jo, D. Kim, H. Choi, Highly efficient computer algorithm for identifying layer thickness of atomically thin 2D materials, J Phys D Appl Phys 51 (2018) 11LT03. https://doi.org/10.1088/1361-6463/aaac19.

[69] X. Duan, C. Wang, A. Pan, R. Yu, X. Duan, Two-dimensional transition metal dichalcogenides as atomically thin semiconductors: opportunities and challenges, Chem Soc Rev 44 (2015) 8859–8876. https://doi.org/10.1039/C5CS00507H.

[70] R. Wu, Q. Tao, W. Dang, Y. Liu, B. Li, J. Li, B. Zhao, Z. Zhang, H. Ma, G. Sun, X. Duan, X. Duan, van der Waals Epitaxial Growth of Atomically Thin 2D Metals on Dangling-Bond-Free WSe_2 and WS_2, Adv Funct Mater 29 (2019). https://doi.org/10.1002/adfm.201806611.

[71] M. Nakano, Y. Wang, Y. Kashiwabara, H. Matsuoka, Y. Iwasa, Layer-by-Layer Epitaxial Growth of Scalable WSe2 on Sapphire by Molecular Beam Epitaxy, Nano Lett 17 (2017) 5595–5599. https://doi.org/10.1021/acs.nanolett.7b02420.

[72] C. Tan, X. Cao, X.-J. Wu, Q. He, J. Yang, X. Zhang, J. Chen, W. Zhao, S. Han, G.-H. Nam, M. Sindoro, H. Zhang, Recent Advances in Ultrathin Two-Dimensional Nanomaterials, Chem Rev 117 (2017) 6225–6331. https://doi.org/10.1021/acs.chemrev.6b00558.

[73] K. Chen, L. Shi, Y. Zhang, Z. Liu, Scalable chemical-vapour-deposition growth of three-dimensional graphene materials towards energy-related applications, Chem Soc Rev 47 (2018) 3018–3036. https://doi.org/10.1039/c7cs00852j.

[74] L. Sun, G. Yuan, L. Gao, J. Yang, M. Chhowalla, M.H. Gharahcheshmeh, K.K. Gleason, Y.S. Choi, B.H. Hong, Z. Liu, Chemical vapour deposition, Nature Reviews Methods Primers 1 (2021) 5. https://doi.org/10.1038/s43586-020-00005-y.

[75] T. Kwak, J. Lee, B. So, U. Choi, O. Nam, Growth behavior of wafer-scale two-dimensional MoS 2 layer growth using metal-organic chemical vapor deposition, J Cryst Growth 510 (2019) 50–55. https://doi.org/10.1016/j.jcrysgro.2019.01.020.

[76] N.A. Shepelin, Z.P. Tehrani, N. Ohannessian, C.W. Schneider, D. Pergolesi, T. Lippert, A practical guide to pulsed laser deposition, Chem Soc Rev 52 (2023) 2294–2321. https://doi.org/10.1039/D2CS00938B.

[77] M.J. Aziz, Film growth mechanisms in pulsed laser deposition, Applied Physics A 93 (2008) 579–587. https://doi.org/10.1007/s00339-008-4696-7.

[78] F. Bertoldo, R.R. Unocic, Y.-C. Lin, X. Sang, A.A. Puretzky, Y. Yu, D. Miakota, C.M. Rouleau, J. Schou, K.S. Thygesen, D.B. Geohegan, S. Canulescu, Intrinsic Defects in MoS2 Grown by Pulsed Laser Deposition: From Monolayers to Bilayers, ACS Nano 15 (2021) 2858–2868. https://doi.org/10.1021/acsnano.0c08835.

[79] P. Panjan, A. Drnovšek, P. Gselman, M. Čekada, M. Panjan, Review of Growth Defects in Thin Films Prepared by PVD Techniques, Coatings 10 (2020) 447. https://doi.org/10.3390/coatings10050447.

[80] Y. Shi, H. Li, L.-J. Li, Recent advances in controlled synthesis of two-dimensional transition metal dichalcogenides via vapour deposition techniques, Chem Soc Rev 44 (2015) 2744–2756. https://doi.org/10.1039/C4CS00256C.

[81] R. Sahoo, M. Singh, T.N. Rao, A Review on the Current Progress and Challenges of 2D Layered Transition Metal Dichalcogenides as Li/Na-ion Battery Anodes, ChemElectroChem 8 (2021) 2358–2396. https://doi.org/10.1002/celc.202100197.

[82] V. Sorkin, H. Pan, H. Shi, S.Y. Quek, Y.W. Zhang, Nanoscale Transition Metal Dichalcogenides: Structures, Properties, and Applications, Critical Reviews in Solid State and Materials Sciences 39 (2014) 319–367. https://doi.org/10.1080/10408436.2013.863176.

[83] Z. Xu, H. Yang, X. Song, Y. Chen, H. Yang, M. Liu, Z. Huang, Q. Zhang, J. Sun, L. Liu, Y. Wang, Topical review: recent progress of charge density waves in 2D transition metal dichalcogenide-based heterojunctions and their applications, Nanotechnology 32 (2021) 492001. https://doi.org/10.1088/1361-6528/ac21ed.

[84] D. Mouloua, A. Kotbi, G. Deokar, K. Kaja, M. El Marssi, M.A. EL Khakani, M. Jouiad, Recent Progress in the Synthesis of MoS2 Thin Films for Sensing, Photovoltaic and Plasmonic Applications: A Review, Materials 14 (2021) 3283. https://doi.org/10.3390/ma14123283.

[85] H. Chen, J. Zhang, D. Kan, J. He, M. Song, J. Pang, S. Wei, K. Chen, The Recent Progress of Two-Dimensional Transition Metal Dichalcogenides and Their Phase Transition, Crystals (Basel) 12 (2022) 1381. https://doi.org/10.3390/cryst12101381.

[86] T.F. Schranghamer, M. Sharma, R. Singh, S. Das, Review and comparison of layer transfer methods for two-dimensional materials for emerging applications, Chem Soc Rev 50 (2021) 11032–11054. https://doi.org/10.1039/D1CS00706H.

[87] Y. Chang, N. Yang, J. Min, F. Zheng, C. Huang, J. Chen, Y. Zhang, P. Yang, C. Li, H. Liu, B. Ye, J. Xu, H. Chen, Z. Luo, W. Wu, K. Shih, J. Huang, L. Li, Y. Wan, Atomically Thin Decoration Layers for Robust Orientation Control of 2D Transition Metal Dichalcogenides, Adv Funct Mater 34 (2024). https://doi.org/10.1002/adfm.202311387.

[88] Y. Yi, Z. Chen, X. Yu, Z. Zhou, J. Li, Recent Advances in Quantum Effects of 2D Materials, Adv Quantum Technol 2 (2019). https://doi.org/10.1002/qute.201800111.

[89] H.H. Huang, X. Fan, D.J. Singh, W.T. Zheng, Recent progress of TMD nanomaterials: phase transitions and applications, Nanoscale 12 (2020) 1247–1268. https://doi.org/10.1039/C9NR08313H.

[90] K. Khan, A.K. Tareen, M. Aslam, R. Wang, Y. Zhang, A. Mahmood, Z. Ouyang, H. Zhang, Z. Guo, Recent developments in emerging two-dimensional materials and their applications, J Mater Chem C Mater 8 (2020) 387–440. https://doi.org/10.1039/C9TC04187G.

[91] Z. Zheng, T. Zhang, J. Yao, Y. Zhang, J. Xu, G. Yang, Flexible, transparent and ultra-broadband photodetector based on large-area WSe2 film for wearable devices, Nanotechnology 27 (2016) 1–11. https://doi.org/10.1088/0957-4484/27/22/225501.

[92] J. Ding, A. Feng, X. Li, S. Ding, L. Liu, W. Ren, Properties, preparation, and application of tungsten disulfide: a review, J Phys D Appl Phys 54 (2021) 173002. https://doi.org/10.1088/1361-6463/abd9e8.

[93] J.H. Han, M. Kwak, Y. Kim, J. Cheon, Recent Advances in the Solution-Based Preparation of Two-Dimensional Layered Transition Metal Chalcogenide Nanostructures, Chem Rev 118 (2018) 6151–6188. https://doi.org/10.1021/acs.chemrev.8b00264.

[94] M. Chhowalla, Z. Liu, H. Zhang, Two-dimensional transition metal dichalcogenide (TMD) nanosheets, Chem Soc Rev 44 (2015) 2584–2586. https://doi.org/10.1039/C5CS90037A.

[95] Y. Lee, J. Kim, Controlling Lattice Defects and Inter-Exciton Interactions in Monolayer Transition Metal Dichalcogenides for Efficient Light Emission, ACS Photonics 5 (2018) 4187–4194. https://doi.org/10.1021/acsphotonics.8b00645.

[96] D. Wolverson, L.S. Hart, Lattice Dynamics of the Rhenium and Technetium Dichalcogenides, Nanoscale Res Lett 11 (2016) 250. https://doi.org/10.1186/s11671-016-1459-9.

[97] J. Jadczak, J. Kutrowska-Girzycka, M. Bieniek, T. Kazimierczuk, P. Kossacki, J.J. Schindler, J. Debus, K. Watanabe, T. Taniguchi, C.H. Ho, A. Wójs, P. Hawrylak, L. Bryja, Probing negatively charged and neutral excitons in MoS2 /hBN and hBN /MoS2 /hBN van der Waals heterostructures, Nanotechnology 32 (2021) 145717. https://doi.org/10.1088/1361-6528/abd507.

[98] L. Cai, H. Duan, Q. Liu, C. Wang, H. Tan, W. Hu, F. Hu, Z. Sun, W. Yan, Ultrahigh-temperature ferromagnetism in MoS2 Moiré superlattice/graphene hybrid heterostructures, Nano Res 14 (2021) 4182–4187. https://doi.org/10.1007/s12274-021-3360-9.

[99] D.J. Trainer, A. V. Putilov, B. Wang, C. Lane, T. Saari, T.-R. Chang, H.-T. Jeng, H. Lin, X. Xi, J. Nieminen, A. Bansil, M. Iavarone, Moiré superlattices and 2D electronic properties of graphite/MoS2 heterostructures, Journal of Physics and Chemistry of Solids 128 (2019) 325–330. https://doi.org/10.1016/j.jpcs.2017.10.034.

[100] R.K. Mishra, K. Verma, D. sethi singh, Defect engineering in nanomaterials: Impact, challenges, and applications, Smart Materials in Manufacturing 2 (2024) 100052. https://doi.org/10.1016/j.smmf.2024.100052.

[101] S. Yu, Q. Rice, B. Tabibi, Q. Li, F.J. Seo, Piezoelectricity in WSe2/MoS2 heterostructure atomic layers, Nanoscale 10 (2018) 12472–12479. https://doi.org/10.1039/c8nr04394a.

[102] C. Huang, S. Wu, A.M. Sanchez, J.J.P. Peters, R. Beanland, J.S. Ross, P. Rivera, W. Yao, D.H. Cobden, X. Xu, Lateral heterojunctions within monolayer MoSe2-WSe2 semiconductors, Nat Mater 13 (2014) 1096–1101. https://doi.org/10.1038/nmat4064.

[103] A.K. Geim, I. V. Grigorieva, Van der Waals heterostructures, Nature 499 (2013) 419–425. https://doi.org/10.1038/nature12385.

[104] K.-K. Liu, W. Zhang, Y.-H. Lee, Y.-C. Lin, M.-T. Chang, C.-Y. Su, C.-S. Chang, H. Li, Y. Shi, H. Zhang, C.-S. Lai, L.-J. Li, Growth of Large-Area and Highly Crystalline MoS2 Thin Layers on Insulating Substrates, Nano Lett 12 (2012) 1538–1544. https://doi.org/10.1021/nl2043612.

[105] N. Bandaru, R.S. Kumar, D. Sneed, O. Tschauner, J. Baker, D. Antonio, S.-N. Luo, T. Hartmann, Y. Zhao, R. Venkat, Effect of Pressure and Temperature on Structural Stability of MoS2, The Journal of Physical Chemistry C 118 (2014) 3230–3235. https://doi.org/10.1021/jp410167k.

[106] A. Jain, S.P. Ong, G. Hautier, W. Chen, W.D. Richards, S. Dacek, S. Cholia, D. Gunter, D. Skinner, G. Ceder, K.A. Persson, Commentary: The Materials Project: A materials genome approach to accelerating materials innovation, APL Mater 1 (2013). https://doi.org/10.1063/1.4812323.

[107] M. Okada, T. Sawazaki, K. Watanabe, T. Taniguch, H. Hibino, H. Shinohara, R. Kitaura, Direct Chemical Vapor Deposition Growth of WS2 Atomic Layers on Hexagonal Boron Nitride, ACS Nano 8 (2014) 8273–8277. https://doi.org/10.1021/nn503093k.

[108] S.V.P. Vattikuti, C. Byon, V. Chitturi, Selective hydrothermally synthesis of hexagonal WS2 platelets and their photocatalytic performance under visible light irradiation, Superlattices Microstruct 94 (2016) 39–50. https://doi.org/10.1016/j.spmi.2016.03.042.

[109] A. Ennaoui, K. Diesner, S. Fiechter, J.H. Moser, F. Lévy, Structural analysis of 2H–WS2 thin films by X-ray and TEM investigation, Thin Solid Films 311 (1997) 146–150. https://doi.org/10.1016/S0040-6090(97)00473-2.

[110] G.A. Wiegers, J.L. de Boer, A. Meetsma, S. van Smaalen, Domain structure and refinement of the triclinic superstructure of 1T-TaSe2 by single crystal X-ray diffraction, Z Kristallogr Cryst Mater 216 (2001) 45–50. https://doi.org/10.1524/zkri.216.1.45.18999.

[111] Y. Wu, J. He, J. Liu, H. Xing, Z. Mao, Y. Liu, Dimensional reduction and ionic gating induced enhancement of superconductivity in atomically thin crystals of 2H-TaSe2, Nanotechnology 30 (2019) 035702. https://doi.org/10.1088/1361-6528/aaea3b.

[112] Y. Wu, H. Xing, C.-S. Lian, H. Lian, J. He, W. Duan, J. Liu, Z. Mao, Y. Liu, Ion intercalation engineering of electronic properties of two-dimensional crystals of 2H-TaSe2, Phys Rev Mater 3 (2019) 104003. https://doi.org/10.1103/PhysRevMaterials.3.104003.

[113] J. Chen, B. Liu, Y. Liu, W. Tang, C.T. Nai, L. Li, J. Zheng, L. Gao, Y. Zheng, H.S. Shin, H.Y. Jeong, K.P. Loh, Chemical Vapor Deposition of Large-Sized Hexagonal WSe2 Crystals on Dielectric Substrates, Advanced Materials 27 (2015) 6722–6727. https://doi.org/10.1002/adma.201503446.

[114] H. Zhou, C. Wang, J.C. Shaw, R. Cheng, Y. Chen, X. Huang, Y. Liu, N.O. Weiss, Z. Lin, Y. Huang, X. Duan, Large Area Growth and Electrical Properties of p-Type WSe2 Atomic Layers, Nano Lett 15 (2015) 709–713. https://doi.org/10.1021/nl504256y.

[115] G.C. Resende, G.A.S. Ribeiro, O.J. Silveira, J.S. Lemos, J.C. Brant, D. Rhodes, L. Balicas, M. Terrones, M.S.C. Mazzoni, C. Fantini, B.R. Carvalho, M.A. Pimenta, Origin of the complex Raman tensor elements in single-layer triclinic ReSe2, 2d Mater 8 (2021) 025002. https://doi.org/10.1088/2053-1583/abce07.

[116] M.M.A. Mahmoud, D.P. Joubert, First principles study of the structural, stability properties and lattice thermal conductivity of bulk ReSe2, Mater Today Proc 5 (2018) 10424–10430. https://doi.org/10.1016/j.matpr.2017.12.201.

[117] F.C. Brown, Electronic and vibronic structure of TiS2 and TiSe2, Physica B+C 99 (1980) 264–270. https://doi.org/10.1016/0378-4363(80)90243-0.

[118] D.J. Campbell, C. Eckberg, P.Y. Zavalij, H.-H. Kung, E. Razzoli, M. Michiardi, C. Jozwiak, A. Bostwick, E. Rotenberg, A. Damascelli, J. Paglione, Intrinsic insulating ground state in transition metal dichalcogenide TiSe2, Phys Rev Mater 3 (2019) 053402. https://doi.org/10.1103/PhysRevMaterials.3.053402.

[119] P. Goli, J. Khan, D. Wickramaratne, R.K. Lake, A.A. Balandin, Charge Density Waves in Exfoliated Films of van der Waals Materials: Evolution of Raman Spectrum in TiSe2, Nano Lett 12 (2012) 5941–5945. https://doi.org/10.1021/nl303365x.

[120] A. Feroze, H.R. Na, Y.C. Park, J.-H. Jun, M.-H. Jung, J.-H. Lee, J.-H. Kim, M.-J. Seong, S. Hong, S.-H. Chun, S. Lee, In-Depth Structural Characterization of 1T-VSe2 Single Crystals Grown by Chemical Vapor Transport, Cryst Growth Des 20 (2020) 2860–2865. https://doi.org/10.1021/acs.cgd.0c00219.

[121] F. Li, K. Tu, Z. Chen, Versatile Electronic Properties of VSe2 Bulk, Few-Layers, Monolayer, Nanoribbons, and Nanotubes: A Computational Exploration, The Journal of Physical Chemistry C 118 (2014) 21264–21274. https://doi.org/10.1021/jp507093t.

[122] S. Das, N. Mohapatra, Tunable Physical Properties of VSe2 hexagonal disks, J Phys Conf Ser 2518 (2023) 012010. https://doi.org/10.1088/1742-6596/2518/1/012010.

[123] Q. Zeng, H. Wang, W. Fu, Y. Gong, W. Zhou, P.M. Ajayan, J. Lou, Z. Liu, Band Engineering for Novel Two-Dimensional Atomic Layers, Small 11 (2015) 1868–1884. https://doi.org/10.1002/smll.201402380.

[124] X. Zhang, X.-F. Qiao, W. Shi, J.-B. Wu, D.-S. Jiang, P.-H. Tan, Phonon and Raman scattering of two-dimensional transition metal dichalcogenides from monolayer, multilayer to bulk material, Chem Soc Rev 44 (2015) 2757–2785. https://doi.org/10.1039/C4CS00282B.

[125] K.F. Mak, J. Shan, Photonics and optoelectronics of 2D semiconductor transition metal dichalcogenides, Nat Photonics 10 (2016) 216–226. https://doi.org/10.1038/nphoton.2015.282.

[126] J. Sun, Y. Wang, S. Guo, B. Wan, L. Dong, Y. Gu, C. Song, C. Pan, Q. Zhang, L. Gu, F. Pan, J. Zhang, Lateral 2D WSe2 p–n Homojunction Formed by Efficient Charge-Carrier-Type Modulation for

High-Performance Optoelectronics, Advanced Materials 32 (2020) 1–9. https://doi.org/10.1002/adma.201906499.

[127] Y. Deng, X. Zhao, C. Zhu, P. Li, R. Duan, G. Liu, Z. Liu, MoTe2 : Semiconductor or Semimetal?, ACS Nano 15 (2021) 12465–12474. https://doi.org/10.1021/acsnano.1c01816.

[128] M.B. Vellinga, R. de Jonge, C. Haas, Semiconductor to metal transition in MoTe2, J Solid State Chem 2 (1970) 299–302. https://doi.org/10.1016/0022-4596(70)90085-X.

[129] L.G. Pimenta Martins, R. Comin, M.J.S. Matos, M.S.C. Mazzoni, B.R.A. Neves, M. Yankowitz, High-pressure studies of atomically thin van der Waals materials, Appl Phys Rev 10 (2023). https://doi.org/10.1063/5.0123283.

[130] L. Zhang, Y. Tang, A.R. Khan, M.M. Hasan, P. Wang, H. Yan, T. Yildirim, J.F. Torres, G.P. Neupane, Y. Zhang, Q. Li, Y. Lu, 2D Materials and Heterostructures at Extreme Pressure, Advanced Science 7 (2020). https://doi.org/10.1002/advs.202002697.

[131] K. Sugawara, Y. Nakata, R. Shimizu, P. Han, T. Hitosugi, T. Sato, T. Takahashi, Unconventional Charge-Density-Wave Transition in Monolayer 1T-TiSe2, ACS Nano 10 (2016) 1341–1345. https://doi.org/10.1021/acsnano.5b06727.

[132] J. Dai, E. Calleja, J. Alldredge, X. Zhu, L. Li, W. Lu, Y. Sun, T. Wolf, H. Berger, K. McElroy, Microscopic evidence for strong periodic lattice distortion in two-dimensional charge-density wave systems, Phys Rev B 89 (2014) 165140. https://doi.org/10.1103/PhysRevB.89.165140.

[133] Q. Tang, Tuning the phase stability of Mo-based TMD monolayers through coupled vacancy defects and lattice strain, J Mater Chem C Mater 6 (2018) 9561–9568. https://doi.org/10.1039/C8TC03430C.

[134] T. Shen, A. V. Penumatcha, J. Appenzeller, Strain Engineering for Transition Metal Dichalcogenides Based Field Effect Transistors, ACS Nano 10 (2016) 4712–4718. https://doi.org/10.1021/acsnano.6b01149.

[135] M. Ghorbani-Asl, S. Borini, A. Kuc, T. Heine, Strain-dependent modulation of conductivity in single-layer transition-metal dichalcogenides, Phys Rev B 87 (2013) 235434. https://doi.org/10.1103/PhysRevB.87.235434.

[136] H. Yoo, K. Heo, Md.H.R. Ansari, S. Cho, Recent Advances in Electrical Doping of 2D Semiconductor Materials: Methods, Analyses, and Applications, Nanomaterials 11 (2021) 832. https://doi.org/10.3390/nano11040832.

[137] B. Balasubramaniam, N. Singh, P. Kar, A. Tyagi, J. Prakash, R.K. Gupta, Engineering of transition metal dichalcogenide-based 2D nanomaterials through doping for environmental applications, Mol Syst Des Eng 4 (2019) 804–827. https://doi.org/10.1039/C8ME00116B.

[138] S. Zhang, H.M. Hill, K. Moudgil, C.A. Richter, A.R. Hight Walker, S. Barlow, S.R. Marder, C.A. Hacker, S.J. Pookpanratana, Controllable, Wide-Ranging n-Doping and p-Doping of Monolayer Group 6 Transition-Metal Disulfides and Diselenides, Advanced Materials 30 (2018). https://doi.org/10.1002/adma.201802991.

[139] J. Musil, P. Baroch, J. Vlček, K.H. Nam, J.G. Han, Reactive magnetron sputtering of thin films: present status and trends, Thin Solid Films 475 (2005) 208–218. https://doi.org/10.1016/j.tsf.2004.07.041.

[140] S.M. Rossnagel, Magnetron sputtering, Journal of Vacuum Science & Technology A: Vacuum, Surfaces, and Films 38 (2020). https://doi.org/10.1116/6.0000594.

[141] R.K. Crouch, W.J. Debnam, R. Ryan, Vacuum tight quartz ampoule for bridgman growth of crystals with interface demarcation, J Cryst Growth 56 (1982) 215–216. https://doi.org/10.1016/0022-0248(82)90031-8.

[142] A. Balgarkashi, V. Piazza, J. Jasinski, R. Frisenda, A. Surrente, M. Baranowski, M. Dimitrievska, D. Dede, W. Kim, L. Guniat, J.-B. Leran, A. Castellanos-Gomez, P. Plochocka, A. Fontcuberta i Morral, Spatial Modulation of Vibrational and Luminescence Properties of Monolayer MoS_2 Using a GaAs Nanowire Array, IEEE J Quantum Electron 58 (2022) 1–8. https://doi.org/10.1109/JQE.2022.3167480.

[143] Y. Yu, Z. Li, Z. Lu, X. Geng, Y. Lu, G. Xu, L. Wang, J. Jie, Graphene/MoS2 /Si Nanowires Schottky-NP Bipolar van der Waals Heterojunction for Ultrafast Photodetectors, IEEE Electron Device Letters 39 (2018) 1688–1691. https://doi.org/10.1109/LED.2018.2872107.

[144] J.H. Kim, H.S. Lee, G.H. An, J. Lee, H.M. Oh, J. Choi, Y.H. Lee, Dielectric Nanowire Hybrids for Plasmon-Enhanced Light–Matter Interaction in 2D Semiconductors, ACS Nano 14 (2020) 11985–11994. https://doi.org/10.1021/acsnano.0c05158.

[145] Q. An, Y. Liu, R. Jiang, X. Meng, Chemical vapor deposition growth of ReS2 nanowires for high-performance nanostructured photodetector, Nanoscale 10 (2018) 14976–14983. https://doi.org/10.1039/C8NR04143A.

[146] K. Chen, J. Pan, W. Yin, C. Ma, L. Wang, Flexible electronics based on one-dimensional inorganic semiconductor nanowires and two-dimensional transition metal dichalcogenides, Chinese Chemical Letters 34 (2023) 108226. https://doi.org/10.1016/j.cclet.2023.108226.

[147] X. Jia, X. Zhu, W. Tian, Y. Ding, X. Tian, B. Cheng, L. Cheng, S. Bai, Y. Qin, Nanowire templated CVD synthesis and morphological control of MoS2 nanotubes, J Mater Chem C Mater 8 (2020) 4133–4138. https://doi.org/10.1039/C9TC06060J.

[148] E. Butanovs, A. Kuzmin, S. Piskunov, K. Smits, A. Kalinko, B. Polyakov, Synthesis and characterization of GaN/ReS2, ZnS/ReS2 and ZnO/ReS2 core/shell nanowire heterostructures, Appl Surf Sci 536 (2021) 2–9. https://doi.org/10.1016/j.apsusc.2020.147841.

[149] W.-C. Shen, R.-S. Chen, Y.-S. Huang, Photoconductivities in MoS2 Nanoflake Photoconductors, Nanoscale Res Lett 11 (2016) 124. https://doi.org/10.1186/s11671-016-1331-y.

[150] F. Reale, K. Sharda, C. Mattevi, From bulk crystals to atomically thin layers of group VI-transition metal dichalcogenides vapour phase synthesis, Appl Mater Today 3 (2016) 11–22. https://doi.org/10.1016/j.apmt.2015.12.003.

[151] R. Gatensby, T. Hallam, K. Lee, N. McEvoy, G.S. Duesberg, Investigations of vapour-phase deposited transition metal dichalcogenide films for future electronic applications, Solid State Electron 125 (2016) 39–51. https://doi.org/10.1016/j.sse.2016.07.021.

[152] A.T. Hoang, K. Qu, X. Chen, J.-H. Ahn, Large-area synthesis of transition metal dichalcogenides via CVD and solution-based approaches and their device applications, Nanoscale 13 (2021) 615–633. https://doi.org/10.1039/D0NR08071C.

[153] S. V Mandyam, H.M. Kim, M. Drndić, Large area few-layer TMD film growths and their applications, Journal of Physics: Materials 3 (2020) 024008. https://doi.org/10.1088/2515-7639/ab82b3.

[154] Y. Zhang, Y. Yao, M.G. Sendeku, L. Yin, X. Zhan, F. Wang, Z. Wang, J. He, Recent Progress in CVD Growth of 2D Transition Metal Dichalcogenides and Related Heterostructures, Advanced Materials 31 (2019). https://doi.org/10.1002/adma.201901694.

[155] B. Polyakov, K. Kadiwala, E. Butanovs, L. Dipane, A. Trausa, D. Bocharov, S. Vlassov, Synthesis of ZnS/Al2O3/TaSe2 Core/Shell Nanowires Using Thin Ta Metal Film Precursor, ChemEngineering 8 (2024) 25. https://doi.org/10.3390/chemengineering8010025.

[156] K. Kadiwala, E. Dipans, L. Dipane, E. Butanovs, B. Polyakov, Towards Scalable Synthesis of $TiSe_2$ and VSe_2 Thin Films, Latvian Journal of Physics and Technical Sciences 61 (2024) 13–22. https://doi.org/10.2478/lpts-2024-0009.

[157] K. Kadiwala, L. Dipane, E. Dipans, A. Bundulis, M. Zubkins, A. Ogurcovs, J. Gabrusenoks, D. Bocharov, E. Butanovs, B. Polyakov, Synthesis and Investigation of ReSe2 Thin Films Obtained from Magnetron Sputtered Re and ReOx, Crystals (Basel) 14 (2024) 690. https://doi.org/10.3390/cryst14080690.

[158] K. Kadiwala, E. Butanovs, A. Ogurcovs, M. Zubkins, B. Polyakov, Comparative study of WSe2 thin films synthesized via pre-deposited WO3 and W precursor material selenization, J Cryst Growth 593 (2022) 126764. https://doi.org/10.1016/j.jcrysgro.2022.126764.

[159] E. Butanovs, K. Kadiwala, A. Gopejenko, D. Bocharov, S. Piskunov, B. Polyakov, Different strategies for GaN-MoS2 and GaN-WS2 core–shell nanowire growth, Appl Surf Sci 590 (2022) 153106. https://doi.org/10.1016/j.apsusc.2022.153106.

[160] J. Lee, N. Shin, Toward an understanding of the mechanism of mixed-salt-mediated CVD growth of MoSe2, Appl Phys Lett 123 (2023). https://doi.org/10.1063/5.0165703.

[161] R. Dziobek-Garrett, S. Hilliard, S. Sriramineni, O. Ambrozaite, Y. Zhu, B.M. Hudak, T.H. Brintlinger, T. Chowdhury, T.J. Kempa, Controlling Morphology and Excitonic Disorder in Monolayer WSe_2 Grown by Salt-Assisted CVD Methods, ACS Nanoscience Au 3 (2023) 441–450. https://doi.org/10.1021/acsnanoscienceau.3c00028.

[162] S. Li, Y.-C. Lin, J. Hong, B. Gao, H.E. Lim, X. Yang, S. Liu, Y. Tateyama, K. Tsukagoshi, Y. Sakuma, K. Suenaga, T. Taniguchi, Mixed-Salt Enhanced Chemical Vapor Deposition of Two-Dimensional Transition Metal Dichalcogenides, Chemistry of Materials 33 (2021) 7301–7308. https://doi.org/10.1021/acs.chemmater.1c01652.

[163] I. Hotovy, L. Spiess, M. Mikolasek, I. Kostic, H. Romanus, Structural and morphological evaluation of layered WS2 thin films, Vacuum 179 (2020) 109570. https://doi.org/10.1016/j.vacuum.2020.109570.

[164] S.K. Jain, R.R. Kumar, N. Aggarwal, P. Vashishtha, L. Goswami, S. Kuriakose, A. Pandey, M. Bhaskaran, S. Walia, G. Gupta, Current Transport and Band Alignment Study of MoS2 /GaN and MoS2 /AlGaN Heterointerfaces for Broadband Photodetection Application, ACS Appl Electron Mater 2 (2020) 710–718. https://doi.org/10.1021/acsaelm.9b00793.

[165] E. Hossain, A.A. Rahman, A.P. Shah, B.A. Chalke, A. Bhattacharya, Large-area, thermally-sulfurized WS2 thin films: control of growth direction and use as a substrate for GaN epitaxy, Semicond Sci Technol 35 (2020) 035011. https://doi.org/10.1088/1361-6641/ab6bb3.

[166] J. Lee, H. Jang, T. Kwak, U. Choi, B. So, O. Nam, Growth and characterization of MoS2/n-GaN and MoS2/p-GaN vertical heterostructure with wafer scale homogeneity, Solid State Electron 165 (2020) 107751. https://doi.org/10.1016/j.sse.2019.107751.

[167] S.E. Panasci, I. Deretzis, E. Schilirò, A. La Magna, F. Roccaforte, A. Koos, M. Nemeth, B. Pécz, M. Cannas, S. Agnello, F. Giannazzo, Interface Properties of MoS2 van der Waals Heterojunctions with GaN, Nanomaterials 14 (2024) 133. https://doi.org/10.3390/nano14020133.

[168] F. Khan, M. Idrees, C. Nguyen, I. Ahmad, B. Amin, A first-principles study of electronic structure and photocatalytic performance of GaN–MX2 (M = Mo, W; X= S, Se) van der Waals heterostructures, RSC Adv 10 (2020) 24683–24690. https://doi.org/10.1039/D0RA04082G.

[169] Md.S.H. Khan, M.S. Islam, Md.R. Islam, A. Iskanderani, I.M. Mehedi, Md.T. Hasan, Potential Visible-Light Driven PtO_2/GaN vdW Hetero-Bilayer Photocatalysts for Water Splitting Using First-Principles, IEEE Access 9 (2021) 109510–109521. https://doi.org/10.1109/ACCESS.2021.3102190.

[170] S.J. Cartamil-Bueno, P.G. Steeneken, F.D. Tichelaar, E. Navarro-Moratalla, W.J. Venstra, R. van Leeuwen, E. Coronado, H.S.J. van der Zant, G.A. Steele, A. Castellanos-Gomez, High-quality-factor tantalum oxide nanomechanical resonators by laser oxidation of TaSe2, Nano Res 8 (2015) 2842–2849. https://doi.org/10.1007/s12274-015-0789-8.

[171] Z. Yan, C. Jiang, T.R. Pope, C.F. Tsang, J.L. Stickney, P. Goli, J. Renteria, T.T. Salguero, A.A. Balandin, Phonon and thermal properties of exfoliated TaSe2 thin films, J Appl Phys 114 (2013). https://doi.org/10.1063/1.4833250.

[172] A. Kassim, S. Nagalingam, H.S. Min, N. Karrim, XRD and AFM studies of ZnS thin films produced by electrodeposition method, Arabian Journal of Chemistry 3 (2010) 243–249. https://doi.org/10.1016/j.arabjc.2010.05.002.

[173] H. Wang, Y. Chen, C. Zhu, X. Wang, H. Zhang, S.H. Tsang, H. Li, J. Lin, T. Yu, Z. Liu, E.H.T. Teo, Synthesis of Atomically Thin 1T-TaSe2 with a Strongly Enhanced Charge-Density-Wave Order, Adv Funct Mater 30 (2020). https://doi.org/10.1002/adfm.202001903.

[174] L. Najafi, S. Bellani, R. Oropesa-Nuñez, B. Martín-García, M. Prato, L. Pasquale, J.-K. Panda, P. Marvan, Z. Sofer, F. Bonaccorso, TaS2 , TaSe2, and Their Heterogeneous Films as Catalysts for

the Hydrogen Evolution Reaction, ACS Catal 10 (2020) 3313–3325. https://doi.org/10.1021/acscatal.9b03184.

[175] P.M. Pataniya, C.K. Zankat, M. Tannarana, A. Patel, S. Narayan, G.K. Solanki, K.D. Patel, P.K. Jha, V.M. Pathak, Photovoltaic activity of WSe2/Si hetero junction, Mater Res Bull 120 (2019). https://doi.org/10.1016/j.materresbull.2019.110602.

[176] G.H. Shin, C. Park, K.J. Lee, H.J. Jin, S.Y. Choi, Ultrasensitive Phototransistor Based on WSe2-MoS2van der Waals Heterojunction, Nano Lett 20 (2020) 5741–5748. https://doi.org/10.1021/acs.nanolett.0c01460.

[177] K. Andrews, U. Rijal, A. Bowman, H.J. Chuang, M.R. Koehler, J. Yan, D.G. Mandrus, P.Y. Chen, Z. Zhou, Accumulation-Type Ohmic van der Waals Contacts to Nearly Intrinsic WSe2Nanosheet-Based Channels: Implications for Field-Effect Transistors, ACS Appl Nano Mater 4 (2021) 5598–5610. https://doi.org/10.1021/acsanm.1c01138.

[178] F. Qi, X. Wang, B. Zheng, Y. Chen, B. Yu, J. Zhou, J. He, P. Li, W. Zhang, Y. Li, Self-assembled chrysanthemum-like microspheres constructed by few-layer ReSe2 nanosheets as a highly efficient and stable electrocatalyst for hydrogen evolution reaction, Electrochim Acta 224 (2017) 593–599. https://doi.org/10.1016/j.electacta.2016.12.097.

[179] R. Oliva, M. Laurien, F. Dybala, J. Kopaczek, Y. Qin, S. Tongay, O. Rubel, R. Kudrawiec, Pressure dependence of direct optical transitions in ReS2 and ReSe2, NPJ 2D Mater Appl 3 (2019) 20. https://doi.org/10.1038/s41699-019-0102-x.

[180] Y. Liu, X. Li, Y. Guo, T. Yang, K. Chen, C. Lin, J. Wei, Q. Liu, Y. Lu, L. Dong, C. Shan, Modulation on the electronic properties and band gap of layered ReSe2 via strain engineering, J Alloys Compd 827 (2020) 154364. https://doi.org/10.1016/j.jallcom.2020.154364.

[181] F. Liu, X. Zhao, X.-Q. Yan, J. Xie, W. Hui, X. Xin, Z.-B. Liu, J.-G. Tian, Ultrafast nonlinear absorption and carrier relaxation in ReS2 and ReSe2 films, J Appl Phys 125 (2019). https://doi.org/10.1063/1.5093757.

[182] H. Saqib, S. Rahman, Y. Zhao, C. Cazorla, D. Errandonea, R. Susilo, Y. Zhuang, yanwei Huang, B. Chen, N. Dai, Evolution of Structural and Electronic Properties of TiSe2 under High Pressure, J Phys Chem Lett 12 (2021) 9859–9867. https://doi.org/10.1021/acs.jpclett.1c02492.

[183] H.S. Arora, R. Polski, Y. Zhang, A. Thomson, Y. Choi, H. Kim, Z. Lin, I.Z. Wilson, X. Xu, J.H. Chu, K. Watanabe, T. Taniguchi, J. Alicea, S. Nadj-Perge, Superconductivity in metallic twisted bilayer graphene stabilized by WSe2, Nature 583 (2020) 379–384. https://doi.org/10.1038/s41586-020-2473-8.

[184] T. Wang, K. Andrews, A. Bowman, T. Hong, M. Koehler, J. Yan, D. Mandrus, Z. Zhou, Y.Q. Xu, High-Performance WSe2 Phototransistors with 2D/2D Ohmic Contacts, Nano Lett 18 (2018) 2766–2771. https://doi.org/10.1021/acs.nanolett.7b04205.

[185] Z. Wu, W. Zhao, J. Jiang, T. Zheng, Y. You, J. Lu, Z. Ni, Defect Activated Photoluminescence in WSe2 Monolayer, Journal of Physical Chemistry C 121 (2017) 12294–12299. https://doi.org/10.1021/acs.jpcc.7b03585.

[186] J. Zhou, J. Lin, X. Huang, Y. Zhou, Y. Chen, J. Xia, H. Wang, Y. Xie, H. Yu, J. Lei, D. Wu, F. Liu, Q. Fu, Q. Zeng, C.-H. Hsu, C. Yang, L. Lu, T. Yu, Z. Shen, H. Lin, B.I. Yakobson, Q. Liu, K. Suenaga, G. Liu, Z. Liu, A library of atomically thin metal chalcogenides, Nature 556 (2018) 355–359. https://doi.org/10.1038/s41586-018-0008-3.

Acknowledgements

First and foremost, I would like to express my sincere gratitude to my supervisor, Dr. Boris Polyakovs, for his vital guidance and support throughout my PhD studies. His overall expertise in the field of material science and his dedication to my development have been instrumental in shaping my research journey.

Special thanks go to Dr. Edgars Butanovs for his significant contributions to my research. His invaluable guidance, from the very beginning of teaching me experimental tools, methodologies and to instilling the importance of adaptability in this field, has been instrumental to my success.

I am indebted to my colleagues for their support and camaraderie throughout my research. Their insights, experimental support, and guidance were essential to the success of my research. I would like to express my sincere appreciation to Andrejs Ogurcovs, Martin Zubkins, Annamarija Trausa, Karlis Vilks, Arturs Bundulis, Aleksejs Zoltrovs, Alexei Kuzmins, Liga Jasulaneca, Luize Dipane, Eriks Dipans, Viktors Vibornijs, Edwards Strods, Alexanders Novikovs, Thomas Yager, and Halil Arslan.

I extend my sincere thanks to Juris Purans, Andris Anspoks, and Andris Sternbergs for their committed belief in my abilities and their generous financial support. Their contributions have been instrumental in creating an environment that allowed me to fully concentrate on my research.

Finally, I would like to express my sincere gratitude to my family and friends for their unwavering support throughout my PhD journey. My brother's constant encouragement has been a source of inspiration for me. I am eternally grateful to my dearest friend, Nair, whose belief in me made this entire journey possible. I would also like to acknowledge the invaluable support of my Dostaar, my Luvvaz and Don Pablo whose encouragement and discussions have been instrumental in my success.

I am grateful for the financial support provided by the Latvian Council of Science through projects LZP-2020/1-0261 and LZP-2020/1-0345. Furthermore, the Institute of Solid State Physics, University of Latvia, awarded two 'Student and Young Researcher Grants' to support this research. Additionally, the European Union's Horizon 2020 Framework Programme grant CAMART2 (No. 739508) played a crucial role in enhancing the quality and scope of the study.